

Dynamics of Continuous Attractor Neural Networks

by

FUNG, Chi Chung

A Thesis Submitted to
The Hong Kong University of Science and Technology
in Partial Fulfillment of the Requirements for
the Degree of Master of Philosophy
in Physics

August 2010, Hong Kong

Authorization

I hereby declare that I am the sole author of the thesis.

I authorize the Hong Kong University of Science and Technology to lend this thesis to other institutions or individuals for the purpose of scholarly research.

I further authorize the Hong Kong University of Science and Technology to reproduce the thesis by photocopying or by other means, in total or in part, at the request of other institutions or individuals for the purpose of scholarly research.

FUNG, Chi Chung

23 August 2010

Dynamics of Continuous Attractor Neural Networks

by

FUNG, Chi Chung

This is to certify that I have examined the above MPhil thesis
and have found that it is complete and satisfactory in all respects,
and that any and all revisions required by
the thesis examination committee have been made.

Prof. K. Y. Michael Wong, Thesis Supervisor

Prof. Tai Kai Ng, Head of Department

Department of Physics

23 August 2010

Acknowledgments

I would like to express my deep gratitude to my supervisor, Prof. K. Y. Michael Wong, who has given me a lot of advice and kind support in my research during two years of my MPhil study. I would like to thank the Department of Physics for providing me with postgraduate studentship award so I have the valuable opportunity to study here. I would like to thank the postgraduate students in the Department of Physics who have given me a lot of help and valuable opinions in different ways. Also, I would like to thank Prof. Si Wu, a senior investigator in Institute of Neuroscience, Chinese Academy of Science, for supporting the research direction of my postgraduate study. In addition, I would like to thank Prof. Bradley A. Foreman and Prof. Yilong Han for taking time to be examiners of my thesis examination. Lastly, I would like to appreciate the support of my family.

Contents

Title Page	i
Authorization Page	ii
Signature Page	iii
Acknowledgments	iv
Table of Contents	v
List of Figures	viii
Abstract	xii
Chapter 1 Background	1
1.1 Introduction	1
1.2 Continuous Attractors	2
1.3 Outline of this Thesis	3
Chapter 2 Review: The Perturbative Approach on One-dimensional Continuous Attractor Neural Networks	6
2.1 1D Continuous Attractor Neural Networks with Divisive Inhibition . . .	6
2.1.1 Tracking	8
2.2 Perturbative Approach on 1D Continuous Attractors Neural Networks with Divisive Inhibition	8
2.3 Summary	11
Chapter 3 Continuous Attractor Neural Networks with Mexican-Hat Couplings	13
3.1 Introduction	13
3.2 Tracking Performance	15
3.2.1 1D ANN with Various Parameters	17

3.2.2	Trackability with an Abruptly Changed Stimulus	19
3.3	2D Continuous Attractor Neural Networks with Mexican-Hat Couplings .	23
3.3.1	Instability of 2D CANNs with Mexican Couplings	26
3.4	Summary	27
Chapter 4	Dynamics of 2D Continuous Attractor Neural Networks with Divisive Inhibition	32
4.1	Introduction	32
4.2	Solution to the Model	33
4.2.1	Using Basis Functions in Rectangular Coordinates	35
4.2.2	Using Basis Functions in Polar Coordinates	38
4.3	Simulation Experiments	43
4.3.1	Reaction Time to an Abrupt Change of the Stimulus	44
4.3.2	Amplitudes of the Basis Function Distortion Modes	45
4.4	Summary	45
Chapter 5	1D Continuous Attractor Neural Networks with Time- dependent Couplings	48
5.1	Introduction	48
5.2	Synaptic Depression	48
5.2.1	Phase Diagram	49
5.2.2	Plateau States	50
5.2.3	Tracking Performance	51
5.3	Analysis	53
5.3.1	Static Bump Solution	56
5.3.2	Perturbative Approach to Synaptic Depression	59
5.3.3	Slow-decaying Behavior	65
5.3.4	Tracking along the Preferred Stimulus Space	65
5.4	Synaptic Facilitation	70
5.4.1	Tracking Performance: A comparison with Synaptic Depression .	70
5.5	Summary	72
Chapter 6	Conclusion	73
Appendix A	Derivation of the interacting kernel matrix $\mathcal{F}_{nmn'm'}$ for 2D CANNs with Divisive Inhibition	77

Appendix B	Derivation of Bump Speed for 2D CANNs with Divisive Inhibition	79
Appendix C	Proof: $\Psi_{l\pm l}$ are the eigenfunctions of \mathcal{G}	81
Bibliography		83

List of Figures

Figure 1.1	Left : An example of a neural network. Right : Illustration about how a artificial neuron works.	2
Figure 1.2	A diagram illustrate the concept of discrete attractors. Dashed lines are the basin boundary between different attractors, the black dots. It the system is start from any points within this space of the neuronal response, the system will relax to one of the attractors.	3
Figure 1.3	A diagram illustrate the concept of continuous attractors. If the state of the system is away from the continuous line attractor, the system will relax to the continuous attractor gradually.	4
Figure 1.4	Illustration of a bump-shape neuronal response.	4
Figure 2.1	The Gaussian-shaped stationary states of the network.	7
Figure 2.2	Tracking the change of position of stimulus from 0 to 1.5. Parameters: $N = 200$, $\alpha = 0.15$, $a = 0.5$, $\tau_s = 1$, $k = 0.5$, $\rho = N/(2\pi)$ and $J_0 = \sqrt{2\pi}a$. Range of preferred stimulus is $(-\pi, \pi]$	9
Figure 2.3	The first four basis functions of the quantum harmonic oscillators, representing distortions in the height, position, width and skewness of the Gaussian bump.	9
Figure 2.4	Snapshots of the neuronal inputs in the center-of-mass frame of the bump. Symbols: simulations. Solid lines: predicted synaptic input with the $n = 10$ perturbation. Dashed lines: synaptic input at $t = 0$. Parameters: $N = 200$, $\alpha = 0.15$, $a = 0.5$, $\tau_s = 1$, $k = 0.5$, $\rho = N/(2\pi)$ and $J_0 = \sqrt{2\pi}a$	12
Figure 3.1	The bump functions are of height 0.5, while the Gaussian function is with $a = 0.75$ and $\omega_0 = 0.05$. In the neural network, there are $N = 96$ neurons distributed uniformly over $(-6, 6]$, while the boundary condition is periodic.	16
Figure 3.2	Reaction of neuronal responses. The stimulus changed from 0 to 2 at $t = 0$. Parameter: $N = 96$, $k = 1$. Bump function: truncated cosine.	18
Figure 3.3	Reaction of neuronal responses. The stimulus changed from 0 to 3 at $t = 0$. Parameter: $N = 96$, $k = 1$. Bump function: truncated cosine.	18
Figure 3.4	Reaction of neuronal responses. The stimulus changed from 0 to 4 at $t = 0$. Parameter: $N = 96$, $k = 1$. Bump function: truncated cosine.	19

Figure 3.5	The cutoffs of z_0 for one bump and tracking of 1D ANNs with respect to k . Parameter: $\omega_0 = 0.05$. Bump function: truncated cosine. Parameters: range of the network = $(-6, 6]$ and $N = 96$. 20
Figure 3.6	The contour plot of cutoff of z_0 for one bump of 1D ANNs for different combinations of ω_0 and k . Parameter: $N = 96$. Bump function: truncated cosine. 21
Figure 3.7	The contour plot of cutoff of z_0 for one bump of 1D ANNs for different combinations of ω_0 and k . Parameter: $N = 96$. Bump function: Gaussian. 21
Figure 3.8	Cutoff of z_0 for tracking. The sample bump functions are the truncated cosine. Parameters: the same as figure 3.6. . . . 22
Figure 3.9	Cutoff of z_0 for tracking. The sample bump functions are Gaussian. Parameters: the same as figure 3.7. 22
Figure 3.10	Tracking speed vs. position of the bump with different z_0 . Parameters: $N = 96$, $\omega_0 = 0.05$, $k = 1$, range of the network = $(-6, 6)$ and $z_0 = 2$ 24
Figure 3.11	The couplings obtained from the truncated cosine functions. The bump functions are of height 0.5. The neural network is a square lattice with periodic boundary condition. There are $N = N_x \times N_y = 40 \times 40$ neurons distributed on $(-2\pi, 2\pi] \times (-2\pi, 2\pi]$. 25
Figure 3.12	The couplings obtained from the Gaussian functions. The bump functions are of height 0.5. Structure and other parameters are the same as figure 3.11. 26
Figure 3.13	Reaction of neuronal responses. The stimulus changed from $(0, 0)$ to $(1, 1)$. Parameter: $N = N_x \times N_y = 40 \times 40$, $k = 2.5$. Bump function: truncated cosine. 27
Figure 3.14	Reaction of neuronal responses. The stimulus changed from $(0, 0)$ to $(2.26, 2.26)$. Parameter: $N = N_x \times N_y = 40 \times 40$, $k = 2.5$. Bump function: truncated cosine. 28
Figure 3.15	Reaction of neuronal responses. The stimulus changed from $(0, 0)$ to $(1, 1)$. Parameter: $N = N_x \times N_y = 40 \times 40$, $k = 1$. Bump function: truncated cosine. 28
Figure 3.16	Reaction of neuronal responses. The stimulus changed from $(0, 0)$ to $(1, 1)$. Parameter: $N = N_x \times N_y = 40 \times 40$, $k = 3$. Bump function: truncated cosine. 29
Figure 3.17	Reaction of neuronal responses. The stimulus changed from $(0, 0)$ to $(1, 1)$. Parameter: $N = N_x \times N_y = 40 \times 40$, $k = 8$. Bump function: truncated cosine. 29
Figure 3.18	Reaction of neuronal responses. The stimulus changed from $(0, 0)$ to $(1, 1)$. Parameter: $N = N_x \times N_y = 40 \times 40$, $k = 3$. Bump function: Gaussian. 30
Figure 3.19	Reaction of neuronal responses. The stimulus changed from $(0, 0)$ to $(1, 1)$. Parameter: $N = N_x \times N_y = 40 \times 40$, $k = 8$. Bump function: Gaussian. 30

Figure 4.1	A stationary state $\tilde{U}(\mathbf{x}, 0)$. Parameters: $N = 40 \times 40$, $a = 0.5$, $k = 0.5$, $\tau_s = 1$ and $\rho = N/(2\pi)^2$	34
Figure 4.2	The synaptic input in the space due to the abruptly changed stimulus. Parameters: $\alpha = 0.05$, $\mathbf{z}_0(t < 0) = 0$, $\mathbf{z}_0(t \geq 0) = (1, 1)$ and the rest are the same as figure 4.1.	34
Figure 4.3	Real part of the eigenfunction $\Psi_{0,0}$	40
Figure 4.4	Real part of the eigenfunction $\Psi_{1,\pm 1}$	40
Figure 4.5	Real part of the eigenfunction $\Psi_{2,0}$	41
Figure 4.6	Real part of the eigenfunction $\Psi_{2,\pm 2}$	41
Figure 4.7	Real part of the eigenfunction $\Psi_{3,\pm 1}$	42
Figure 4.8	Real part of the eigenfunction $\Psi_{3,\pm 3}$	42
Figure 4.9	The reaction time T for the synaptic input to catch up the stimulus position change from 0 to z_{01} . Parameters: $N = N_x \times N_y = 40 \times 40$, $\Theta = \pi\sqrt{2/N}$, $\alpha = 0.05$ and the rest are the same as figure 4.1. Near $ \mathbf{z}_0 = 0$, the reaction time is zero up to Θ , because the reaction time is defined as the time needed for the bump to track from 0 to $ \mathbf{z}_0 $ within the range of Θ	44
Figure 4.10	The experimentally projected $b_{l,j}$ and the predicted $b_{l,j}$ using $l = 10$ perturbation. Solid lines: corresponding predictions. Circles: simulation results. Parameters: same as figure 4.9. . .	46
Figure 5.1	Phase diagram of the network states. Symbols: numerical solutions. Dashed line: predicted boundary for amplitude-stable static (metastatic) bump. Dotted line: predicted boundary for static bump. Solid line: predicted boundary between silent state and all possible stable bumps. Order of perturbation = 11 th . Point P: the working point for Figs. 5.3 and 5.11. Parameters: $\tau_d/\tau_s = 50$, $a = 0.5/6$, range of the network = $[-\pi, \pi)$	50
Figure 5.2	Neuronal input $u(x, t)$ and the STD coefficient $p(x, t)$ in (a) the static state at $(\bar{k}, \bar{\beta}) = (0.9, 0.005)$, and (b) the moving state at $(\bar{k}, \bar{\beta}) = (0.5, 0.015)$. Parameter: $\tau_d/\tau_s = 50$	51
Figure 5.3	Magnitudes of neuronal input $U(x, t)$ and synaptic depression $1=p(x, t)$ at $(\bar{k}, \bar{\beta}) = (0.95, 0.0085)$ (point P in figure 5.1) and for initial conditions of types A and B in figure 5.11. Symbols: numerical solutions. Lines: Gaussian approximation using Eqs. (5.10) and (5.11). Other parameters: $\tau_d/\tau_s = 50$, $a = 0.5$ and $x \in [-\pi, \pi)$	52
Figure 5.4	Contours of plateau lifetimes in the space of k and β . The lines are the two topmost phase boundaries in figure 5.1. The initial condition is prepared by using stimulus with $\alpha = 0.5$	52
Figure 5.5	The neural response profile tracks the change of position of the external stimulus from $z_0 = 0$ to 1.5 at $t = 0$. Parameters: $\tau_d/\tau_s = 50$, $a = 0.5$, $\bar{k} = 0.95$, $\bar{\beta} = 0.0085$, $\alpha = 0.5$	53

Figure 5.6	The profile of $u(x, t)$ at $t/\tau_s = 0, 1, 2, \dots, 10$ during the tracking process in figure 5.5.	54
Figure 5.7	The response of CANNs with STD to an abruptly changed stimulus from $z_0 = 0$ to $z_0 = 1.5$ at $t = 0$. Symbols: numerical solutions. Lines: Gaussian approximation using 11 th order perturbation of the STD coefficient. Parameters: $\tau_d/\tau_s = 50$, $\alpha = 0.5$, $a = 0.5$ and $x \in [-\pi, \pi)$	55
Figure 5.8	Region of existence of the static bump solution. Dashed line: Parabolas drawn by Eq. (5.16). Solid line: existence region figured out by the parabolas. Parameter: $z = 0.5$	58
Figure 5.9	Region of amplitude stable static bump solution. Dashed line: Parabolas drawn by Eq. (5.16). Solid line: the region figured out by Eq. 5.19. Symbols: simulations. The simulations for $(\bar{k}, \bar{\beta})$ are done by initial conditions prepared with $(\bar{k}, 0)$ and stimulus with $\alpha = 0.5$. However, these simulations may not be appropriate to test this phase boundary. As we will show later, below this phase boundary, the bump may not be <i>totally</i> stable. Some of the states are only amplitude-stable, but not positionally unstable. . .	60
Figure 5.10	Comparison of predictions with perturbation with various orders. The predicted phase boundary is oscillating around the simulation result.	64
Figure 5.11	Nullclines and plots of $p_0(t)$ against \bar{U} . Symbols: numerical result from Eqs. (5.10) and (5.11) plotted every $2\tau_s$. Dashed line: U -nullcline. Solid line: p_0 -nullcline. Parameter: $\bar{k} = 0.95$, $\bar{\beta} = 0.0085$	66
Figure 5.12	The simulation counterpart of figure 5.11. These results show that the predictions by Eqs. (5.17) and (5.18) agree with the simulations.	66
Figure 5.13	Tracking of a neuronal bump with continuously moving stimulus. Symbols: simulation result of center of mass of neuronal input bump. Dashed line: 11 th order perturbation prediction of Eq. (5.43). Solid line: Continuously moving stimulus with speed 0.03. Parameter: $\alpha = 0.1$, $\bar{k} = 0.5$, $\bar{\beta} = 0.01$, other parameters are the same as figure 5.7.	68
Figure 5.14	Tracking of a neuronal bump with continuously moving stimulus. Symbols: simulation result of center of mass of neuronal input bump. Dashed line: 11 th order perturbation prediction of Eq. (5.43). Solid line: Continuously moving stimulus with speed 0.03. Parameter: $\alpha = 0.1$, $\bar{k} = 0.5$, $\bar{\beta} = 0.05$, other parameters are the same as figure 5.7.	69
Figure 5.15	Comparison between system with synaptic depression, synaptic facilitation, or without time-dependent coupling. Parameter: $\alpha = 0.5$, $\bar{k} = 0.5$, other parameters are the same as figure 5.7.	71

Dynamics of Continuous Attractor Neural Networks

by

FUNG, Chi Chung

Department of Physics
The Hong Kong University of Science and Technology

Abstract

In this thesis, there are three parts related to continuous attractor neural networks (CANNs). They are 1) continuous attractor neural networks with Mexican-hat coupling, 2) two-dimensional (2D) continuous attractor neural networks with divisive inhibition, and 3) one-dimensional (1D) continuous attractor neural networks with divisive inhibition and dynamical synapse. In the first part, two kinds of Mexican-hat couplings are chosen. With this, some properties of CANNs with Mexican-hat couplings will be studied. With some reasonable neuronal response gain functions, the CANNs with Mexican-hat coupling will be unstable. In the second part, the study will be an extension of 1D CANNs with divisive inhibition. The perturbative approach for 1D CANNs will be applied on the its 2D counterpart. In the analysis, eigenfunctions of 2D harmonic oscillator in polar coordinate are chosen to be the basis to decompose the distortion around the local stable bump. This enables us to introduce the perturbative approach and predict the motion of the bump. Also, anisotropic eigenfunctions of the quantum harmonic oscillator are able to describe distortion modes such as those with cigar and triangular shapes. In the last part, the synaptic plasticity effect is introduced to the original 1D model with divisive inhibition. There are two kinds of synaptic plasticity, short-term depression (STD) and short-term facilitation (STF). STD may make the system relax to a spontaneous motion, but it can also improve the tracking performance. STF, as a opposite effect as STD, will slow down the tracking process. By using a perturbative analysis on the function modeling STD, the behavior of STD can be explained, including various phases on the parameter space.

Chapter 1

Background

1.1 Introduction

Neural networks refer to artificial networks of neurons. The connection between neurons are called synapse. The neurons may send signals, or neural response, to its connected neighbors, based on the neural signals received from its neighbors and external stimuli [1] (see figure 1.1). Neural networks received much attention because of its potentials in inspiring new computational algorithms and understanding real nervous systems. For example, neural networks can be used to construct algorithms for memories [2, 3, 4], pattern recognition [5], speech recognition [6] and so on. Neural networks can also be treated as simplified models for the real biological systems. For example, it can be used to model the reactions of the brain for recognition of object's positions [7] and moving directions [8], and so on. To achieve the above applications and models, the key is to elucidate the architecture of the network and coupling strength between neurons.

As a demonstration, suppose, at the moment, we look for a neural network to recognize patterns composed of N states of 1 (representing “on” or active) or -1 (representing “off” or inactive), e.g. (1, 1, -1, 1, -1, -1,). The goal is to code the given patterns as the responses of the neurons. For this purpose, a fully connected neural network with N neurons is used. The connection strength between neuron i and neuron j is denoted by ω_{ij} , while the neuronal response is denoted by $r_i = \text{sgn} \left(\sum_{j=1}^N \omega_{ij} r_j \right)$ for neuron i . Suppose there are p patterns to be stored within the network. For $p = 1$, substituting $\omega_{ij} = r_i^1 r_j^1 / N$ and $r_j = r_j^1$ into the right hand yields $r_i = \text{sgn} \left(\sum_j \omega_{ij} r_j^1 \right) = r_i^1$. Hence the coupling $\omega_{ij} = r_i^1 r_j^1 / N$ forms a neural network that recognizes the pattern. For $p > 1$, $\omega_{ij} = \sum_{\mu=1}^p r_i^\mu r_j^\mu / N$, which is known as Hebb rule [9], which implies that if neuron i and neuron j always give the same (opposite) signal in the given p patterns, the coupling between them will be positive (negative). By similar reasoning, ω_{ij} will be zero for neurons i and j are independent. For $1 \leq p \ll N$, for any initial condition of

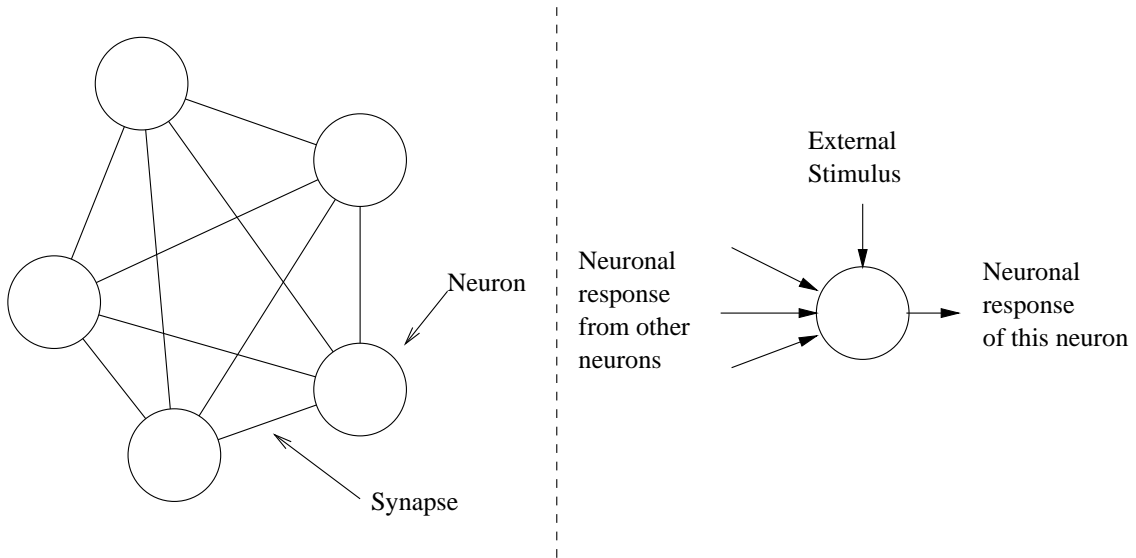


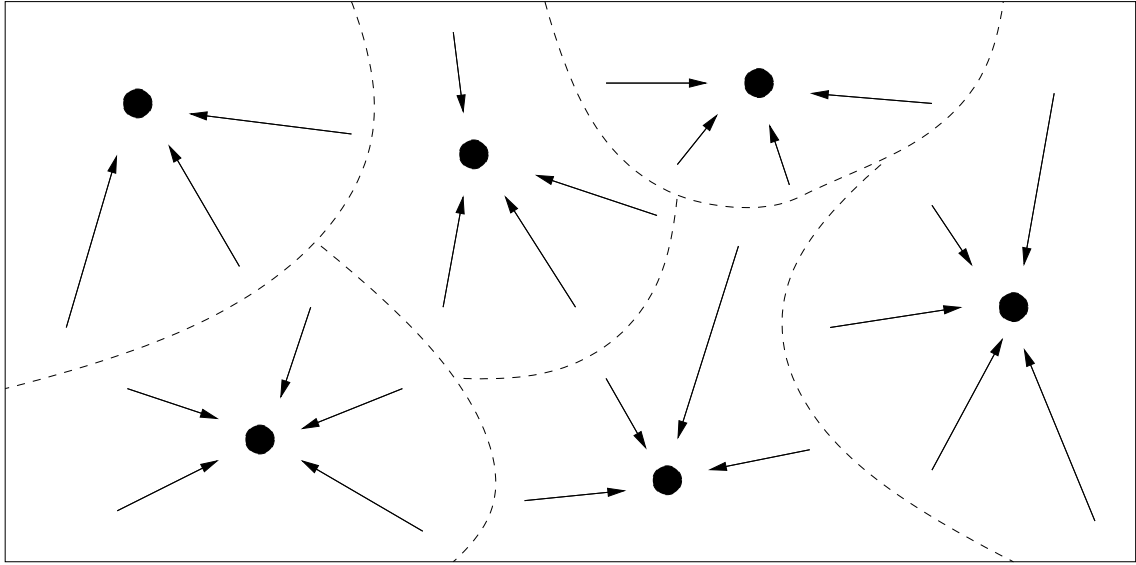
Figure 1.1: Left : An example of a neural network. Right : Illustration about how a artificial neuron works.

$\{r_i\}$, the system will relax to one of the given patterns or its negative counterpart. In this situation, we can say that, this neural network *remembers* those p patterns. Since any initial $\{r_i\}$ can relax to one of the given patterns, the given patterns are then the *attractors* of the space of all possible r_i . However, this kind of attractor cannot represent continuous information in the real system, e.g. positions and moving directions. This type of attractors are called discrete attractors (see figure 1.2).

1.2 Continuous Attractors

With some particular architectures and neuronal couplings, as shown in figure 1.3, the attractor in the space of the neuronal response will be a continuous attractor. Since the system can be stable on the line attractor, any perturbation along the line attractor can change the system from the original state to a new state nearby. In the biological systems, this kind of attractors can be used to represent continuous variables.

Georgopoulos et al. [10] found that, monkeys use a bump-shape neuronal response (see figure 1.4) to represent an orientation, which is a continuous variable. In this system, the response of a neuron will be maximal if a specific external stimulus is applied. The quantity represented by this specific stimulus, e.g. position or moving direction of an object, could be used to label this neuron, namely *preferred stimulus*. In figure 1.4, the shape of the neuronal response will be a bump, if we plot the response against the preferred stimulus. Also, these bumps represent the continuous variable by its center



Space of the neuronal response

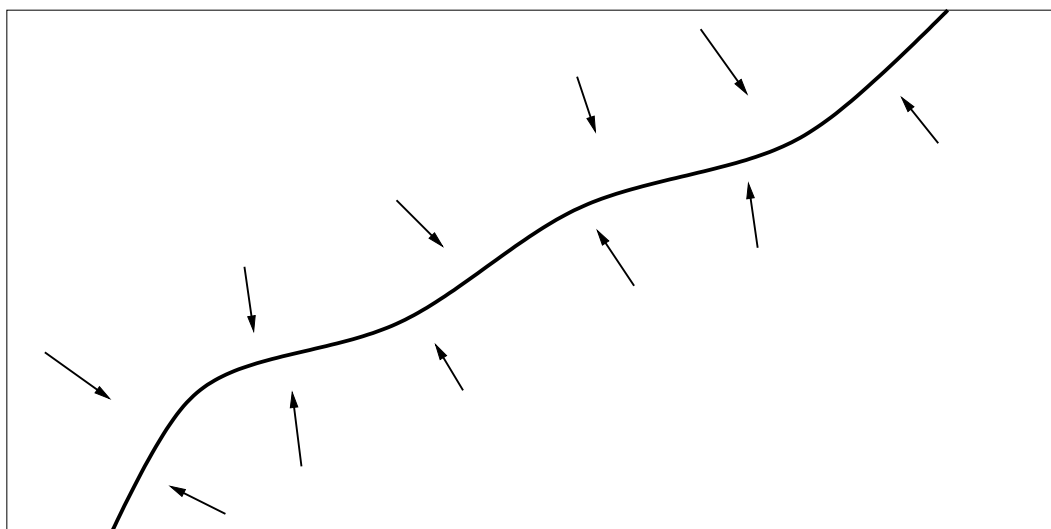
Figure 1.2: A diagram illustrate the concept of discrete attractors. Dashed lines are the basin boundary between different attractors, the black dots. If the system is start from any points within this space of the neuronal response, the system will relax to one of the attractors.

of mass. For example, the neuronal response profile in figure 1.4 is representing the continuous variable z . If the external stimulus is changing, the bump will track the change of stimulus. This tracking behavior will be discussed throughout this thesis.

1.3 Outline of this Thesis

In this thesis, the dynamics of Continuous Attractor Neural Networks (CANNs) will be discussed. In the chapter 2, a perturbative approach on one-dimensional CANNs will be reviewed, while the study of two-dimensional (2D) CANN with Divisive Inhibition is also important (Chapter 4), because, in the nervous system, 2D information is not rare. The dynamics of 2D CANNs should be richer [11, 12, 13], compared with to that in one-dimensional (1D). Also, in the cortex, neurons are essentially distributed in a two-dimensional sheet [14].

The time independent coupling mentioned above is also not realistic [15]. The neural signal is sent by the neural transmitters. However, the concentration of the neural transmitters is not a constant. That means, the efficiency of the neural signal transmission may not be perfect. To model this, a time-dependent term is introduced with the coupling function (Chapter 5). This introduction of term may induce a sponta-



Space of the neuronal response

Figure 1.3: A diagram illustrate the concept of continuous attractors. If the state of the system is away from the continuous line attractor, the system will relax to the continuous attractor gradually.

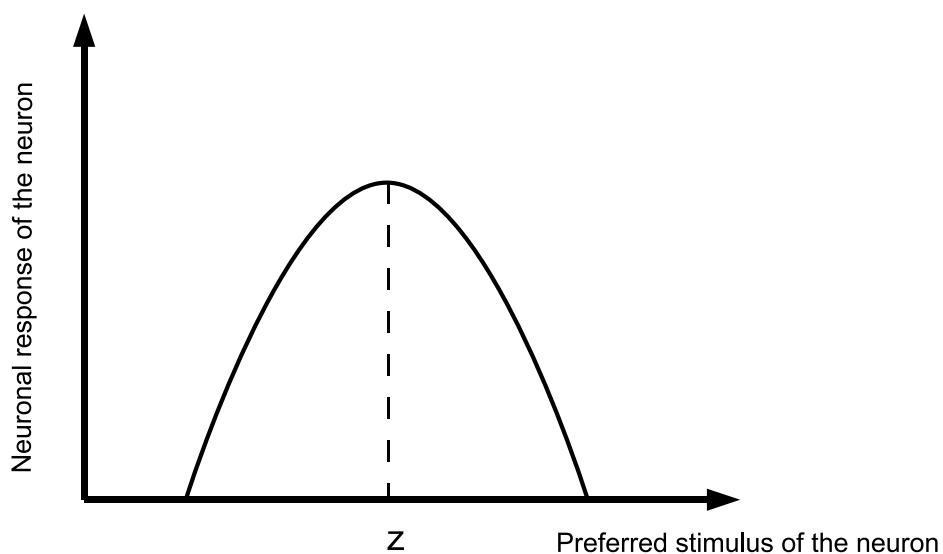


Figure 1.4: Illustration of a bump-shape neuronal response.

neous motion in the system. Also, it may affect the tracking performance. However, the concentration of the neural transmitters is not the only factor affecting the connection efficiency. The neuronal response may raise the level of calcium [16]. This effect may strengthen the coupling between neurons. In chapter 5, both of these two effects will be discussed separately.

Besides, the performance of the CANN with Mexican-hat coupling, an alternative choice of translationally invariant couplings, will also be reported (Chapter 3). It is found that, in this case, the system may not track changes of the stimulus in some cases. Also, for the 2D version of the network, the system may be unstable to some changes of the stimulus in some cases.

Chapter 2

Review: The Perturbative Approach on One-dimensional Continuous Attractor Neural Networks

2.1 1D Continuous Attractor Neural Networks with Divisive Inhibition

In order to model systems dealing with continuous information, like positions and directions, various kinds of neural networks with *continuous attractors* were proposed [17, 18, 19, 20, 21], known as Continuous Attractor Neural Networks. One of them is called Continuous Attractor Neural Networks with Divisive Inhibition [20, 22]. The network contains N neurons. Each neuron carries a quantity, x , namely preferred stimulus, which codes the information represented by the network signal. The neuronal input of neuron having preferred stimulus x , $U(x, t)$, is governed by the differential equation

$$\tau_s \frac{\partial U(x, t)}{\partial t} = -U(x, t) + \rho \int_{-\infty}^{\infty} dx' J(x, x') r(x') + I^{\text{ext}}(x, t), \quad (2.1)$$

where ρ is the density of neurons over the space of preferred stimulus, I^{ext} is the external signal sending from the outside of the network, $J(x, x')$ is the connection strength (or coupling) between neurons at x and x' , and $r(x)$ represents the neuronal response of neuron at x . They are given by

$$J(x, x') = \frac{J_0}{\sqrt{2\pi a^2}} \exp \left[-\frac{(x - x')^2}{2a^2} \right], \text{ and} \quad (2.2)$$

$$r(x) = \frac{U(x)^2}{1 + k\rho \int_{-\infty}^{\infty} dx' U(x')^2} \Theta[U(x)], \quad (2.3)$$

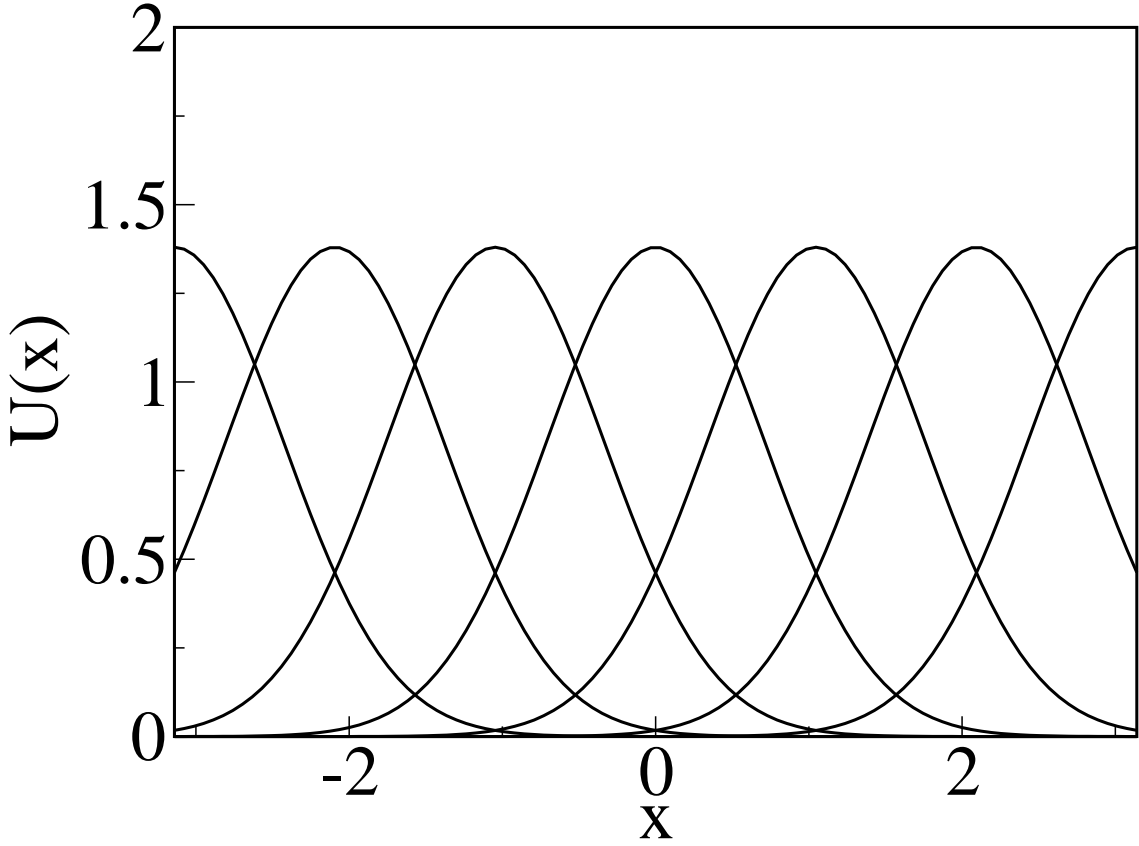


Figure 2.1: The Gaussian-shaped stationary states of the network.

where k is the parameter for controlling the global inhibition for the network and Θ is a step function. When the stimulus is absent, i.e. $I^{\text{ext}} = 0$, and $k < k_c \equiv J_0^2 \rho / (8\sqrt{2\pi}a)$, there are stationary solutions such that $\partial U / \partial t = 0$, which are *stationary states*. By solving Eqs. (2.1) and (2.3), the stationary states are given by

$$\tilde{U}(x - z) = U_0 \exp \left[-\frac{(x - z)^2}{4a^2} \right], \text{ and} \quad (2.4)$$

$$\tilde{r}(x - z) = r_0 \exp \left[-\frac{(x - z)^2}{2a^2} \right], \quad (2.5)$$

where $U_0 = [1 + (1 - k/k_c)^{1/2}]J_0/(4\sqrt{\pi}ak)$ and $r_0 = [1 + (1 - k/k_c)^{1/2}]/(2\sqrt{2\pi}ak\rho)$. It is obvious that these stationary states exist for any z on the preferred stimulus space, as shown in figure 2.1. Therefore, in the preferred stimulus space, the collection of these stationary states forms a continuous line attractor. This is the continuous attractor we want to have to model systems dealing with continuous information in the nervous system.

2.1.1 Tracking

Tracking is an important feature studied by several authors in the literature [21, 22, 23, 24, 25]. These studies have demonstrated that a CANN has the capacity of tracking a moving stimulus continuously and that this tracking behavior can describe many brain functions well. For simplicity, we take

$$I^{\text{ext}}(x, t) = \alpha U_0 \exp \left[-\frac{(x - z_0(t))^2}{4a^2} \right], \quad (2.6)$$

where α represents the strength of the external stimulus. If $\alpha > 0$, due to the broken symmetry of the network, the neuronal input bump will be stable only when $z = z_0$. Consider the most extreme case, $z(t)$ changes from 0 to z'_0 *abruptly*. As shown in figure 2.2, the neuronal input bump will not catch up the new position of the stimulus immediately, but move gradually to the new position of the stimulus. However, in figure 2.2, the neuronal bump can only roughly maintain its original shape during the tracking process. To analyze the distortions during the tracking process and the motion of the tracking bumps, a perturbative approach was introduced [26].

2.2 Perturbative Approach on 1D Continuous Attractors Neural Networks with Divisive Inhibition

Because the shape of the bump is almost preserved during the tracking process, one may let

$$\delta U(x, t) = U(x, t) - \tilde{U}(x - z(t)) \equiv \sum_{n=0}^{\infty} a_n(t) u_n(x - z(t)), \quad (2.7)$$

where u_n , as shown in figure 2.3 are eigenfunctions of quantum harmonic oscillator given by

$$u_n(x) = \frac{1}{\sqrt{\sqrt{2\pi}a2^n n!}} H_n \left(\frac{x}{\sqrt{2}a} \right) \exp \left[-\frac{x^2}{4a^2} \right], \quad (2.8)$$

where H_n is the Hermite Polynomial [27]. The magnitudes of a_n are expected to be small, comparing with U . Since this collection of eigenfunctions is complete, for all possible δU , there exists a linear combination of u_n satisfying Eq. (2.7). With Eq. (2.7), linearization

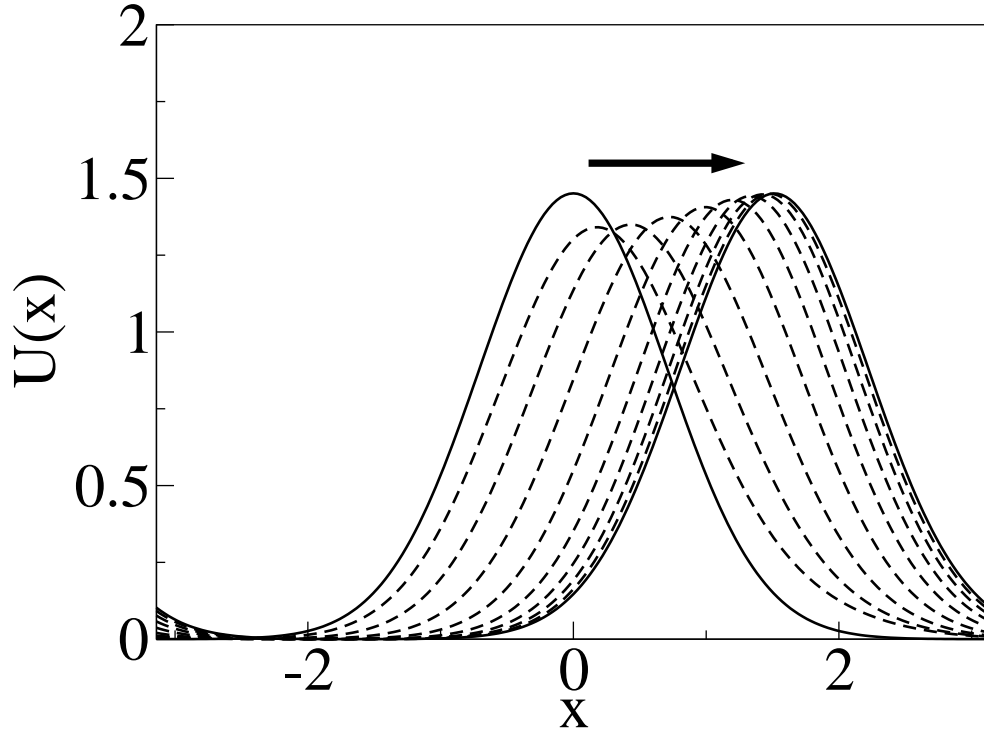


Figure 2.2: Tracking the change of position of stimulus from 0 to 1.5. Parameters: $N = 200$, $\alpha = 0.15$, $a = 0.5$, $\tau_s = 1$, $k = 0.5$, $\rho = N/(2\pi)$ and $J_0 = \sqrt{2\pi}a$. Range of preferred stimulus is $(-\pi, \pi]$.

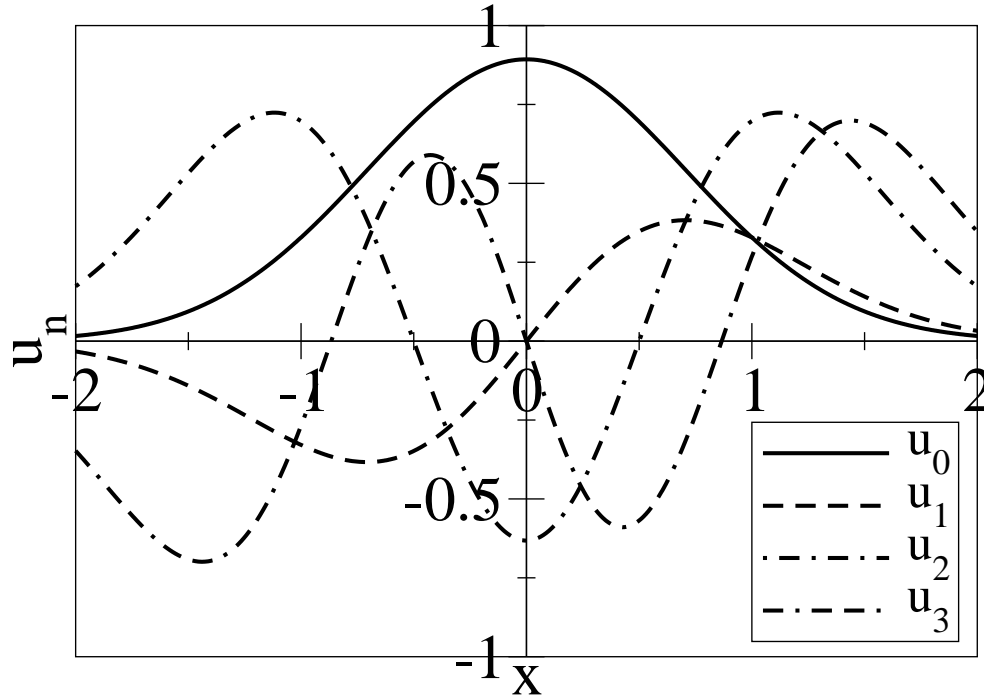


Figure 2.3: The first four basis functions of the quantum harmonic oscillators, representing distortions in the height, position, width and skewness of the Gaussian bump.

of Eq. (2.1) leads to

$$\begin{aligned}
\tau_s \frac{\partial U}{\partial t} &= -\delta U + \rho \int_{-\infty}^{\infty} dx' J(x, x') \int_{-\infty}^{\infty} dx'' \frac{\partial r(x')}{\partial U(x'')} \delta U(x'') + I^{\text{ext}} \\
&= -\delta U + \int_{-\infty}^{\infty} dx' \left[\int_{-\infty}^{\infty} dx'' \rho J(x, x'') \frac{\partial r(x'')}{\partial U(x')} \right] \delta U(x') + I^{\text{ext}} \\
&= -\delta U + \int_{-\infty}^{\infty} dx' F(x, x') \delta U(x') + I^{\text{ext}}, \tag{2.9}
\end{aligned}$$

where $F(x, x')$ has the close form

$$\begin{aligned}
F(x, x') &= \frac{2}{a\sqrt{\pi}} \exp \left[-\frac{(x-x')^2}{2a^2} \right] \exp \left[-\frac{(x'-z)^2}{a^2} \right] \\
&\quad - \frac{1 + \sqrt{1-k/k_c}}{\sqrt{2\pi}a} \exp \left[-\frac{(x-z)^2}{4a^2} \right] \exp \left[-\frac{(x'-z)^2}{4a^2} \right]. \tag{2.10}
\end{aligned}$$

Using the decomposition of Eq. (2.7), the left hand side of Eq. (2.9) is then

$$\begin{aligned}
\tau_s \frac{\partial U}{\partial t} &= \tau_s U_0 \sqrt{\sqrt{2\pi}a} u_1(x-z) \frac{1}{2a} \frac{dz}{dt} \\
&\quad + \tau_s \sum_n \left[\frac{da_n}{dt} + \left(\sqrt{n}a_{n-1} - \sqrt{n+1}a_{n+1} \right) \frac{1}{2a} \frac{dz}{dt} \right] u_n(x-z). \tag{2.11}
\end{aligned}$$

By using the orthogonality of $\{u_m\}$, the right hand side of Eq. (2.9) becomes

$$\begin{aligned}
&-\delta U + \int_{-\infty}^{\infty} dx' F(x, x') \delta U(x') + I^{\text{ext}} \\
&= \sum_n (-a_n + \sum_m \mathcal{F}_{nm} a_m + I_n) u_n(x-z), \tag{2.12}
\end{aligned}$$

where $\mathcal{F}_{nm} = \int dx u_n(x-z) \int dx' u_m(x'-z) F(x, x')$ and $I_n = \int dx u_n(x-z) I^{\text{ext}}(x, t)$. The matrix \mathcal{F}_{nm} is given by [26]

$$\begin{aligned}
\mathcal{F}_{nm} &= 2^{1-m} \sqrt{\frac{m!}{n!} \frac{(-1)^{\frac{m-n}{2}}}{2^{\frac{m-n}{2}} \left(\frac{m-n}{2}\right)!}} & m = n = 0; \\
&0 & m - n \text{ being an even integer} \\
&0 & \text{otherwise.} \tag{2.13}
\end{aligned}$$

Since matrix \mathcal{F}_{nm} is a upper triangular matrix, the eigenvalues are given by the diagonal

elements,

$$\lambda_0 = 1 - \sqrt{1 - k/k_c}, \text{ and} \quad (2.14)$$

$$\lambda_n = 2^{1-n} \quad (n \geq 1). \quad (2.15)$$

Since the eigenvalues are at most 1, all distortions will decay away exponentially, except $n = 1$ [28, 26]. The eigenmode with $n = 1$ represents the change in position. This property guarantees that the neuronal input bump is able to track external stimuli in the preferred stimulus space.

The differential equations of a_n are

$$\begin{aligned} \left(\frac{d}{dt} + \frac{1 - \lambda_n}{\tau_s} \right) a_n &= \frac{I_n}{\tau_s} - \left(U_0 \sqrt{\sqrt{2\pi} a \delta_{n1}} + \sqrt{n} a_{n-1} - \sqrt{n+1} a_{n+1} \right) \frac{1}{2a} \frac{dz}{dt} \\ &+ \frac{1}{\tau_s} \sum_{r=1}^{\infty} \sqrt{\frac{(n+2r)!}{n!}} \frac{(-1)^r}{2^{n+3r-1} r!} a_{n+2r}. \end{aligned} \quad (2.16)$$

With the self consistent condition

$$z(t) = \frac{\int dx U(x) x}{\int dx U(x)}, \quad (2.17)$$

we have [26]

$$\frac{dz}{dt} = \frac{2a}{\tau_s} \frac{I_1 + \sum_{n=3, \text{odd}}^{\infty} \sqrt{\frac{n!!}{(n-1)!!}} I_n + a_1}{U_0 \sqrt{\sqrt{2\pi} a} + \sum_{n=0, \text{even}}^{\infty} \sqrt{\frac{(n-1)!!}{n!!}} a_n}. \quad (2.18)$$

This equation can give the tracking speed of the bump. In practice, it is impossible to sum up $a_n u_n(x - z)$ to $n = \infty$. For a given accuracy, adding terms up to $n = l$ is good enough, which is called $n = l$ perturbation. As an example, results of the $n = 10$ perturbation are shown in figure 2.4. Using Eqs. (2.7), (2.16) and (2.18), one can predict the motion and the distorted shape of the bump. With this method, we can also predict the reaction time of neural network reacting to a change of stimulus.

2.3 Summary

In this revision chapter, the basic concept of continuous attractor is introduced. As mentioned above, the tracking feature is important, because it can model the behavior in real systems after a change of stimulus. However, this kind of motion is usually difficult to analyze. In a previous study [28, 26], a perturbative approach was introduced. The

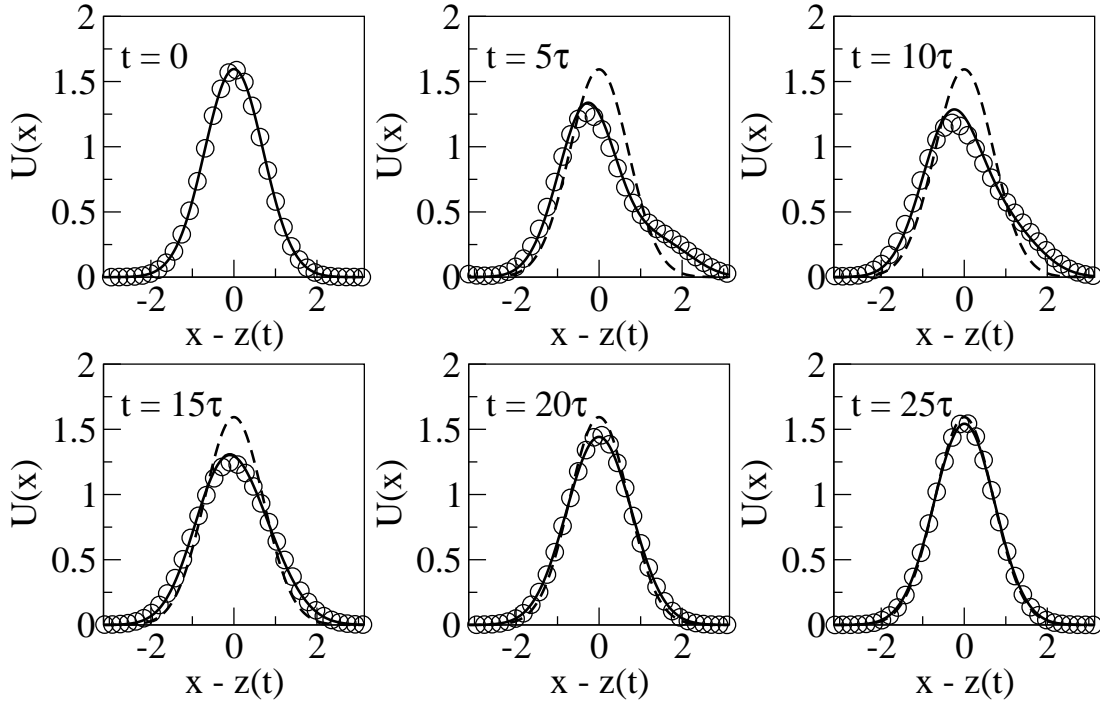


Figure 2.4: Snapshots of the neuronal inputs in the center-of-mass frame of the bump. Symbols: simulations. Solid lines: predicted synaptic input with the $n = 10$ perturbation. Dashed lines: synaptic input at $t = 0$. Parameters: $N = 200$, $\alpha = 0.15$, $a = 0.5$, $\tau_s = 1$, $k = 0.5$, $\rho = N/(2\pi)$ and $J_0 = \sqrt{2\pi}a$.

key idea is that the changes of the shape of the neuronal bumps can be decomposed into different orthogonal modes. This approach is useful to systems having the following characteristics: 1) there exists a continuous family of stationary solution to the system and 2) the coupling function is translational invariant. Therefore, the analytically solvable model we have chosen - the continuous attractor neural network with divisive inhibition - is appropriate. However, this model is just a demonstrational example. In general, this perturbative approach should work for any continuous attractor neural networks satisfying the above two conditions.

Although the perturbation method may result in a massive computation, this method is good because of powerful computers nowadays. However, this is not the end of the story. In the CANN model mentioned above, the dimension of the attractor space is one. The similar approach can be applied in two-dimensional CANNs (Chapter 4).

Chapter 3

Continuous Attractor Neural Networks with Mexican-Hat Couplings

3.1 Introduction

In this chapter, a fully connected network with N neurons is used to demonstrate the behavior. Neurons are evenly distributed on space of preferred stimulus. Each of them are assigned a quantity x representing its preferred stimulus. The dynamics of the neuronal input $U(x, t)$ is governed by

$$\tau \frac{dU(x_i)}{dt} = -U(x_i) + \sum_j \omega_{ij} g[U(x_j)] + I^{\text{ext}}(x_i), \quad (3.1)$$

where g is the gain function such that $r(x_i) = g[U(x_i)]$.

To obtain the coupling ω_{ij} that have a bump-shaped neuronal response centered at z , we may consider minimizing the energy function, taking $g(U) = U$ for simplicity,

$$E_1(z) = \sum_{i=1}^N \left(\sum_{j=1}^N \omega_{ij} r^{\text{sample}}(x_j - z) - r^{\text{sample}}(x_i - z) \right)^2, \quad (3.2)$$

where r^{sample} is the expected function form of the neuronal response. The obtained $\{\omega_{ij}\}$ is the coupling that can minimize this energy function for any z . However, the energy function

$$E_2(z) = \sum_{i=1}^N \left(\sum_{j=1}^N \omega_{ij} \left. \frac{\partial r^{\text{sample}}(x_j - z')}{\partial z'} \right|_{z'=z} - \left. \frac{\partial r^{\text{sample}}(x_i - z')}{\partial z'} \right|_{z'=z} \right)^2 \quad (3.3)$$

is also possible. Expanding the energy function $E_2(z)$,

$$E_2(z) = \sum_{i=1}^N \left[\left(\sum_{j=1}^N \omega_{ij} \frac{\partial r^{\text{sample}}(x_j - z')}{\partial z'} \Big|_{z'=z} \right)^2 + \left(\frac{\partial r^{\text{sample}}(x_i - z')}{\partial z'} \Big|_{z'=z} \right)^2 - 2 \sum_{j=1}^N \omega_{ij} \frac{\partial r^{\text{sample}}(x_j - z')}{\partial z'} \Big|_{z'=z} \frac{\partial r^{\text{sample}}(x_i - z')}{\partial z'} \Big|_{z'=z} \right]. \quad (3.4)$$

In Eq. (3.4), the first two terms can only relate the magnitudes of expected neuronal inputs and neuronal responses, which are the not most important terms enabling the trackability. The last term of Eq. (3.4) may give negative ω_{ij} , which may induce inhibition effects necessary for bump formations. Based on this idea, the couplings used in this study are obtained by the modified energy function

$$E(z) = -2 \sum_{ij} \omega_{ij} \frac{\partial}{\partial z} r^{\text{sample}}(x_i - z) \frac{\partial}{\partial z} r^{\text{sample}}(x_j - z) + \omega_0 \sum_{ij} \omega_{ij}^2, \quad (3.5)$$

where z is a randomly chosen position over the preferred stimulus space and ω_0 is the weight decay that controls the amplitude of ω_{ij} . The function $r^{\text{sample}}(x - z)$ is a sample *bump function* with peak position z .

The optimal ω_{ij} can be obtained by gradient descent with an annealing learning rate [29]. In the n^{th} iteration of the learning process, for a randomly chosen z , we update the coupling strength by

$$\Delta \omega_{ij} = -\eta(n) \frac{\partial E(z)}{\partial \omega_{ij}}, \quad (3.6)$$

where $\eta(n)$ is the annealing learning rate. Truncated cosine functions and Gaussian functions are examples of sample bump functions. Since the position z is randomly chosen on the preferred stimulus space, the obtained couplings should be

$$\omega_{ij} = \frac{1}{\omega_0} \left\langle \frac{\partial}{\partial x_i} r^{\text{sample}}(x_i - z) \frac{\partial}{\partial x_j} r^{\text{sample}}(x_j - z) \right\rangle_z. \quad (3.7)$$

For the 1D case, the sample bump functions are

$$r_1(x - z) = \frac{1}{2} \Theta\left(\frac{\pi}{2} - |x - z|\right) \cos(x - z), \quad (3.8)$$

where $\Theta(x)$ is the step function, and

$$r_2(x - z) = \frac{1}{2} e^{-\frac{(x-z)^2}{2a^2}}, \quad (3.9)$$

where a is the width of the Gaussian function. In this study, a is chosen to be 0.75. The

obtained couplings ω_{ij} are shown in figure 3.1, characteristic of the shape of a Mexican hat. In this plot, neurons with similar preferred stimuli will be positively coupled, while neurons with significantly different preferred stimuli will be negatively coupled.

Analytically, with sample function r_1 , ω_{ij} will be given by

$$\omega_{ij} = \begin{cases} 0, & \text{for } |x_i - x_j| > \pi, \\ \frac{1}{8\omega_0 L} [(\pi - |x_j - x_i|) \cos(x_j - x_i) - \sin(|x_j - x_i|)] & \text{for } |x_i - x_j| \leq \pi, \end{cases} \quad (3.10)$$

where L is the range of the network. By using r_2 , the coupling ω_{ij} reads

$$\omega_{ij} = \frac{1}{L\omega_0\sqrt{\pi}} \left[\frac{1}{2} - \left(\frac{x_i - x_j}{2a} \right)^2 \right] \exp \left[-\frac{|x_i - x_j|^2}{4a^2} \right]. \quad (3.11)$$

These equations are obviously Mexican-hat functions. Note that, by comparing the cases of truncated cosine functions and Gaussian functions, the coupling in the form case has sharp corners at $|x_i - x_j| = 0$ and π . As we shall see, this may cause some differences in their behaviors.

3.2 Tracking Performance

The corresponding external stimulus I^{ext} is defined as

$$I^{\text{ext}}(x_i - z_0) = \alpha r_{1 \text{ or } 2}(x_i - z_0), \quad (3.12)$$

where the constant α is chosen to be 0.3 for the simulations. The stimulus will be placed at $z_0 = 0$ initially. When the system becomes steady, the position of the stimulus will be changed abruptly. After the change, we will observe the change of neuronal input, $U(x, t)$.

In Eq. (3.1), the relation between $r(x_i)$ and $U(x_i)$ is given by

$$r(x_i) = g(U(x_i)) \equiv \Theta(U(x_i)) \frac{kU(x_i)^2}{1 + kU(x_i)^2}, \quad (3.13)$$

where k controls the curvature of the gain functions near the origin and the function Θ is the step function. Note that, when k becomes very large, the gain function tends to a step function.

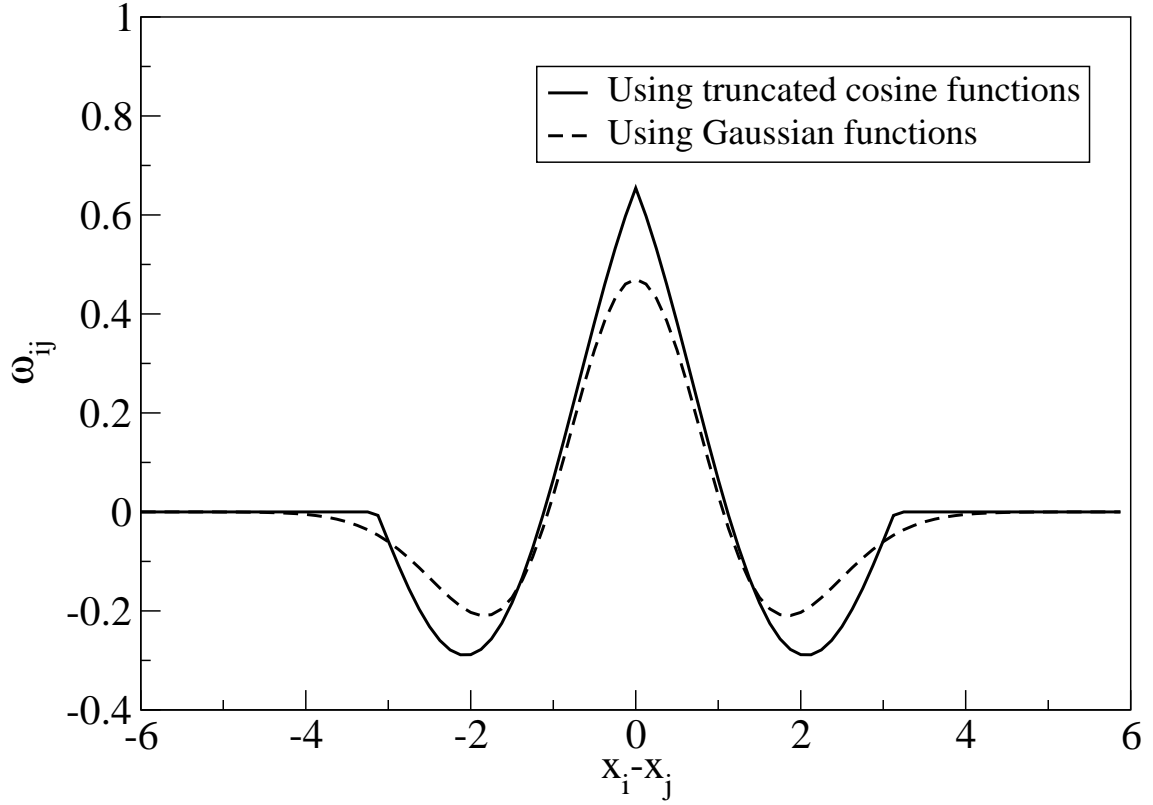


Figure 3.1: The bump functions are of height 0.5, while the Gaussian function is with $a = 0.75$ and $\omega_0 = 0.05$. In the neural network, there are $N = 96$ neurons distributed uniformly over $(-6, 6]$, while the boundary condition is periodic.

In the 1D model simulations, the stimuli are initially at 0 until the neuronal responses become steady. Then the stimulus will shift to a new position z_0 . For different combinations of ω_0 , k and z_0 , the terminal behavior of the steady state of the neuronal response will be different. In the simulations, the behaviors can be categorized into three classes: 1) successful tracking, 2) no tracking and 3) multi-bump solution, namely *spurious solutions*, as shown in figures 3.2-3.4 correspondingly.

In cases of successful tracking, when the jump size of the stimulus is small, because the excitatory effect on the neuronal bump due to the stimulus is asymmetric, the bump will tend to shift its position to catch up with the new position of the stimulus.

For the cases of no tracking, for some larger jump sizes of stimulus, some of the neurons near the new position of the stimulus will only be excited *slightly*, because of the inhibition effect from the bump. Since those slightly excited neurons are negatively coupled with neurons within the bump, the effect of the stimulus will be reduced, as implied by Eq. (3.1).

For an even larger jump size of the position of the stimulus, the neurons near the new position of the stimulus will be excited more significantly, but still small. In figure 3.4, a second bump was excited slightly in the first several τ 's. However, this small second bump is bigger than that in the case of no tracking. The inhibitory effect on the original bump due to the new bump will be larger than the excitatory effect by the stimulus. According to Amari [17], two bumps living in the inhibitory regions of each other will repel each other. So, the original bump will shift to the opposite direction. After the original bump has shifted away, the second bump can grow up.

We study the relation between ω_0 , k and z_0 , and the condition of exciting spurious solutions. The *cutoff of $|z_0|$ for one bump* is defined as the minimum $|z_0|$ such that the shift of the stimulus from 0 to z_0 results in spurious states.

3.2.1 1D ANN with Various Parameters

As shown in figures 3.5 and 3.6, for a large k and truncated cosine bump functions, the cutoff of z_0 for one bump will tend to a constant, since $g(U)$ tends to be a step function. In a latter section of this chapter, we will see that the behavior of 2D ANNs will be different from this. If Gaussian bump functions are used, the cutoff of z_0 for one bump will be larger, as shown in figure 3.7, and the trend is different from that of truncated cosine bump functions. In figure 3.7, we can observe that the cutoff of z_0 for one bump decreases with the value of ω_0 , for the case that the sample functions are Gaussian.

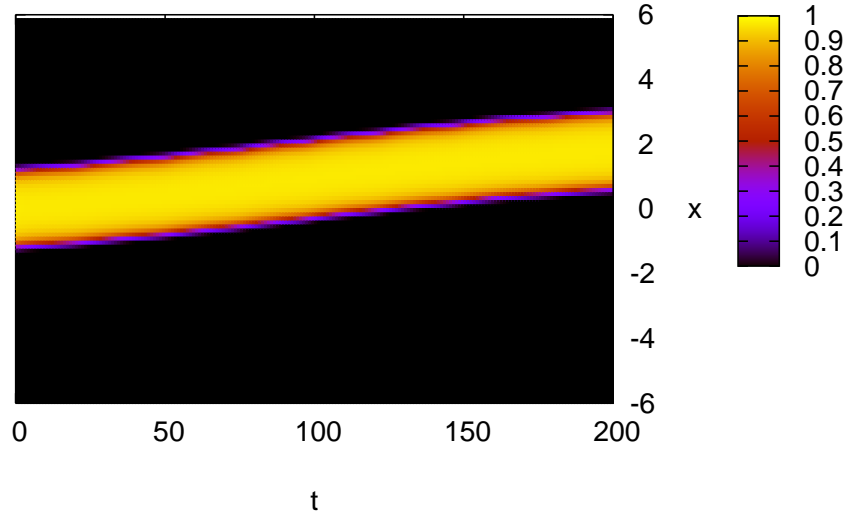


Figure 3.2: Reaction of neuronal responses. The stimulus changed from 0 to 2 at $t = 0$. Parameter: $N = 96, k = 1$. Bump function: truncated cosine.

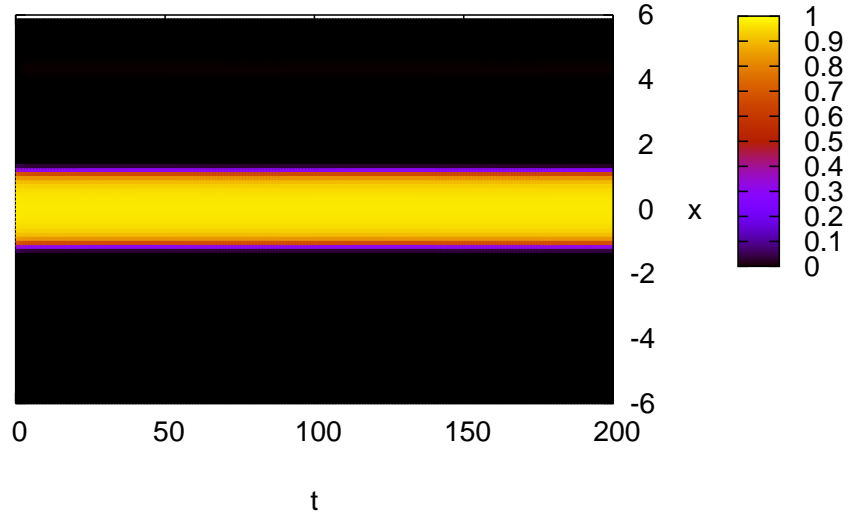


Figure 3.3: Reaction of neuronal responses. The stimulus changed from 0 to 3 at $t = 0$. Parameter: $N = 96, k = 1$. Bump function: truncated cosine.

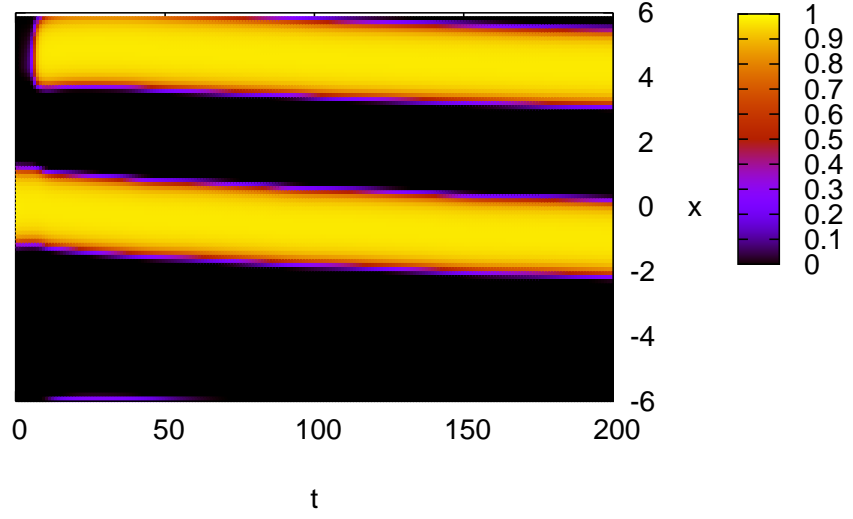


Figure 3.4: Reaction of neuronal responses. The stimulus changed from 0 to 4 at $t = 0$. Parameter: $N = 96, k = 1$. Bump function: truncated cosine.

Because when the range of inhibitory coupling is broader, the position of the new second bump needs to be farther away from the original bump.

The general trends of figures 3.6 and 3.7 are different. For figure 3.6, because the coupling function for truncated cosine function has a sharp turning point at $|x_i - x_j| = \pi$. The existence of the spurious states will depend on the curvature and the sensitivity of the gain function, which in turn depends on k . However, for the coupling for Gaussian sample functions, there is no sharp turning point on the coupling function. So, the sensitivity of the gain function will give a minor effect. The trend of the cutoff of z_0 for one bump will depend on the amplitude of ω_{ij} more.

3.2.2 Trackability with an Abruptly Changed Stimulus

According to figures 3.2-3.4, there should be two cutoffs of $|z_0|$, one between tracking and no tracking, and one from a single bump to spurious states. The cutoff between single bump and spurious states were considered in figures 3.6 and 3.7. Here we consider the cutoff between tracking and no tracking. This is called the *cutoff of $|z_0|$ for tracking*. To

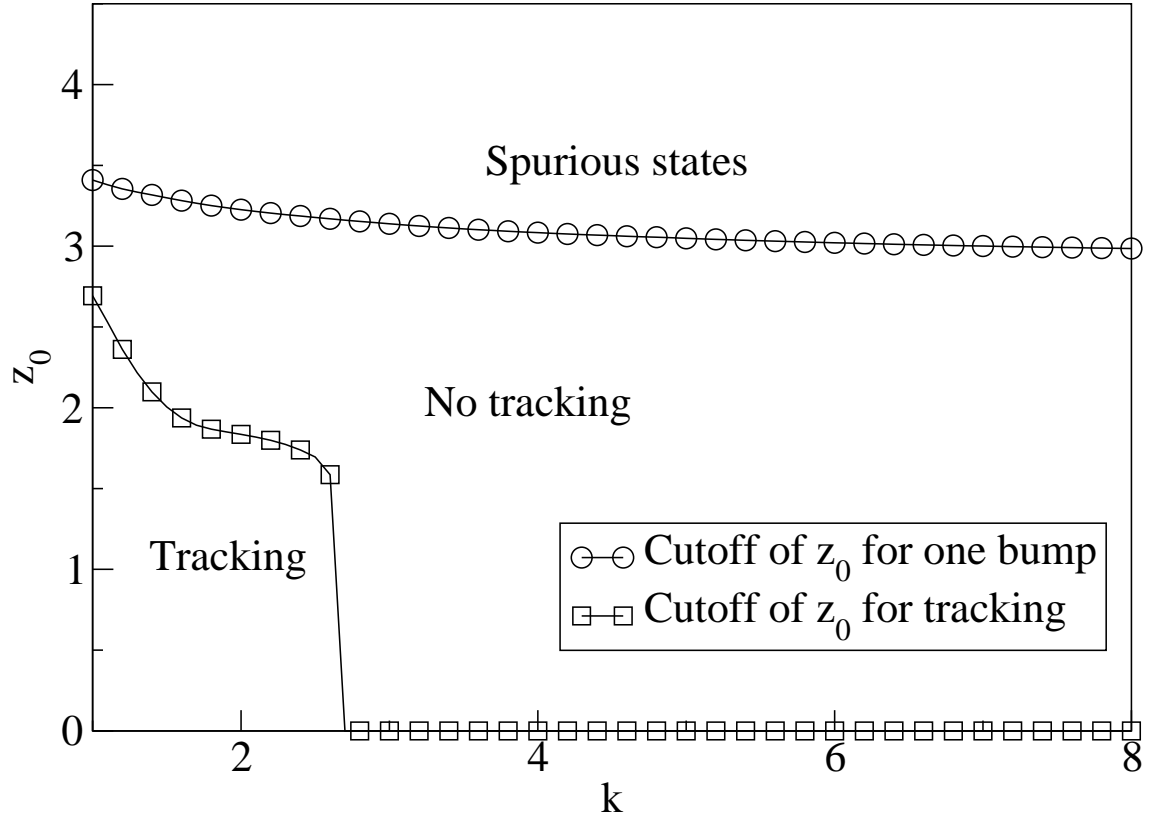


Figure 3.5: The cutoffs of z_0 for one bump and tracking of 1D ANNs with respect to k . Parameter: $\omega_0 = 0.05$. Bump function: truncated cosine. Parameters: range of the network = $(-6, 6]$ and $N = 96$.

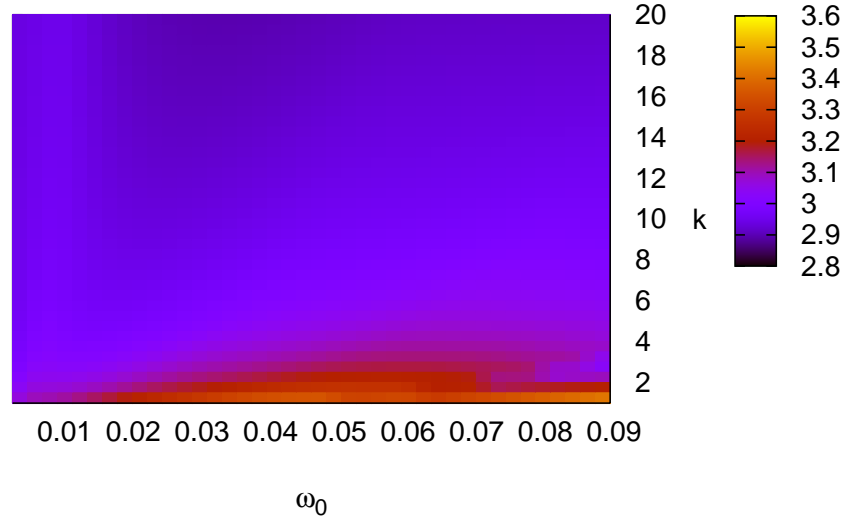


Figure 3.6: The contour plot of cutoff of z_0 for one bump of 1D ANNs for different combinations of ω_0 and k . Parameter: $N = 96$. Bump function: truncated cosine.

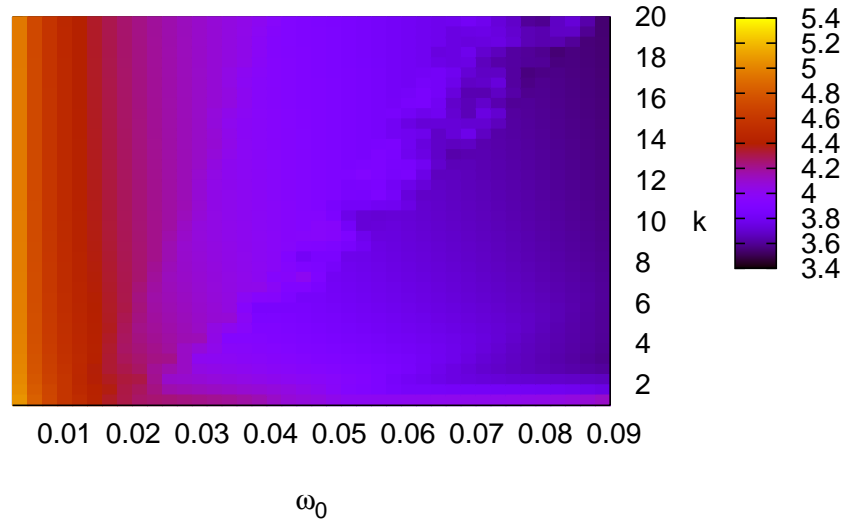


Figure 3.7: The contour plot of cutoff of z_0 for one bump of 1D ANNs for different combinations of ω_0 and k . Parameter: $N = 96$. Bump function: Gaussian.

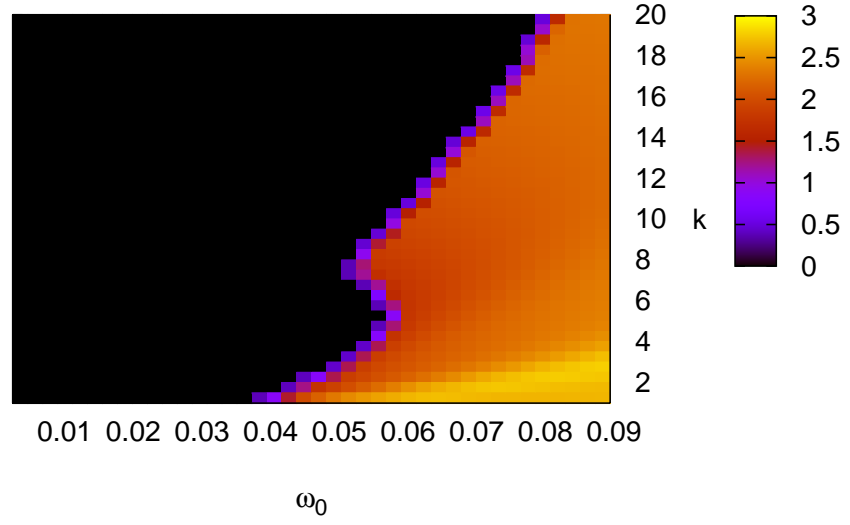


Figure 3.8: Cutoff of z_0 for tracking. The sample bump functions are the truncated cosine. Parameters: the same as figure 3.6.

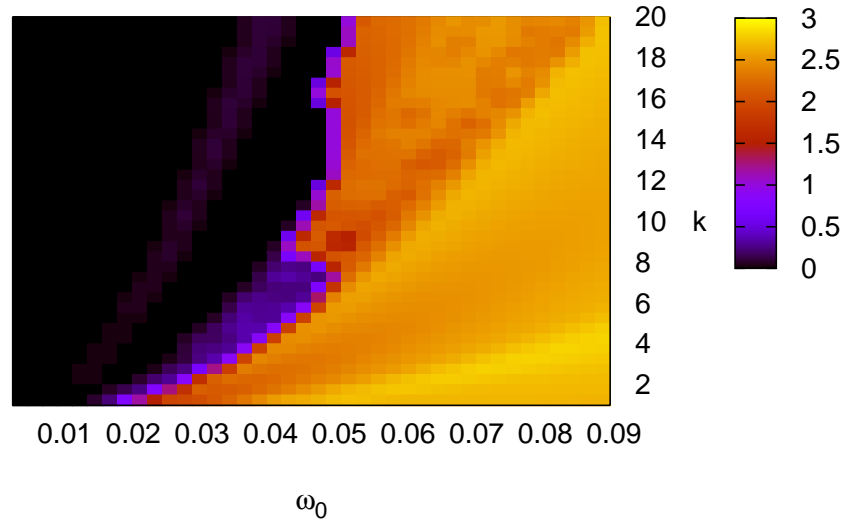


Figure 3.9: Cutoff of z_0 for tracking. The sample bump functions are Gaussian. Parameters: the same as figure 3.7.

facilitate tracking in large number of experiments, we define *tracking* by the conditions: 1) the steady state is a one-bump solution, 2) there is an observable tracking process, i.e. for a given z_0 , the bump can displace at least $z_0/2$, and 3) there is no spurious intermediate states during the process. As shown in figure 3.5, besides the boundary for single bumps, there is a boundary separating the regions of tracking and no tracking.

In figures 3.8 and 3.9, the features of the plots are similar. The system with Gaussian sample function can track at smaller ω_0 , because, for the same ω_0 , the amplitude of the coupling for truncated cosine function is larger than that for Gaussian function, as shown in figure 3.7. When ω_0 is very small, the amplitude of the coupling will be too large. Within these regions, the local excitation will be too large, which will inhibit smaller changes of the bump. As a result, no tracking is observed. Surprisingly, these are kinks near $(\omega_0, k) = (0.05, 7)$ in both plots. These kinks are due to finite size effects of the system. Unlike the system with uniform divisive inhibition, the inhibitory effect is discrete in this system. The kinks should disappear when N becomes very large. Also, small fluctuations are not rare in figures 3.6-3.9. These fluctuations are due to finite size effects. But their magnitudes are of order of the separations between neurons. So, these fluctuations are not related to the inherent properties of the network.

Finite size effect affects not only the smoothness of the plots, but also the tracking process. In figure 3.10, the tracking speed of the bump is oscillating until hitting 0. This oscillation should be due to the rough inhibitory effect. So, if the number of neurons becomes larger, the amplitude of the oscillation is expected to be smaller.

3.3 2D Continuous Attractor Neural Networks with Mexican-Hat Couplings

For the 2D case, the network is covered by $N = N_x \times N_y$ neurons. Their preferred stimuli are represented by \mathbf{x} . The higher dimensional version of Eq. (3.5) is given by

$$E(\mathbf{z}) = -2 \sum_{ij} \omega_{ij} \vec{\nabla}_i r^{\text{sample}}(\mathbf{x}_i - \mathbf{z}) \cdot \vec{\nabla}_j r^{\text{sample}}(\mathbf{x}_j - \mathbf{z}) + \omega_0 \sum_{ij} \omega_{ij}^2. \quad (3.14)$$

From this, the resulting coupling functions will be

$$\omega_{ij} = \frac{1}{\omega_0} \left\langle \vec{\nabla}_i r^{\text{sample}}(\mathbf{x}_i - \mathbf{z}) \cdot \vec{\nabla}_j r^{\text{sample}}(\mathbf{x}_j - \mathbf{z}) \right\rangle_{\mathbf{z}}, \quad (3.15)$$

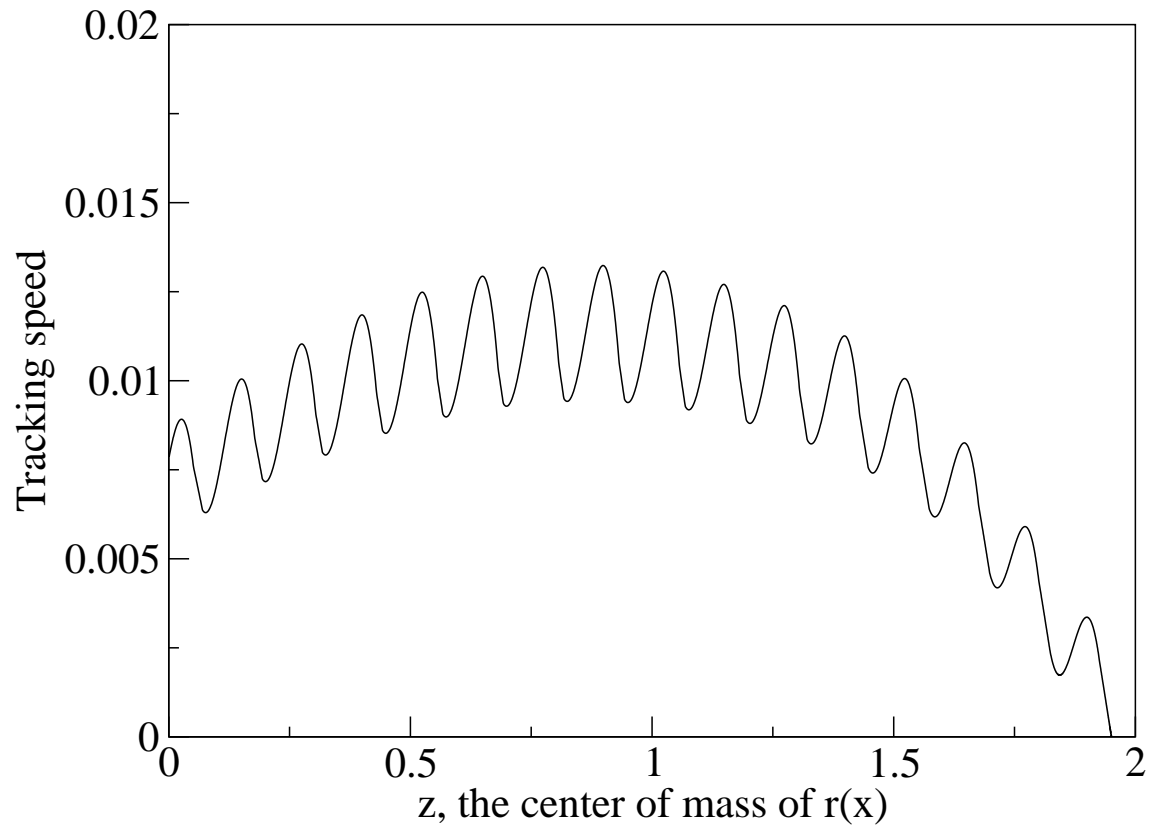


Figure 3.10: Tracking speed vs. position of the bump with different z_0 . Parameters: $N = 96$, $\omega_0 = 0.05$, $k = 1$, range of the network = $(-6, 6)$ and $z_0 = 2$.

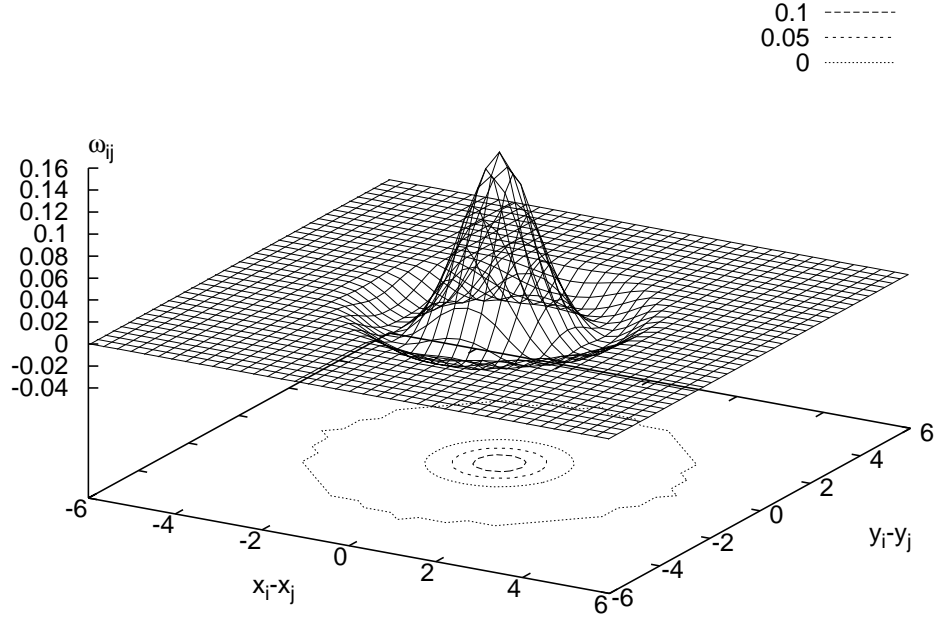


Figure 3.11: The couplings obtained from the truncated cosine functions. The bump functions are of height 0.5. The neural network is a square lattice with periodic boundary condition. There are $N = N_x \times N_y = 40 \times 40$ neurons distributed on $(-2\pi, 2\pi] \times (-2\pi, 2\pi]$.

where $r^{\text{sample}}(\mathbf{x})$ is sample bump functions similar to the 1D case. $r^{\text{sample}}(\mathbf{x})$ will be chosen to be

$$r_1^{2D}(\mathbf{x} - \mathbf{z}) = \frac{1}{2} \Theta \left(\frac{\pi}{2} - |\mathbf{x} - \mathbf{z}| \right) \cos(|\mathbf{x} - \mathbf{z}|), \quad (3.16)$$

where $\Theta(x)$ is the step function, and

$$r_2^{2D}(\mathbf{x} - \mathbf{z}) = \frac{1}{2} e^{-\frac{|\mathbf{x} - \mathbf{z}|^2}{2a^2}}. \quad (3.17)$$

The resulting coupling functions are as shown in figures 3.11 and 3.12. The corresponding external stimulus I^{ext} is defined as

$$I^{\text{ext}}(\mathbf{x}_i - \mathbf{z}_0) = \alpha r^{\text{sample}}(\mathbf{x}_i - \mathbf{z}_0), \quad (3.18)$$

where the external stimulus for 2D case is defined similar to Eq. (3.12), but α is set to be 0.4.

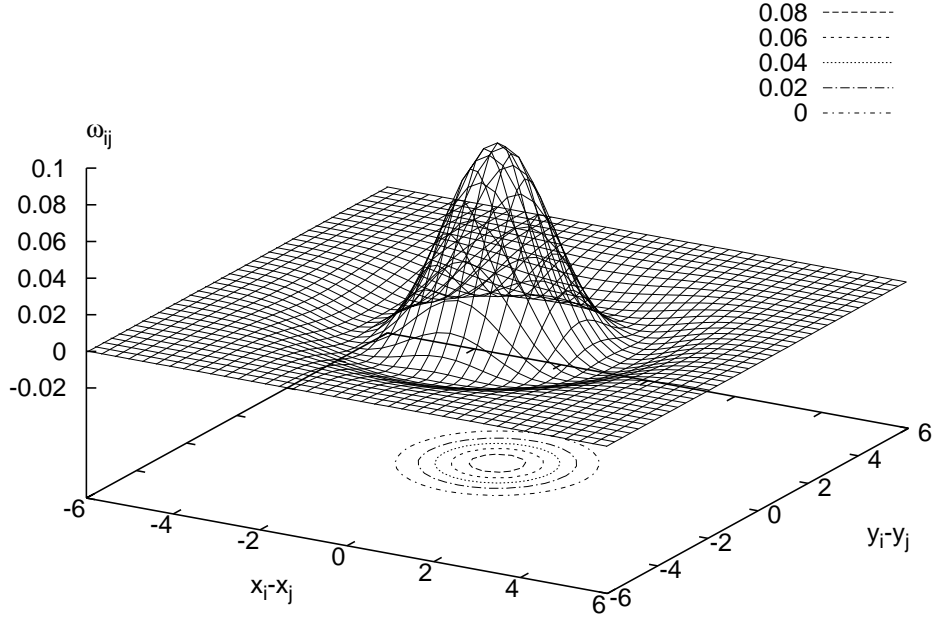


Figure 3.12: The couplings obtained from the Gaussian functions. The bump functions are of height 0.5. Structure and other parameters are the same as figure 3.11.

3.3.1 Instability of 2D CANNs with Mexican Couplings

The plots in figures 3.13 and 3.14 are the 2D counterparts of figures 3.2 and 3.4. The behaviors are similar due to the similar reasoning. In both figures 3.2 and 3.13, the bump can catch up the new position of the stimulus. In both figures 3.4 and 3.14, two bumps will be excited.

When k is small, the bump can track the stimulus, as shown in figure 3.15. When the parameter k became larger, the system will become unstable, as shown in figures 3.16 and 3.17. When k is larger, the response of the neuron due to the neuronal input will become too sensitive. Any small distortions can excite a neuronal response. Therefore, the neural network will not be stable to a one-bump steady state, when k is large.

With the same curvature of the gain function, i.e. same k , the system with couplings obtained by Gaussian sample functions is more stable than that by truncated cosine functions. In figure 3.18, with $k = 3$, the system can still track from $(0,0)$ to $(1,1)$ successfully with Gaussian sample functions. This compares favorably to that with truncated cosine functions, where many bumps are excited as shown in figure 3.16. The stability of the one-bump solution of figure 3.18 is due to the fact that the range

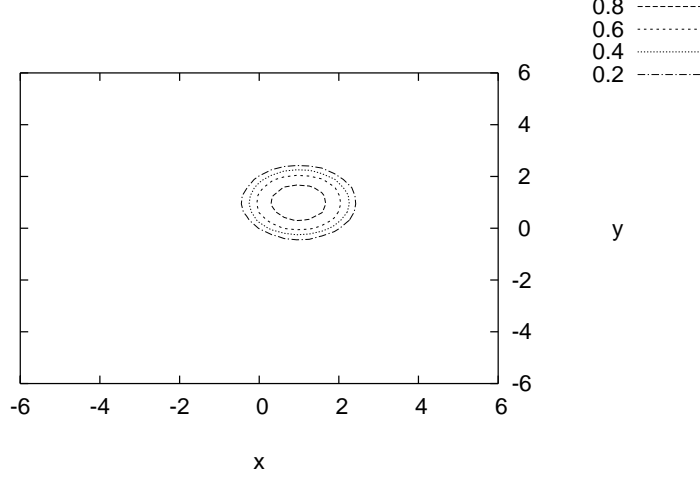


Figure 3.13: Reaction of neuronal responses. The stimulus changed from $(0, 0)$ to $(1, 1)$. Parameter: $N = N_x \times N_y = 40 \times 40$, $k = 2.5$. Bump function: truncated cosine.

of inhibition is larger than the case with truncated cosine sample functions. However, when the curvature is sharp enough, $k = 8$, in figure 3.19, spurious solutions will also be excited, since the gain function is now too sensitive.

3.4 Summary

In this chapter, the behavior of the bump in response to an abruptly changed stimulus is reported. We found that the behavior of the bump is very different if the jump size of the stimulus is different. In summary, there are three kinds of the behaviors, 1) tracking, 2) no tracking but still a stable one-bump solution, and 3) spurious solution. These detailed behaviors are not observed in CANN models with divisive inhibition [26, 28]. Also, in the 1D case, it is found that the space of the attractor is actually not *smooth*. It should be due to the finite size effect of the network. This is the another difference when compared with divisive inhibition models. For the outlook, there are many studies on the case that the gain function is a step function [17]. We have expanded the scope of the studies by considering finite values of k , and it is found the parameter k can also affect the dynamics of the network, as shown above.

In terms of the stability of the one-bump solutions and the trackability of the neuronal input bump, with the couplings we used in this study, the CANNs with Mexican-hat

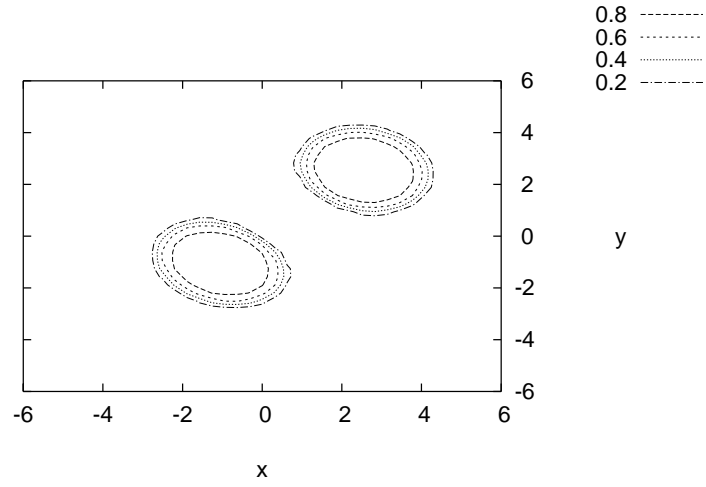


Figure 3.14: Reaction of neuronal responses. The stimulus changed from $(0,0)$ to $(2.26, 2.26)$. Parameter: $N = N_x \times N_y = 40 \times 40, k = 2.5$. Bump function: truncated cosine.

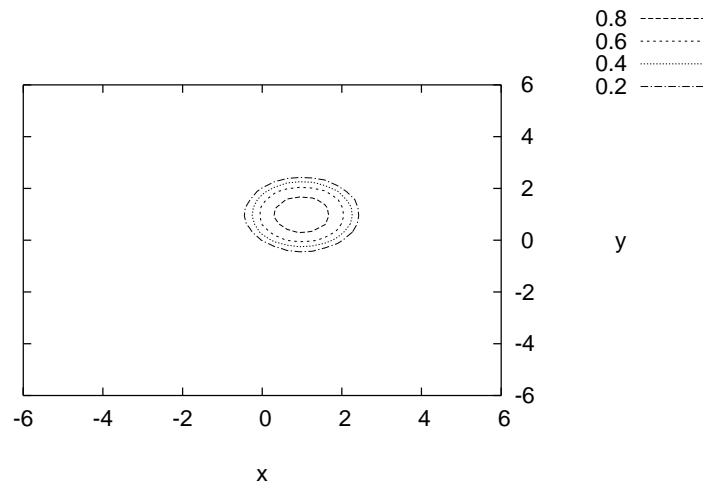


Figure 3.15: Reaction of neuronal responses. The stimulus changed from $(0,0)$ to $(1,1)$. Parameter: $N = N_x \times N_y = 40 \times 40, k = 1$. Bump function: truncated cosine.

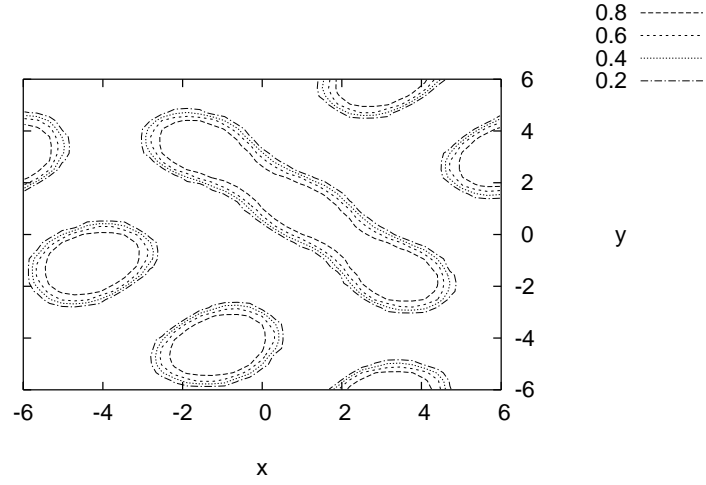


Figure 3.16: Reaction of neuronal responses. The stimulus changed from $(0, 0)$ to $(1, 1)$. Parameter: $N = N_x \times N_y = 40 \times 40, k = 3$. Bump function: truncated cosine.

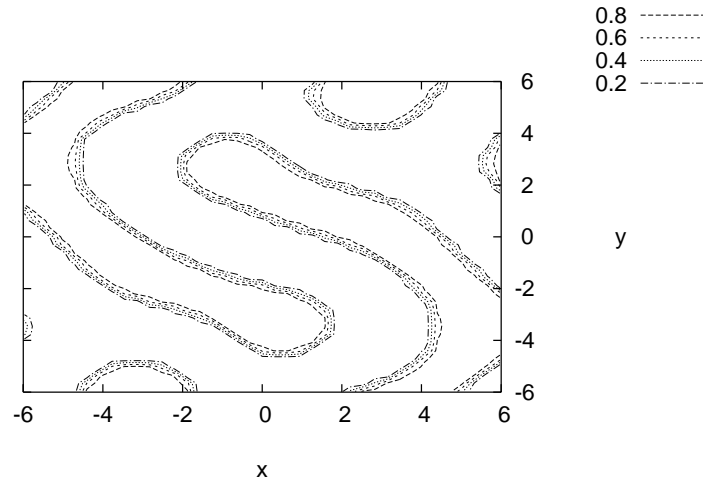


Figure 3.17: Reaction of neuronal responses. The stimulus changed from $(0, 0)$ to $(1, 1)$. Parameter: $N = N_x \times N_y = 40 \times 40, k = 8$. Bump function: truncated cosine.

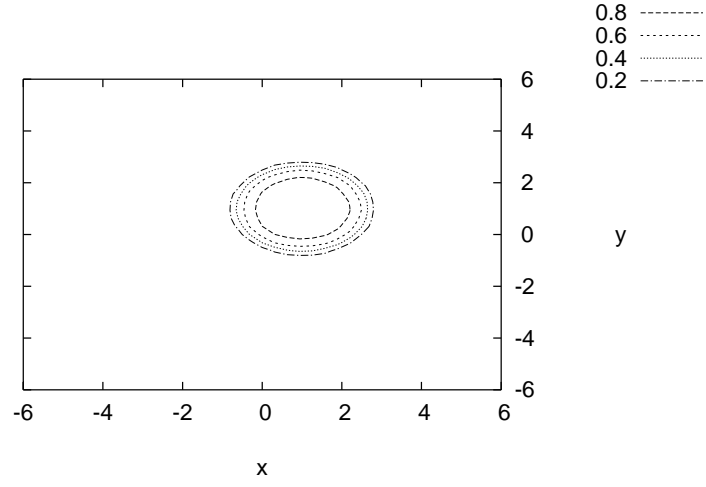


Figure 3.18: Reaction of neuronal responses. The stimulus changed from $(0, 0)$ to $(1, 1)$.
Parameter: $N = N_x \times N_y = 40 \times 40, k = 3$. Bump function: Gaussian.

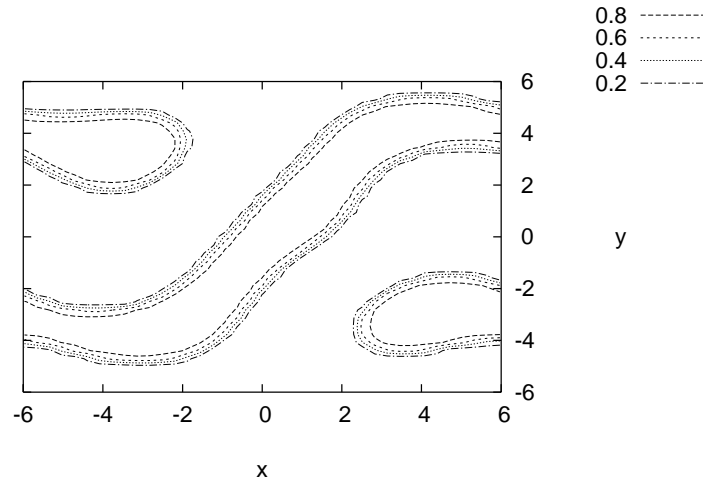


Figure 3.19: Reaction of neuronal responses. The stimulus changed from $(0, 0)$ to $(1, 1)$.
Parameter: $N = N_x \times N_y = 40 \times 40, k = 8$. Bump function: Gaussian.

couplings may not be the best candidates, when compared with CANNs with divisive inhibition. In the previous studies [28, 26] and the next chapter, it can be shown that, the intrinsic dynamics of the model of CANNs with divisive inhibition will guarantee the trackability and stability of one-bump solutions. So, if one prefers a bump-shaped solution to code continuous attractors, CANNs with divisive inhibition is a better choice.

Chapter 4

Dynamics of 2D Continuous Attractor Neural Networks with Divisive Inhibition ¹

4.1 Introduction

As suggested in chapter 1, the study of 2D CANNs is important in understanding of the dynamics of neural systems. In this chapter, we will study a model with divisive inhibition which is similar to the model quoted in chapter 2. Let us consider a two-dimensional neural network coding the stimulus $\mathbf{x} = (x_1, x_2)$, with N neurons evenly distributed over this space. Considering the common case that the range of possible values of the stimulus is much larger than the range of neuronal interactions, we can effectively take $-\infty < x_1, x_2 < \infty$. Similar to Eq. (2.1), the dynamics of the synaptic input $U(\mathbf{x}, t)$ and neuronal response $r(\mathbf{x}, t)$ is given by

$$\tau_s \frac{\partial U(\mathbf{x}, t)}{\partial t} = I^{\text{ext}}(\mathbf{x}) + \rho \int_{-\infty}^{\infty} \int_{-\infty}^{\infty} d\mathbf{x}' J(\mathbf{x}, \mathbf{x}') r(\mathbf{x}') - U(\mathbf{x}, t); \quad (4.1)$$

$$r(\mathbf{x}, t) = \frac{U(\mathbf{x}, t)^2}{1 + k\rho \int_{-\infty}^{\infty} \int_{-\infty}^{\infty} d\mathbf{x}' U(\mathbf{x}', t)^2}, \quad (4.2)$$

where $J(\mathbf{x}, \mathbf{x}')$ is the translationally invariant coupling function defined by

$$J(\mathbf{x}, \mathbf{x}') = \frac{J_0}{2\pi a^2} \exp \left[-\frac{|\mathbf{x} - \mathbf{x}'|^2}{2a^2} \right], \quad (4.3)$$

a is the tuning width of the neural network, k is the global inhibition, and ρ is the density of neurons over the space. When $I^{\text{ext}} = 0$ and $0 < k < k_c \equiv J_0^2 \rho / (32\pi a^2)$, we have the

¹This chapter is an expanded version of [14].

steady solutions given by (see figure 4.1)

$$\tilde{U}(\mathbf{x}|\mathbf{z}) = U_0 \exp \left[-\frac{|\mathbf{x} - \mathbf{z}|^2}{4a^2} \right], \quad (4.4)$$

$$\tilde{r}(\mathbf{x}|\mathbf{z}) = r_0 \exp \left[-\frac{|\mathbf{x} - \mathbf{z}|^2}{2a^2} \right], \quad (4.5)$$

where $U_0 = [1 + (1 - k/k_c)^{1/2}]J_0/(8\pi a^2 k)$ and $r_0 = [1 + (1 - k/k_c)^{1/2}]/(4\pi a^2 k\rho)$. It is notable that Eqs. (4.4) and (4.5) are valid for any \mathbf{z} . So, the stationary state profile can be used to code the preferred stimulus \mathbf{z} over the preferred stimulus space. For simplicity, we consider $I^{\text{ext}} = \alpha U_0 \exp[-|\mathbf{x} - \mathbf{z}_0|^2/(4a^2)]$, where α is the strength of the stimulus. Thanks to the translational invariance of the coupling function, the stationary state solution can be peaked at any point in the space. In this chapter, we consider the network response to a stimulus abruptly changed from $(x_1, x_2) = (0, 0)$ to (z_{01}, z_{02}) at $t = 0$. As shown in the simulation result in figure 4.2, the synaptic input can track the change.

4.2 Solution to the Model

Under the driving of an external stimulus, the network state (i.e, the bump) moves from its initial position to the target one, with its shape distorted during the tracking process. Thus, to describe the tracking performance of a CANN, the key is to know the distortion patterns and their effects on the network dynamics. We denote the the state distortion to be $\delta U(\mathbf{x}, t) \equiv U(\mathbf{x}, t) - \tilde{U}(\mathbf{x}|\mathbf{z})$, whose dynamics is given by linearizing Eq.(1) at $\tilde{U}(\mathbf{x}|\mathbf{z})$, [28, 26]

$$\tau_s \frac{\partial}{\partial t} U(\mathbf{x}, t) = \int_{-\infty}^{\infty} \int_{-\infty}^{\infty} d\mathbf{x}' F(\mathbf{x}, \mathbf{x}'|\mathbf{z}) \delta U(\mathbf{x}', t) - \delta U(\mathbf{x}, t), \quad (4.6)$$

where the interaction kernel $F(\mathbf{x}, \mathbf{x}'|\mathbf{z})$ is

$$\begin{aligned} F(\mathbf{x}, \mathbf{x}'|\mathbf{z}) &= \frac{2\rho\tilde{U}(\mathbf{x}')}{B} \left[J(\mathbf{x}, \mathbf{x}') - k\rho \int_{-\infty}^{\infty} \int_{-\infty}^{\infty} d\mathbf{x}'' J(\mathbf{x}, \mathbf{x}'') \tilde{r}(\mathbf{x}'') \right], \\ &= \frac{2}{\pi a^2} \exp \left[-\frac{|\mathbf{x} - \mathbf{x}'|^2}{2a^2} \right] \exp \left[-\frac{|\mathbf{x}' - \mathbf{z}|^2}{4a^2} \right] \\ &\quad - 2k\rho r_0 \exp \left[-\frac{|\mathbf{x} - \mathbf{z}|^2}{4a^2} \right] \exp \left[-\frac{|\mathbf{x}' - \mathbf{z}|^2}{4a^2} \right]. \end{aligned} \quad (4.7)$$

where $B = 1 + k\rho \int_{-\infty}^{\infty} \int_{-\infty}^{\infty} \tilde{U}(\mathbf{x}'|\mathbf{z})^2 d\mathbf{x}'$ is a constant. The network dynamics is determined by the eigenfunctions and eigenvalues of the kernel $F(\mathbf{x}, \mathbf{x}'|\mathbf{z})$. To compute them, we choose the eigenfunctions of the quantum harmonic oscillator as the basis. While the

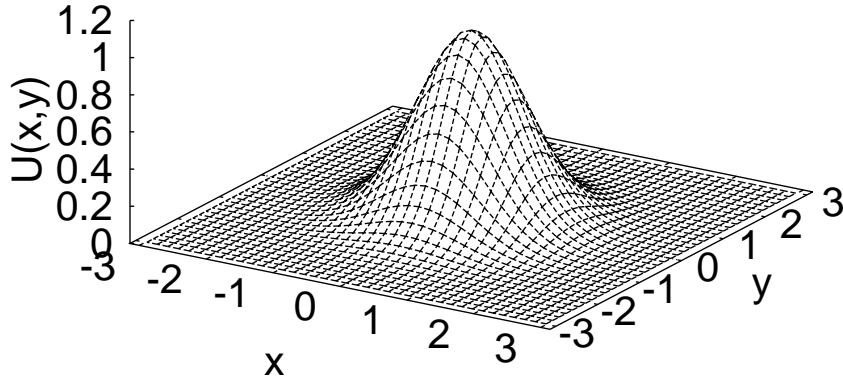


Figure 4.1: A stationary state $\tilde{U}(\mathbf{x}, 0)$. Parameters: $N = 40 \times 40$, $a = 0.5$, $k = 0.5$, $\tau_s = 1$ and $\rho = N/(2\pi)^2$.

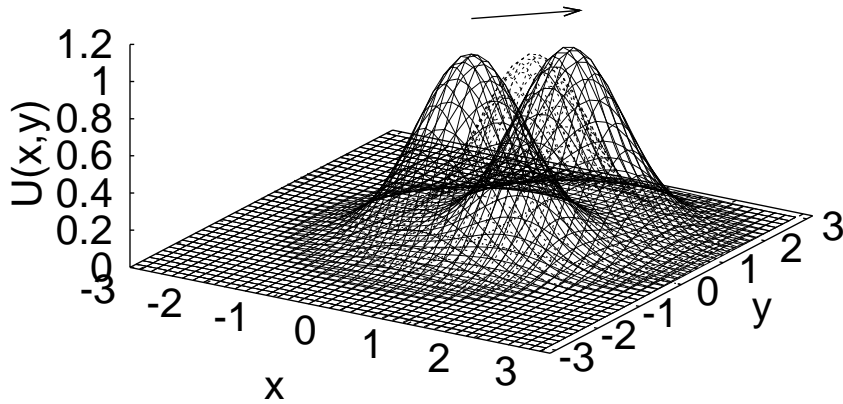


Figure 4.2: The synaptic input in the space due to the abruptly changed stimulus. Parameters: $\alpha = 0.05$, $\mathbf{z}_0(t < 0) = 0$, $\mathbf{z}_0(t \geq 0) = (1, 1)$ and the rest are the same as figure 4.1.

results are more clearly presented using basis functions in polar coordinates, the analysis is more conveniently done in the rectangular coordinates. Hence we will describe the basis functions in both coordinates.

4.2.1 Using Basis Functions in Rectangular Coordinates

Under the rectangular coordinates, the basis functions are

$$u_{n,m}(\mathbf{x}|\mathbf{z}) = \sqrt{\frac{1}{2\pi a^2 m! n! 2^{n+m}}} H_n\left(\frac{x_1 - z_1}{\sqrt{2a}}\right) H_m\left(\frac{x_2 - z_2}{\sqrt{2a}}\right) \exp\left[-\frac{|\mathbf{x} - \mathbf{z}|^2}{4a^2}\right], \quad (4.8)$$

where $H_n(x)$ is the n^{th} order Hermite Polynomial [27]. By the completeness of the basis functions, we have

$$U(\mathbf{x}, t) = \tilde{U}(\mathbf{x}|\mathbf{z}(t)) + \sum_{n,m} a_{n,m}(t) u_{n,m}(\mathbf{x}|\mathbf{z}(t)). \quad (4.9)$$

Using Eq. (4.9), the left-hand side of Eq. (4.6) will become

$$\begin{aligned} \tau_s \frac{\partial U}{\partial t} &= \sqrt{2\pi} a U_0 \frac{\tau_s}{2a} \left(\frac{dz_1}{dt} u_{10} + \frac{dz_2}{dt} u_{01} \right) \\ &\quad + \tau_s \sum_{n,m} (a'_{n,m}(t) u_{n,m}(\mathbf{x}|\mathbf{z}(t)) + a_{n,m}(t) u'_{n,m}(\mathbf{x}|\mathbf{z}(t))) \\ &= \sqrt{2\pi} a U_0 \frac{\tau_s}{2a} \left(\frac{dz_1}{dt} u_{10} + \frac{dz_2}{dt} u_{01} \right) + \tau_s \sum_{n,m} a'_{n,m}(t) u_{n,m} \\ &\quad + \sum_{n,m} a_{n,m}(t) \left\{ \frac{\tau_s}{2a} \frac{dz_1}{dt} (\sqrt{n-1} u_{n-1,m} - \sqrt{n} u_{n+1,m}) \right. \\ &\quad \left. + \frac{\tau_s}{2a} \frac{dz_2}{dt} (\sqrt{m-1} u_{n,m-1} - \sqrt{m} u_{n,m+1}) \right\} \\ &= \sum_{n,m} \left\{ \tau_s \frac{da_{n,m}}{dt} + \frac{\tau_s}{2a} \frac{dz_1}{dt} \left[\sqrt{2\pi} a U_0 \delta_{n1,m0} + \sqrt{n} a_{n-1,m}(t) - \sqrt{n+1} a_{n+1,m}(t) \right] \right. \\ &\quad \left. + \frac{\tau_s}{2a} \frac{dz_2}{dt} \left[\sqrt{2\pi} a U_0 \delta_{n0,m1} + \sqrt{m} a_{n,m-1}(t) - \sqrt{m+1} a_{n,m+1}(t) \right] \right\} u_{n,m}, \quad (4.10) \end{aligned}$$

while the right-hand side will be

$$\begin{aligned}
& I^{\text{ext}}(\mathbf{x}) + \int d\mathbf{x}' F(\mathbf{x}, \mathbf{x}'|\mathbf{z}) \delta U(\mathbf{x}') - \delta U(\mathbf{x}') \\
&= \sum_{n,m} I_{n,m} u_{n,m} + \sum_{n,m} u_{nm} \int d\mathbf{x} u_{nm}(\mathbf{x}|\mathbf{z}) \int d\mathbf{x}' F(\mathbf{x}, \mathbf{x}'|\mathbf{z}) \sum_{n',m'} a_{n',m'} u_{n'm'}(\mathbf{x}'|\mathbf{z}) \\
&\quad - \sum_{n,m} a_{n,m} u_{n,m} \\
&= \sum_{n,m} \left[I_{n,m} + \sum_{n',m'} \mathcal{F}_{n,m,n',m'} a_{n',m'}(t) - a_{n,m} \right] u_{n,m}. \tag{4.11}
\end{aligned}$$

Thanks to the orthonormality of the basis functions, we have derived

$$\begin{aligned}
\tau_s \frac{da_{n,m}}{dt} &= I_{n,m} + \sum_{n',m'} \mathcal{F}_{n,m,n',m'} a_{n',m'}(t) - a_{n,m} \\
&\quad - \frac{\tau_s}{2a} \frac{dz_1}{dt} \left[\sqrt{2\pi} a U_0 \delta_{n1,m0} + \sqrt{n} a_{n-1,m}(t) - \sqrt{n+1} a_{n+1,m}(t) \right] \\
&\quad - \frac{\tau_s}{2a} \frac{dz_2}{dt} \left[\sqrt{2\pi} a U_0 \delta_{n0,m1} + \sqrt{m} a_{n,m-1}(t) - \sqrt{m+1} a_{n,m+1}(t) \right], \tag{4.12}
\end{aligned}$$

where $I_{n,m}$ is the projection of I^{ext} onto $u_{n,m}$, given by

$$I_{n,m}(\mathbf{x}|\mathbf{z}_0) = \alpha U_0 \sqrt{\frac{2\pi a^2}{n!m!}} \left(\frac{z_{01} - z_1}{2a} \right)^n \left(\frac{z_{02} - z_2}{2a} \right)^m \exp \left[-\frac{|\mathbf{z} - \mathbf{z}_0|^2}{8a^2} \right], \tag{4.13}$$

and $\mathcal{F}_{n,m,n',m'}$, the interaction matrix (see Appendix A), is given by

$$\mathcal{F}_{0,0,0,0} = 1 - \left(1 - \frac{k}{k_c} \right)^{\frac{1}{2}}, \tag{4.14}$$

$$\begin{aligned}
\mathcal{F}_{n,m,n',m'} &= \sqrt{\frac{m'!n'!}{m!n!}} \frac{2}{2^{m'+n'}} \frac{(-)^{\frac{m'+n'-m-n}{2}}}{2^{\frac{m'+n'-m-n}{2}} (\frac{m'-m}{2})! (\frac{n'-n}{2})!}, \\
&\quad \text{if } \frac{n'-n}{2} \text{ and } \frac{m'-m}{2} \text{ are positive integers} \tag{4.15}
\end{aligned}$$

$$\mathcal{F}_{n,m,n',m'} = 0, \quad \text{otherwise.} \tag{4.16}$$

The center of mass is given by the self-consistent condition

$$\mathbf{z}(t) = \frac{\iint d\mathbf{x} \mathbf{x} U(\mathbf{x}, t)}{\iint d\mathbf{x} U(\mathbf{x}, t)}. \tag{4.17}$$

If the external stimulus is symmetric with respect to the x -axis, then $dz_2/dt = 0$ and

$$\frac{dz_1}{dt} = \frac{2a}{\tau_s} \frac{\sum_{\text{odd } n, \text{ even } m} \sqrt{\frac{(m-1)!!}{m!!} \frac{n!!}{(n-1)!!}} \left(I_{n,m} + \sum_{n',m'} \mathcal{F}_{n,m,n',m'} a_{n',m'} \right)}{\sqrt{2\pi} a U_0 + \sum_{\text{even } n, m} \sqrt{\frac{(m-1)!!}{m!!} \frac{(n-1)!!}{n!!}} a_{n,m}} \quad (4.18)$$

(see Appendix B). The eigenvalues of \mathcal{F} are $\lambda_{0,0} = 1 - (1 - k/k_c)^{1/2}$, $\lambda_{n,0} = \lambda_n$ for $n \neq 0$, $\lambda_{0,m} = \lambda_m$ for $m \neq 0$, $\lambda_{n,m} = \lambda_n \lambda_m$ for $n \neq 0$ and $m \neq 0$, where $\lambda_n = 2/2^n$. From this result, one can conclude that, if the stimulus is absent, all modes of distortion will decay exponentially in time, except for the eigenfunctions $u_{1,0}$ and $u_{0,1}$, whose eigenvalues are 1. To prove this, we define $v_{n,m}^R(\mathbf{x}|\mathbf{z})$ to be the right eigenfunctions of \mathcal{F} . Then we may express $\delta U(\mathbf{x}, t)$ in Eq. (4.6) as $\delta U(\mathbf{x}, t) = \sum_{n,m} \delta U_{n,m}(\mathbf{z}, t) v_{n,m}^R(\mathbf{x}|\mathbf{z})$. Using the orthonormality of the left and right eigenfunctions of $F(\mathbf{x}, \mathbf{x}'|\mathbf{z})$, we have

$$\delta U_{n,m}(z, t) = \int_{-\infty}^{\infty} \int_{-\infty}^{\infty} d\mathbf{x} \delta U(\mathbf{x}, t) v_{n,m}^L(\mathbf{x}|\mathbf{z}). \quad (4.19)$$

Assume that the motion of the bump is slow, so that $d\mathbf{z}/dt$ becomes negligible in Eq. (4.6); as we shall see, this assumption is valid as long as the external stimulus is sufficiently weak. Then, the projection of Eq. (4.6) on the eigenfunctions become

$$\tau_s \frac{d}{dt} \delta U_{n,m}(\mathbf{z}, t) = (\lambda_{n,m} - 1) \delta U_{n,m}(z, t). \quad (4.20)$$

Hence,

$$\delta U_{n,m}(\mathbf{z}, t) = \delta U_{n,m}(\mathbf{z}, 0) \exp \left[-\frac{(1 - \lambda_{n,m})t}{\tau_s} \right], \quad (4.21)$$

where $\delta U_{n,m}(\mathbf{z}, 0)$ is the initial value of the projection. $u_{1,0}$ and $u_{0,1}$ correspond to the trackability of the synaptic input as well as the neuronal response, because $u_{1,0} \sim \partial \tilde{U} / \partial x_1$ and $u_{0,1} \sim \partial \tilde{U} / \partial x_2$. $u_{1,0}$ and $u_{0,1}$ are the modes of the position shift of the synaptic input. Thus, it guarantees the stability of the stationary solution and trackability of the synaptic input.

We are now ready to find the tracking solution to the stimulus abruptly changed from $(0, 0)$ to $(z_{01}, 0)$ at $t = 0$. Suppose the shape of neuronal input bump remains unchanged. Then, $U(\mathbf{x}, t) = \tilde{U}(\mathbf{x} - \mathbf{z})$. Neglecting the dependence on all $a_{n,m}$ and $I_{n,m}$ in Eq. (4.18), except $I_{0,1}$, we have

$$\frac{dz_1}{dt} = \frac{\alpha}{\tau_s} (z_{01} - z_1) \exp \left[-\frac{(z_{01} - z_1)^2}{8a^2} \right], \quad (4.22)$$

which is consistent with the result obtained from the one-dimensional case, namely the

weak stimulus approximation [28, 26]. This approximation is useful when $|\mathbf{z} - \mathbf{z}_0|$ is small and the stimulus is weak. It also shows that the tracking behavior is similar to the one-dimensional case.

4.2.2 Using Basis Functions in Polar Coordinates

Since the system is also rotationally invariant, the analysis can proceed by using the eigenfunctions in polar coordinates. The eigenfunctions of the quantum harmonic oscillators are

$$\psi_{l,j}(r, \theta) = \sqrt{\frac{(\frac{l-j}{2})!(\frac{l+j}{2})!}{2\pi a}} \left[\sum_{t=0}^{\frac{l-|j|}{2}} \frac{(-1)^t (\frac{r}{\sqrt{2a}})^t}{(\frac{l-j}{2})!(\frac{l+j}{2})!t!} \right] e^{-\frac{r^2}{4a^2} + ij\theta}, \quad (4.23)$$

where $i = \sqrt{-1}$, and l, j are the radial and angular quantum numbers respectively. Decomposing the distortional terms, we have $\delta U = \sum_{l,j} b_{l,j}(t) \psi_{l,j}$. The matrix elements of the transformation matrix are

$$[T]_{n,m,l,j} \equiv \langle u_{n,m} | \psi_{l,j} \rangle = i^m \sqrt{\frac{(\frac{l+j}{2})!(\frac{l-j}{2})!}{n!m!2^l}} \left[\sum_t (-1)^t \binom{m}{t} \binom{n}{\frac{l-j}{2} - t} \right]. \quad (4.24)$$

Similar to Eq. (4.12), there is an interaction kernel \mathcal{G} that represents the interaction between different $\psi_{l,j}$, which can be obtained by $\mathcal{G} = T^{-1} \mathcal{F} T$. The part of \mathcal{G} with small l is

$$\mathcal{G} = \begin{pmatrix} \lambda_{00} & 0 & -1 & 0 & & & & \\ & 1 & & & 0 & -\frac{1}{\sqrt{8}} & 0 & 0 \\ & & 1 & & 0 & 0 & -\frac{1}{\sqrt{8}} & 0 \\ & & & \frac{1}{2} & & & & \\ & & & & \frac{1}{2} & & & \dots \\ & & & & & \frac{1}{2} & & \\ & & & & & & \frac{1}{4} & \\ & & & & & & & \frac{1}{4} \\ & & & & & & & & \frac{1}{4} \\ & & & & & & & & & \frac{1}{4} \\ & & & & & & & & & & \ddots \end{pmatrix}. \quad (4.25)$$

The first few eigenfunctions of \mathcal{G} are

$$\Psi_{00} = \psi_{00}, \quad (4.26)$$

$$\Psi_{1\pm 1} = \psi_{1\pm 1}, \quad (4.27)$$

$$\Psi_{20} = \frac{1}{\sqrt{1 + (\lambda_{00} - 1/2)^2}} [\psi_{00} + (\lambda_{00} - 1/2)\psi_{20}], \quad (4.28)$$

$$\Psi_{2\pm 2} = \psi_{2\pm 2}, \quad (4.29)$$

$$\Psi_{3\pm 1} = \frac{1}{\sqrt{3^2 + 2}} \left[\sqrt{2}\psi_{1\pm 1} + 3\psi_{3\pm 1} \right], \text{ and} \quad (4.30)$$

$$\Psi_{3\pm 3} = \psi_{3\pm 3}, \quad (4.31)$$

where the indices l and j of $\Psi_{l,j}$ represent the highest basis function it contains. Their eigenvalues are λ_{00} , 1, 1/2, 1/2, 1/4, and 1/4 respectively.

As shown in figures 4.3 to 4.8, the eigenfunctions are symmetric with respect to the origin. The eigenfunctions correspond to different modes of the distortion of the synaptic input during the motion. Ψ_{00} corresponds to the change in height. It can describe, say, the reduction of the bump height during the process to catch up with the new position of the stimulus, as shown in figure 4.2. $\Psi_{1,\pm 1}$ can describe the movement of the bump with respect to the center of mass. $\Psi_{2,0}$ describes not only changes in the height of the bump, but also changes in the width of the bump during the motion. $\Psi_{3,\pm 1}$ describes the skewing of the bump due to the stimulus and other modes. While the above distortion modes are apparently extensions of those in the one-dimension case, the modes $\Psi_{2,\pm 2}$ and $\Psi_{3,\pm 3}$ are unique to the two-dimensional case. The former corresponds to an elliptical distortion of the bump shape, and the latter to a three-fold distortion. In fact, $\Psi_{l\pm l}$ are the eigenfunctions with eigenvalues $1/2^{l-1}$ (see Appendix C).

By using the transformation matrix in Eq. (4.24), Eq. (4.12) can be transformed from rectangular to polar coordinates up to arbitrary order. For the perturbation up to $l = 3$, and for external stimuli symmetric with respect to the x -axis, we have

$$\left(\tau_s \frac{d}{dt} + 1 - \lambda_{00} \right) b_{00} = I_{00} - \tau_s \frac{dR}{dt} \left[-\frac{1}{\sqrt{8}a} (b_{1-1} + b_{1+1}) - \frac{1}{2a} (b_{31} + b_{3-1}) \right] - b_{20}, \quad (4.32)$$

$$\tau_s \frac{d}{dt} b_{1\pm 1} = I_{1\pm 1} - \tau_s \frac{dR}{dt} \left(\frac{\sqrt{2}\pi a U_0 + b_{00}}{2\sqrt{2}a} - \frac{1}{2\sqrt{2}a} b_{20} - \frac{1}{2a} b_{2\pm 2} \right) - \frac{1}{\sqrt{8}} b_{3\pm 1}, \quad (4.33)$$

$$\left(\tau_s \frac{d}{dt} + \frac{1}{2} \right) b_{20} = I_{20} - \tau_s \frac{dR}{dt} \left(-\frac{1}{2\sqrt{2}a} (b_{1-1} + b_{1+1}) - \frac{1}{2a} (b_{31} + b_{3-1}) \right), \quad (4.34)$$

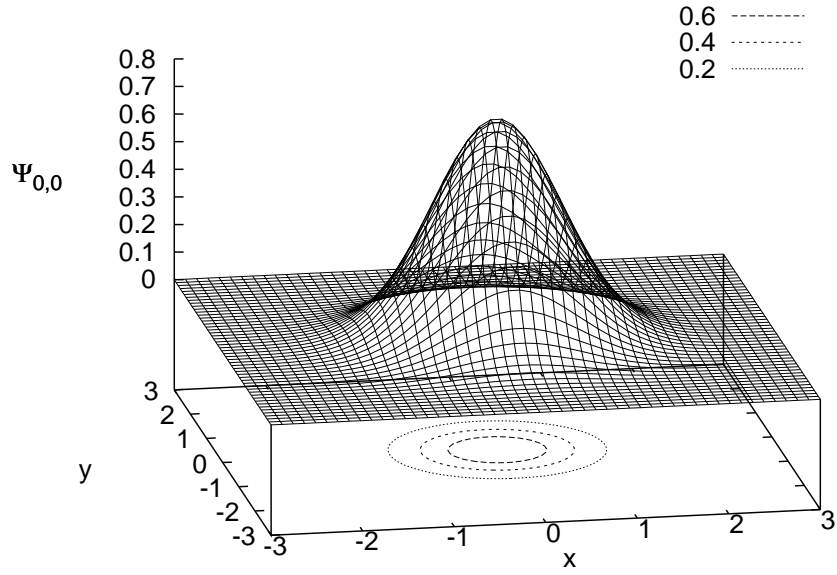


Figure 4.3: Real part of the eigenfunction $\Psi_{0,0}$.

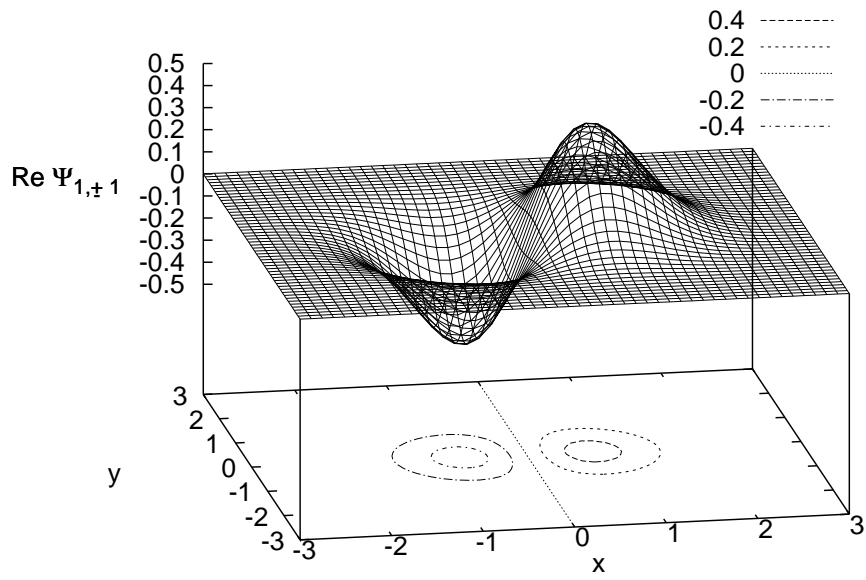


Figure 4.4: Real part of the eigenfunction $\Psi_{1,\pm 1}$.

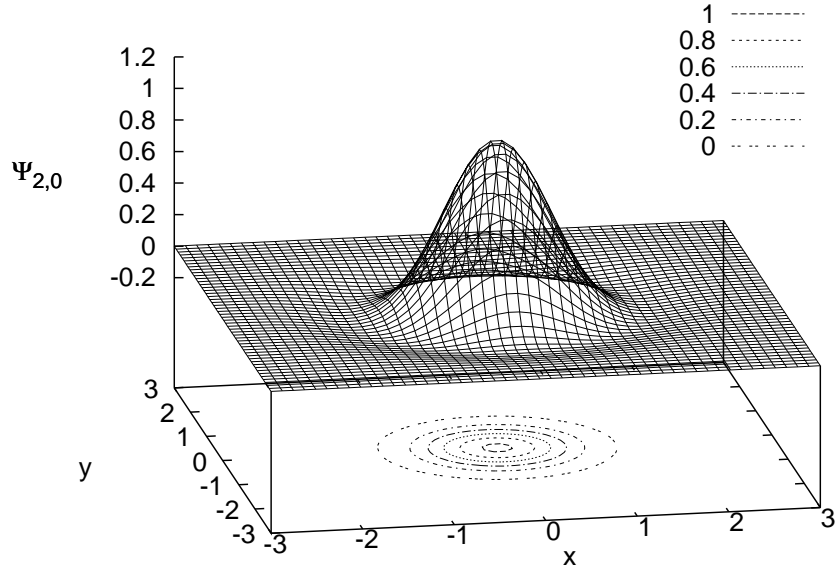


Figure 4.5: Real part of the eigenfunction $\Psi_{2,0}$.

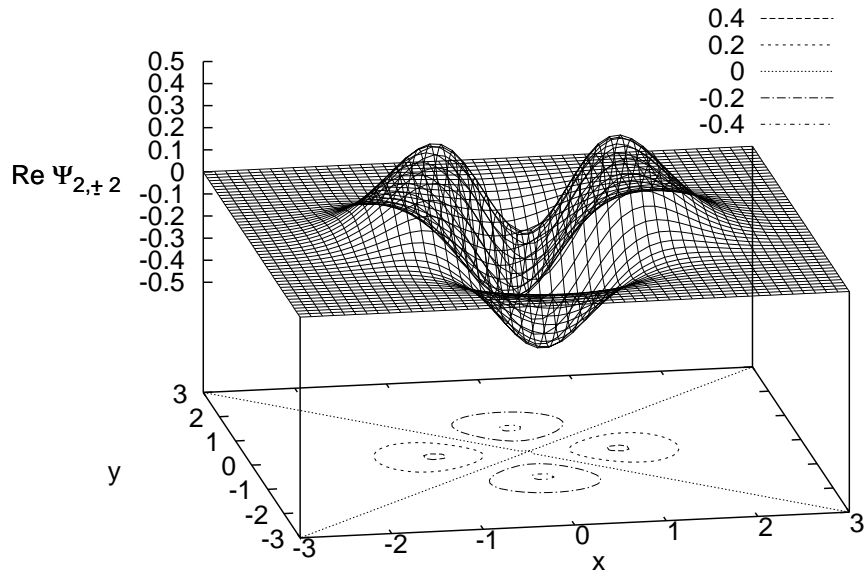


Figure 4.6: Real part of the eigenfunction $\Psi_{2,\pm 2}$.

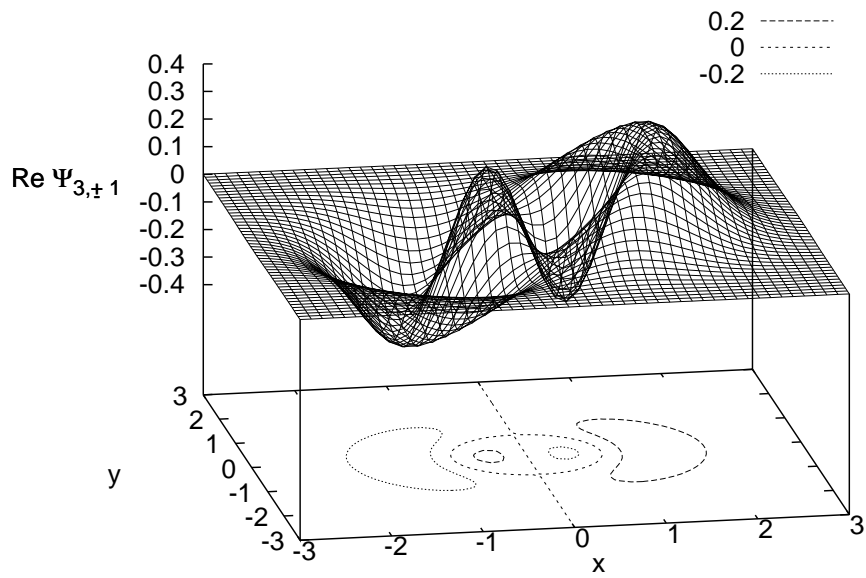


Figure 4.7: Real part of the eigenfunction $\Psi_{3,\pm 1}$.

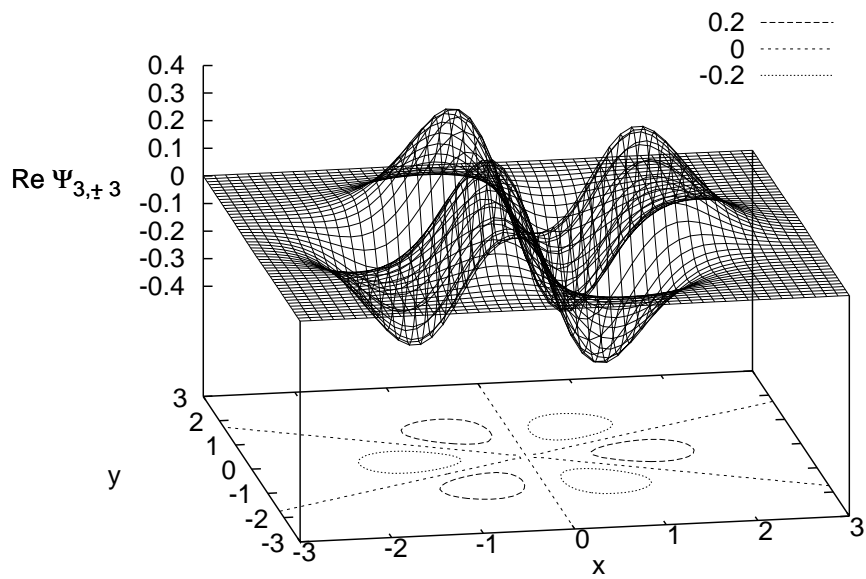


Figure 4.8: Real part of the eigenfunction $\Psi_{3,\pm 3}$.

$$\left(\tau_s \frac{d}{dt} + \frac{1}{2}\right) b_{2\pm 2} = I_{2\pm 2} - \tau_s \frac{dR}{dt} \left(\frac{1}{2a} b_{1\pm 1} - \frac{\sqrt{3}}{\sqrt{8}a} b_{3\pm 3} - \frac{1}{\sqrt{8}a} b_{3\pm 1} \right), \quad (4.35)$$

$$\left(\tau_s \frac{d}{dt} + \frac{3}{4}\right) b_{3\pm 1} = I_{3\pm 1} - \tau_s \frac{dR}{dt} \left(-\frac{1}{4a} b_{20} - \frac{1}{\sqrt{8}a} b_{2\mp 2} \right) \quad (4.36)$$

$$\left(\tau_s \frac{d}{dt} + \frac{3}{4}\right) b_{3\pm 3} = I_{3\pm 3} - \tau_s \frac{dR}{dt} \left(\frac{\sqrt{3}}{\sqrt{8}a} b_{2\pm 2} \right) \quad (4.37)$$

$$b_{1\pm 1} = -\sqrt{2} b_{3\pm 1} \quad (4.38)$$

$$\tau \frac{dR}{dt} = 2\sqrt{2}a \frac{I_{11} + \sqrt{2}(I_{31} - b_{31})}{\sqrt{2\pi}aU_0 + b_{00} - \sqrt{2}b_{20} - 2\sqrt{2}b_{22}}, \quad (4.39)$$

where R is the radial distance from the origin. Note that $I_{l,j} = I_{l,-j}$ and $b_{l,j} = b_{l,-j}$ due to the symmetry when the stimulus lies on the x -axis. In Eqs. (4.32)-(4.39), I_{lj} 's are given by

$$I_{00} = \alpha U_0 \sqrt{2\pi} a \exp \left[-\frac{|\mathbf{z} - \mathbf{z}_0|^2}{8a^2} \right], \quad (4.40)$$

$$I_{1\pm 1} = \frac{1}{2} \alpha U_0 \sqrt{\pi} (R_0 - R) \exp \left[-\frac{|\mathbf{z} - \mathbf{z}_0|^2}{8a^2} \right], \quad (4.41)$$

$$I_{20} = \frac{1}{8a} \alpha U_0 \sqrt{2\pi} (R_0 - R)^2 \exp \left[-\frac{|\mathbf{z} - \mathbf{z}_0|^2}{8a^2} \right], \quad (4.42)$$

$$I_{2\pm 2} = \frac{1}{8a} \alpha U_0 \sqrt{\pi} (R_0 - R)^2 \exp \left[-\frac{|\mathbf{z} - \mathbf{z}_0|^2}{8a^2} \right], \quad (4.43)$$

$$I_{3\pm 1} = \frac{1}{8a^2} \alpha U_0 \sqrt{\pi} (R_0 - R)^3 \exp \left[-\frac{|\mathbf{z} - \mathbf{z}_0|^2}{8a^2} \right], \quad (4.44)$$

$$I_{3\pm 3} = \frac{1}{8\sqrt{3}a^2} \alpha U_0 \sqrt{\pi} (R_0 - R)^3 \exp \left[-\frac{|\mathbf{z} - \mathbf{z}_0|^2}{8a^2} \right], \quad (4.45)$$

where R_0 is the radial distance of the stimulus from the origin.

4.3 Simulation Experiments

In the simulation experiments, the number of neurons is $N = N_x \times N_y$, and the range of (x_1, x_2) is $-\pi \leq x_1, x_2 < \pi$. The boundary condition is periodic.

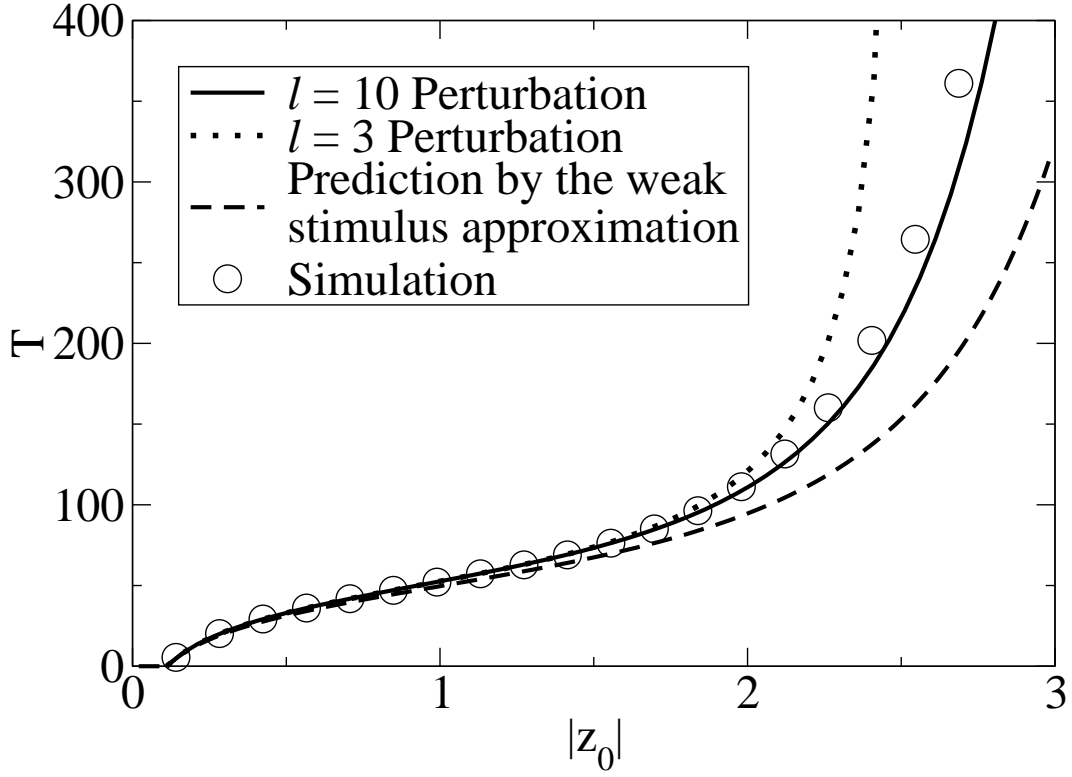


Figure 4.9: The reaction time T for the synaptic input to catch up the stimulus position change from 0 to z_{01} . Parameters: $N = N_x \times N_y = 40 \times 40$, $\Theta = \pi\sqrt{2/N}$, $\alpha = 0.05$ and the rest are the same as figure 4.1. Near $|z_0| = 0$, the reaction time is zero up to Θ , because the reaction time is defined as the time needed for the bump to track from 0 to $|z_0|$ within the range of Θ .

4.3.1 Reaction Time to an Abrupt Change of the Stimulus

In this experiment, the stimulus is centered at $(0,0)$ until the synaptic input $U(\mathbf{x}, t)$ becomes steady. At $t = 0$, the stimulus abruptly changes from $(0,0)$ to $\mathbf{z}_0 \equiv (z_{01}, 0)$, and we observe the dependence of the reaction time on the distance z_{01} . Then, the bump will track the stimulus, as shown in figure 4.2. The reaction time is defined by the time needed to have $|\mathbf{z}(t) - \mathbf{z}_0| < \Theta$, where Θ is the threshold. This threshold is necessary in this experiment, because the motion of $\mathbf{z}(t)$ will become very slow when it approaches the stimulus, as implied by Eq. (4.22). Also, the assumption is reasonable because in real biological systems, we do not need to have $\mathbf{z}(t) = \mathbf{z}_0(t)$ to make decisions.

As shown in figure 4.9, the prediction given by Eq. (4.22) works well only when the change in the position of the stimulus is small, while the $l = 3$ perturbation works well up to $|z_0| = 2$. The prediction of the $l = 10$ perturbation is the best among the three. From this result, one can state that, when the position change of the stimulus is small, only $\psi_{l,j}$ with small l will be activated. However, when the change in stimulus position

is larger, higher order distortions are activated. This is reasonable, because, for smaller l , the distortions are concentrated around $\mathbf{z}(t)$, but if the stimulus is far away from $\mathbf{z}(t)$, the tail part of the bump will be distorted first, leading to higher order distortions.

4.3.2 Amplitudes of the Basis Function Distortion Modes

From Eqs. (4.12) and (4.24), $b_{l,j}$ can be predicted by the projections of δU onto the basis functions $\psi_{l,j}$. The experimental settings are the same as above, but \mathbf{z}_0 was fixed to be $\mathbf{z}_0 = (2, 0)$ in polar coordinates.

As shown in figure 4.10, the predicted $b_{l,j}$'s agree with the simulation results well. It confirms that the perturbative method can also predict the motion of the synaptic input in detail. $b_{0,0}$ indicates that the height drops from its initial value after the stimulus is shifted. The $\psi_{0,0}$ component of the distortion is reduced by the inhibition. It approaches 0 roughly, as if there were no external stimulus, and there is even a slight overshoot. Afterwards, the distortion relaxes smoothly to the equilibrium value when it approaches the shifted position of the stimulus. Similarly, the amplitude of the $\psi_{1,\pm 1}$ components falls abruptly to a negative value initially. This is due to the tail of the bump being pulled by the newly positioned stimulus, causing the peak to lag behind the center of mass. Afterwards, it relaxes smoothly to 0. The initial change in $b_{2,0}$ indicates an increase in width along the direction of the stimulus, and that of $b_{2,\pm 2}$ signals a cigar-shaped distortion when the bump is being pulled by the stimulus. The amplitude $b_{3,\pm 1}$ describes the skewness of the bump, and $b_{3,\pm 3}$ describes the bump being distorted when its tip is pulled by the stimulus, with the posterior part lagging in motion, causing a triangular-shaped distortion.

4.4 Summary

In this chapter, a perturbative method to deal with continuous attractor neural networks is presented in two-dimensional space. We have introduced a simple solvable model to demonstrate how to use the perturbative method to analyze the dynamics of distortions and synaptic input. Since the coupling factors are defined to be translational invariant, a family of stationary states can be sustained anywhere in the preferred stimulus space. Furthermore, the synaptic input is able to track the stimulus in the space. By studying the dynamics, one can deduce the tracking time and the distortions of the synaptic input.

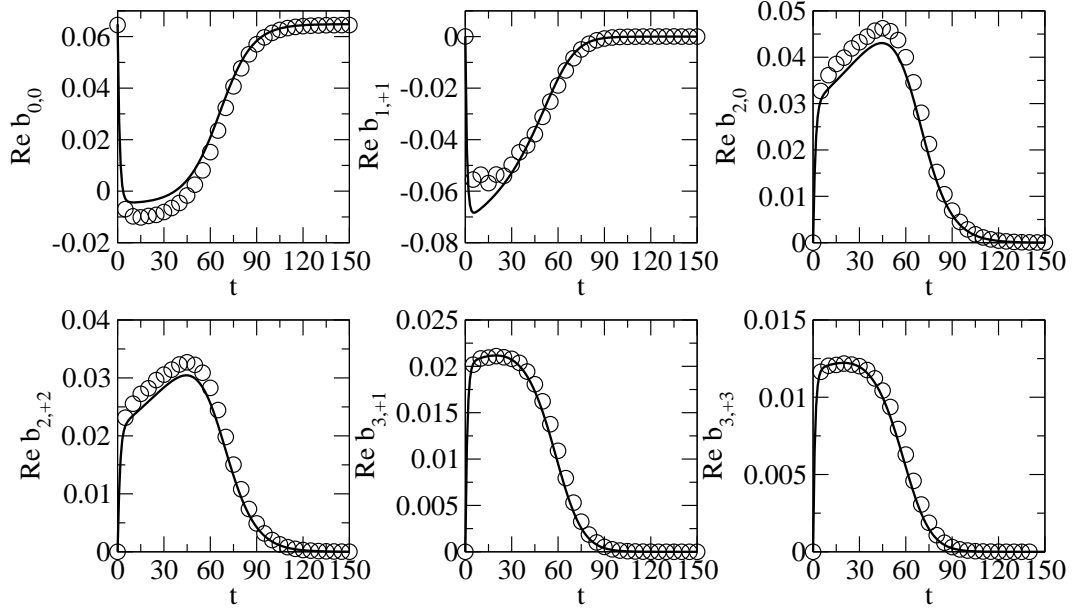


Figure 4.10: The experimentally projected $b_{l,j}$ and the predicted $b_{l,j}$ using $l = 10$ perturbation. Solid lines: corresponding predictions. Circles: simulation results. Parameters: same as figure 4.9.

For one-dimensional continuous attractor neural networks, the tracking speed can be roughly approximated by [28, 26]

$$\frac{dz}{dt} = \frac{\alpha}{\tau}(z_0 - z) \exp \left[-\frac{|z_0 - z|^2}{8a^2} \right], \quad (4.46)$$

which is similar to Eq. (4.22). Although they are rough approximations, the basic properties of tracking in one and two dimensions are similar. The key predictions in the one-dimensional case, the maximum trackable speed and the lag behind a continuously moving stimulus, are also applicable in two dimensions. These similarities arise from the rotational invariance of the interaction kernel and the bump in the limit of weak stimulus, since the description of the dynamics by the translational mode is sufficient. Note, however, for the stronger stimuli, the dynamics is richer in the two-dimensional case, since distortion modes unique to the two-dimensional case need to be considered; examples of cigar-shaped and triangular-shaped distortions are shown in figure 4.10.

For this particular model, the eigenfunctions of the interaction matrix in polar coordinates are also studied. By Eq. (4.24), the interaction matrix \mathcal{G} can be obtained. However, due to complications in the calculation, we can only calculate it term by term.

Since the matrix is upper triangular, the eigenvalues are the diagonal entries, $\lambda_{n,m}$. As the eigenvalues are at most 1, one can show that the synaptic input has a stable Gaussian form. The eigenfunctions corresponding to eigenvalue 1 represent the positional shift. As studied above, different modes of distortion correspond to different kinds of distortion. For example, the component of $\psi_{0,0}$ corresponds to the change in height, while $\psi_{2,0}$ represents the change in width.

Concerning the robustness of the method, we remark that it can be applied to other types of networks with tracking behavior. A common example is the continuous attractor neural network with the Mexican hat interaction. Using the basis functions of the two-dimensional quantum harmonic oscillator, we can obtain the matrix elements of the interaction kernel numerically, although elegant expressions such as those obtained here may not be available. Perturbation dynamics can then be worked out analogously. This proposed extension can be able to address a recent issue of interest, namely, the instability of bumps and rings in a two-dimensional neural field of Amari type [11]. Meanwhile, we note in passing that the present model with a quadratic response and a global inhibition does not suffer from the stability problem.

Chapter 5

1D Continuous Attractor Neural Networks with Time-dependent Couplings¹

5.1 Introduction

As mentioned in chapter 1, the time-independent neuronal couplings are not reasonable in the true neural systems. Experimental data has consistently revealed that neuronal connection weights change in short time scales, varying from hundreds to thousands of milliseconds (see, e.g., [30]). This is called short-term plasticity (STP), and have two different forms, namely, short-term depression (STD) and short-term facilitation (STF). The mechanism underlying STD is the depletion of available resources in transmitting action potentials from a pre-synaptic neuron to the post-synaptic one. On the other hand, STF is associated with the increased level of residual calcium due to spike generation, and the high calcium level increases the release probability of neurotransmitters. In this study, for simplicity, we only consider the 1D cases of the networks.

5.2 Synaptic Depression

To model the depletion of the neural resource for signal transmission, we modify Eq. (2.1) to

$$\tau_s \frac{\partial U(x, t)}{\partial t} = I^{\text{ext}}(x, t) + \rho \int dx' J(x, x') p(x', t) r(x') - U(x, t), \quad (5.1)$$

¹A substantial part of this chapter was included in a recent submission under review.

where $J(x, x')$ is given by Eq. (2.2), $r(x) = U(x)^2 / (1 + k\rho \int dx' U(x')^2)$ is the firing rate of the neuron at x and $p(x, t)$ represents the effect of depletion of neural resource. The dynamics of $p(x, t)$ is then given by [15, 31]

$$\tau_d \frac{\partial p(x, t)}{\partial t} = 1 - p(x, t) - \tau_d \beta p(x, t) r(x), \quad (5.2)$$

where τ_d is the time scale of the synaptic depression, which is chosen to be $\tau_d = 50\tau_s$, and β controls the strength of the synaptic depression. In the steady state,

$$p(x) = \frac{1}{1 + \tau_d \beta r(x)}. \quad (5.3)$$

It implies that, when the system is in a silent state, i.e. $r(x) = 0$, $p(x) = 1$. It means that, when the firing rate is 0, the effective connection between neurons at x and x' in Eq. (5.1) will be given by the original coupling function, i.e. $J(x, x')$. However, when the firing rate is non-zero, the function $p(x)$ will be less than 1. It shows how the signal transmissions weaken the connection strength of the active synapse. By examining the steady state solution of Eqs. (5.1) and (5.2), we find that U_0 , Eq. (5.4), scales as ρJ_0 and $1 - p(x, t)$ scales as $\tau_d \beta U_0^2$. So, we introduce the dimensional parameters $\bar{k} \equiv k/k_c$, same k_c as in chapter 2, and $\bar{\beta} \equiv \tau_d \beta / (\rho^2 J_0^2)$.

5.2.1 Phase Diagram

With this kind of time dependence with $J(x, x')$, the CANNs may exhibit various interesting behaviors. York et al. [32] studied a different CANN model and found that it will relax to various classes of solutions. They are spontaneously moving bump solution, static bump solution, homogeneous solution, i.e. $U(x) = \text{constant}$, and silent solution. In our model, up to this moment, we have discovered similar behaviors except for homogeneous solutions, given that the stimulus is absent. As shown in figure 5.1, there are four regions. If \bar{k} and $\bar{\beta}$ are both large, the system will only be stable in silent state. This is because whenever there is a neuronal input bump over the preferred stimulus space, the excitatory connection will be weakened and inhibition signal will be too large. The bump cannot be sustainable, as expected. In the *moving* region, the neuronal input bump will move spontaneously with a constant speed. As shown in figure 5.2, the motion of the bump is due to the fact that the bump of neuronal input is not centered at the center of $p(x, t)$. This asymmetric synaptic depressional effect will make the excitational current on one side on the bump stronger than that of the other side. As a result, the bump will start to move to left or right. In the static phase, the system will only relax

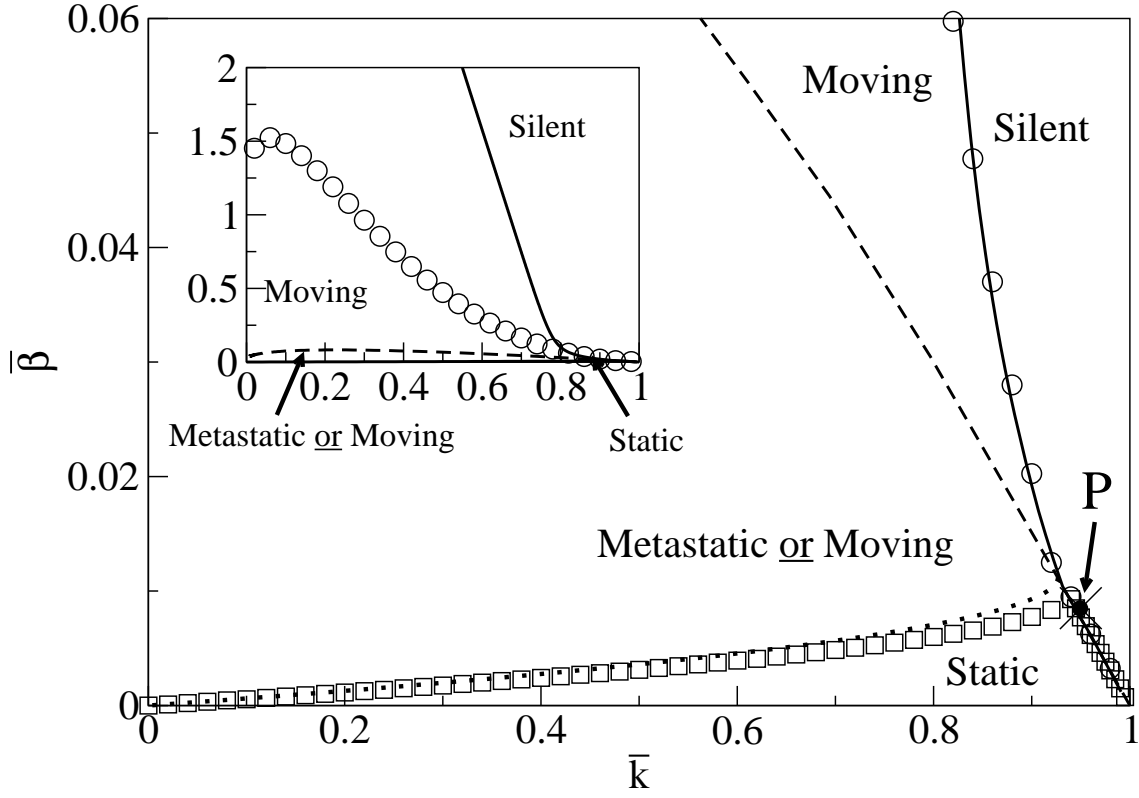


Figure 5.1: Phase diagram of the network states. Symbols: numerical solutions. Dashed line: predicted boundary for amplitude-stable static (metastatic) bump. Dotted line: predicted boundary for static bump. Solid line: predicted boundary between silent state and all possible stable bumps. Order of perturbation = 11th. Point P: the working point for Figs. 5.3 and 5.11. Parameters: $\tau_d/\tau_s = 50$, $a = 0.5/6$, range of the network = $[-\pi, \pi)$.

to stable static bump solution.

In figure 5.1, there is a region called ‘*Metastatic or Moving*’. In this region, the system will relax to stable spontaneously moving bumps. However, the static bumps will be stable in amplitude, but unstable in position. So, if the initial conditions of $U(x, t)$ and $p(x, t)$ are carefully selected, the bump will be static and metastable, due to the symmetry. However, if any small asymmetric perturbation is added to the system, the system will relax to a steady moving bump solution. The boundaries of figure 5.1 will be studied in the following analysis section.

5.2.2 Plateau States

If one can select the parameters $(\bar{k}, \bar{\beta})$ appropriately within the *marginally unstable* region, e.g. point P as in figure 5.1, the plateau behavior can be observed in the system.

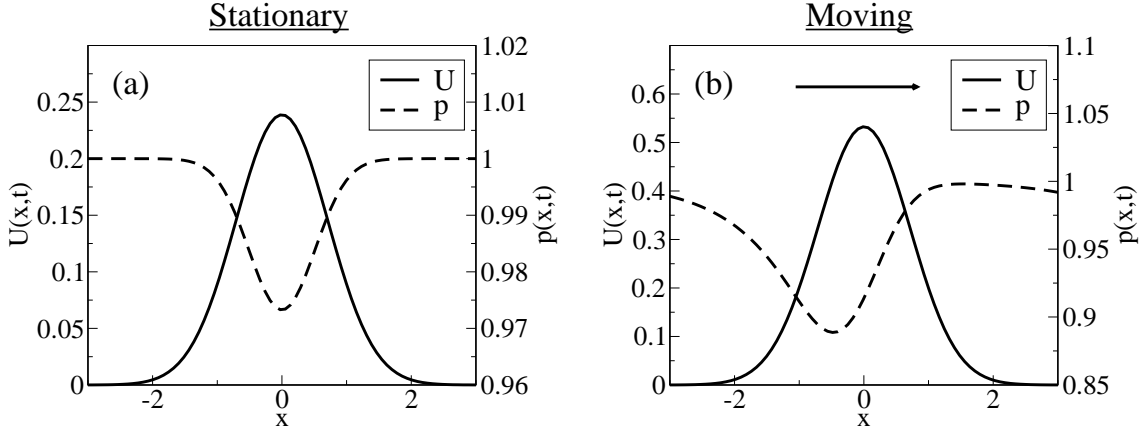


Figure 5.2: Neuronal input $u(x, t)$ and the STD coefficient $p(x, t)$ in (a) the static state at $(\bar{k}, \bar{\beta}) = (0.9, 0.005)$, and (b) the moving state at $(\bar{k}, \bar{\beta}) = (0.5, 0.015)$. Parameter: $\tau_d/\tau_s = 50$.

In figure 5.3, with different initial conditions, the neuronal input bump will decay to a stable silent state, given that the stimulus is absent. However, the bump will not decay exponentially to zero. The bump will first decay to a intermediate plateau state. After a period, the bump will decay out exponentially. This feature is important, because, in the real systems, the activity of the neuron should decay to silence after the stimulus is removed. Indeed, how to shut off the activity of a CANN has been a challenging issue that received wide attention in theoretical neuroscience, with solutions suggesting that a strong external input either in the form of inhibition or excitation must be applied (see, e.g., [33]). In our model, this slow-decaying behavior provides a mechanism for closing down network activities naturally and in the desirable duration.

However, in figure 5.4, we found that the plateau behavior can also be observed, with some particular stimuli, within the region that the static bumps exist. It will be explained in the analysis subsection. Also, when the parameters $(\bar{k}, \bar{\beta})$ is close to the region that a stable bump can be built by the stimuli, the duration of the plateau state will be very long.

5.2.3 Tracking Performance

Similar to systems without synaptic depressional effects, the neuronal input bump can track the change of position of the stimulus. In figures 5.5 and 5.6, the bump-shaped neuronal input tracks from $x = 0$ to $x = 1.5$. At $t = 0$, the stimulus position is changed from 0 to 1.5. Before this change of stimulus, the stimulus was at zero until the neuronal input bump became steady. With appropriately selected parameters, shown in figure

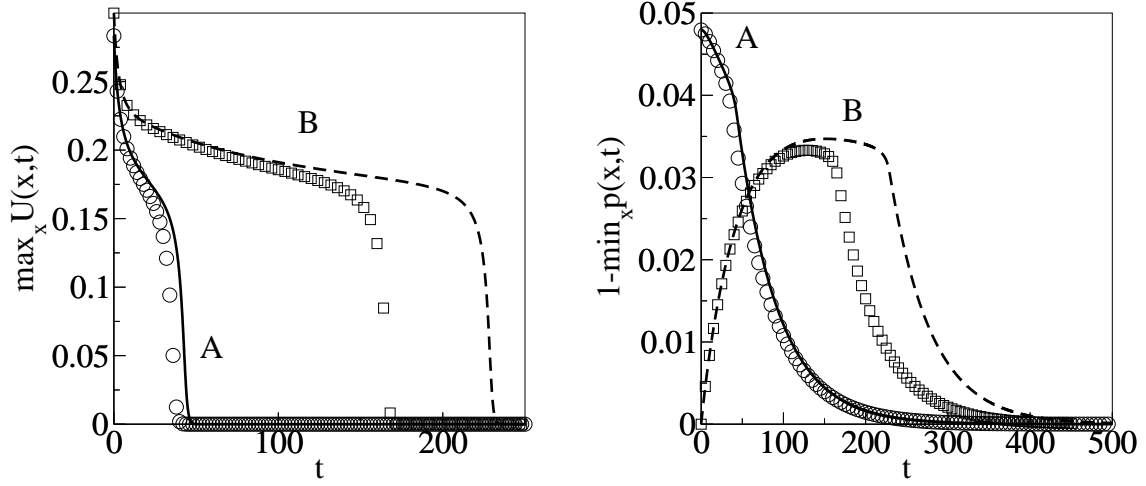


Figure 5.3: Magnitudes of neuronal input $U(x, t)$ and synaptic depression $1 - p(x, t)$ at $(\bar{k}, \bar{\beta}) = (0.95, 0.0085)$ (point P in figure 5.1) and for initial conditions of types A and B in figure 5.11. Symbols: numerical solutions. Lines: Gaussian approximation using Eqs. (5.10) and (5.11). Other parameters: $\tau_d/\tau_s = 50$, $a = 0.5$ and $x \in [-\pi, \pi)$.

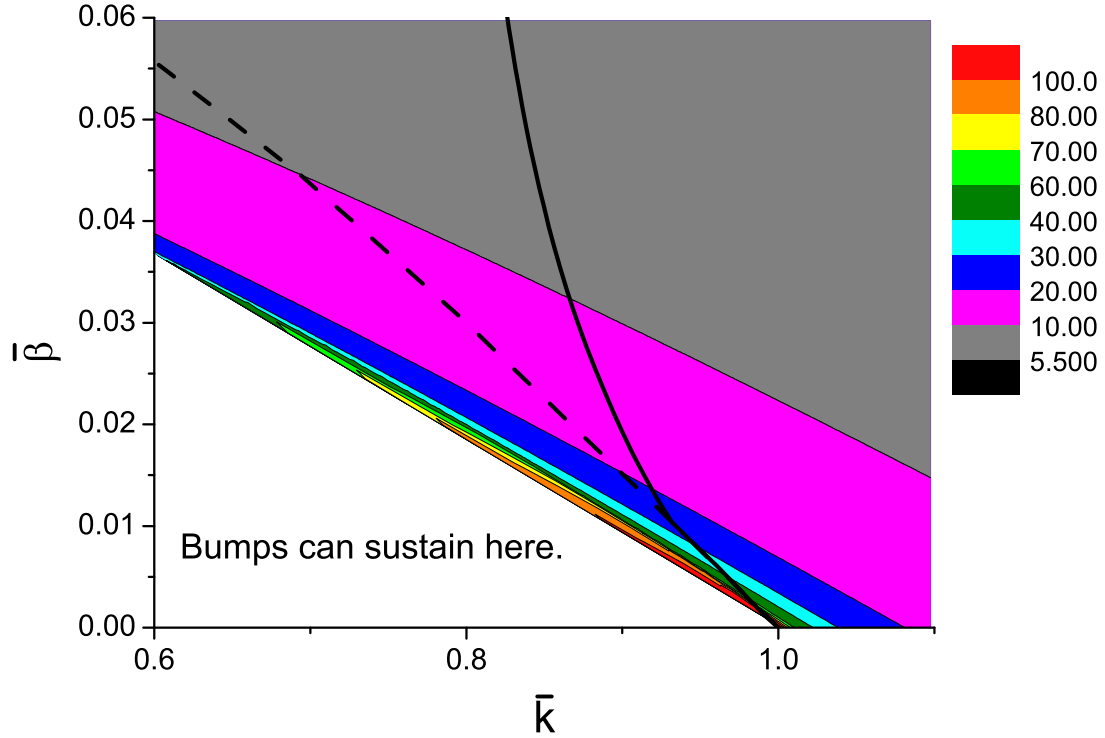


Figure 5.4: Contours of plateau lifetimes in the space of k and β . The lines are the two topmost phase boundaries in figure 5.1. The initial condition is prepared by using stimulus with $\alpha = 0.5$.

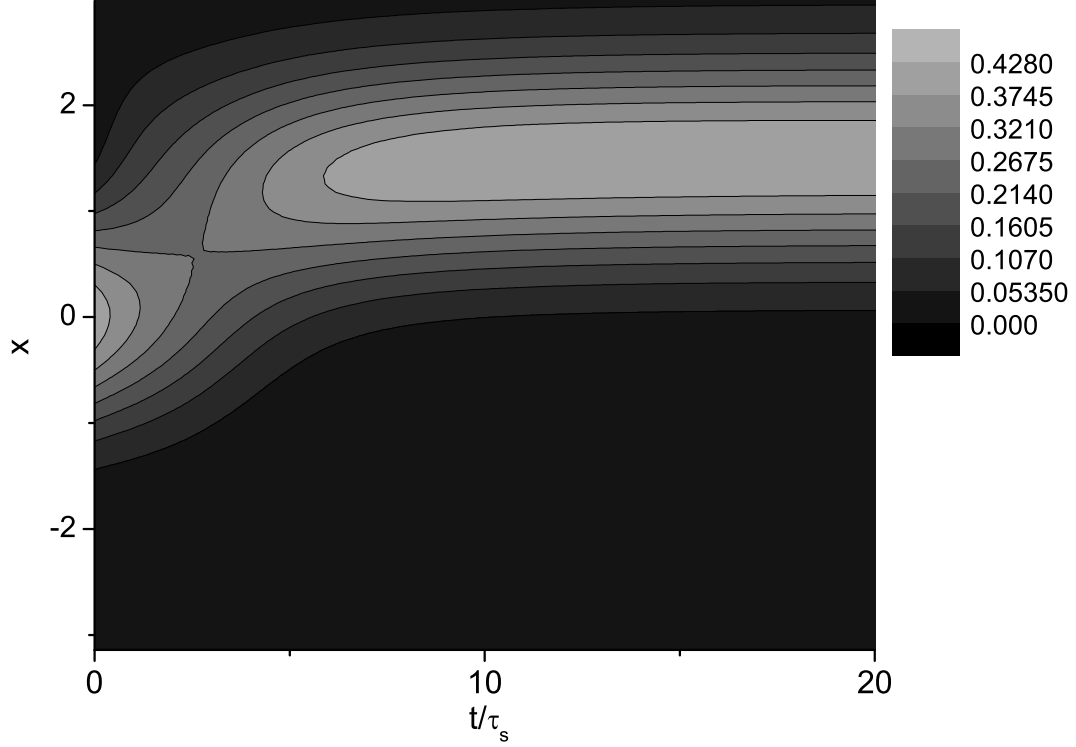


Figure 5.5: The neural response profile tracks the change of position of the external stimulus from $z_0 = 0$ to 1.5 at $t = 0$. Parameters: $\tau_d/\tau_s = 50$, $a = 0.5$, $\bar{k} = 0.95$, $\bar{\beta} = 0.0085$, $\alpha = 0.5$.

5.7, systems with synaptic depression can improve the tracking performance, especially the reaction time. This improvement in reaction can be seen in the analysis as well. Also, comparing with systems with synaptic facilitation, the latter has a negative effect, as we will show in the later sections.

5.3 Analysis

Based on some simulation results, e.g. figure 5.2, with the presence of synaptic depression, the shape of neuronal input can maintain *almost* a Gaussian profile, as if there were no synaptic depression, provided that the synaptic depression is small. With this observation, we *assume*

$$U(x, t) = U_0(t) \exp \left[-\frac{(x - z)^2}{4a^2} \right], \quad (5.4)$$

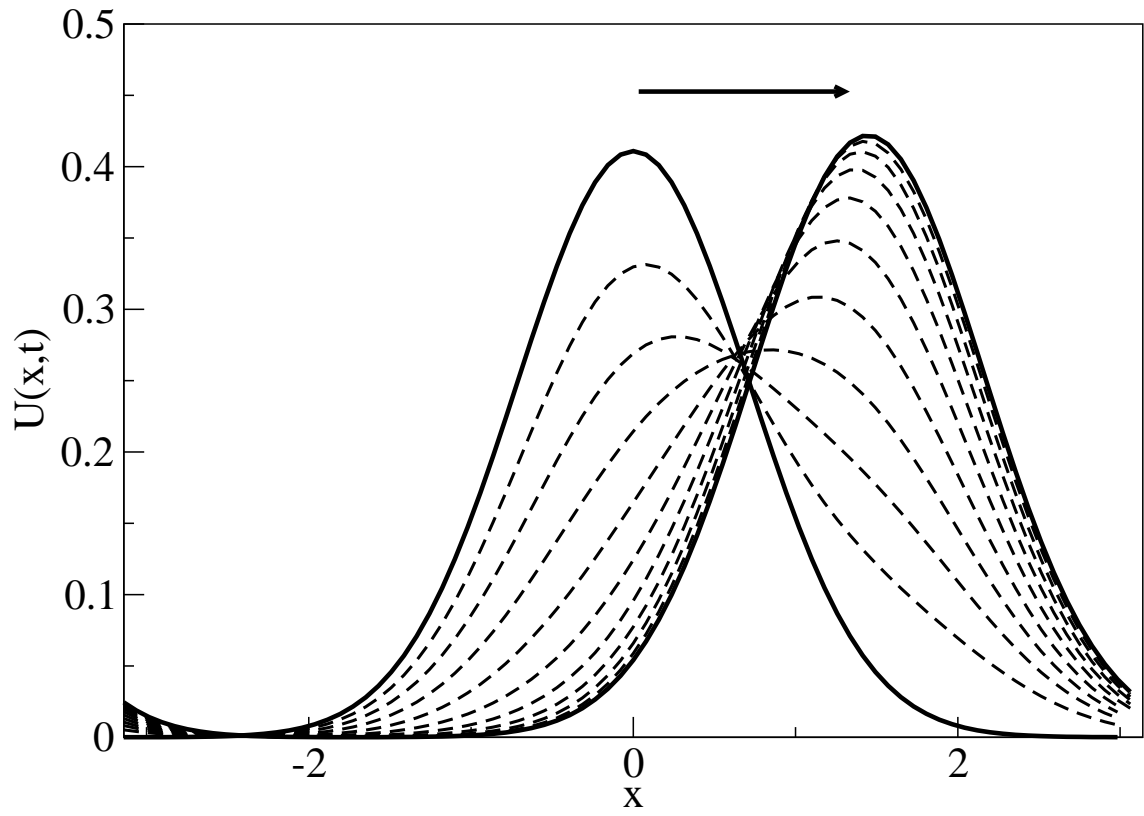


Figure 5.6: The profile of $u(x, t)$ at $t/\tau_s = 0, 1, 2, \dots, 10$ during the tracking process in figure 5.5.

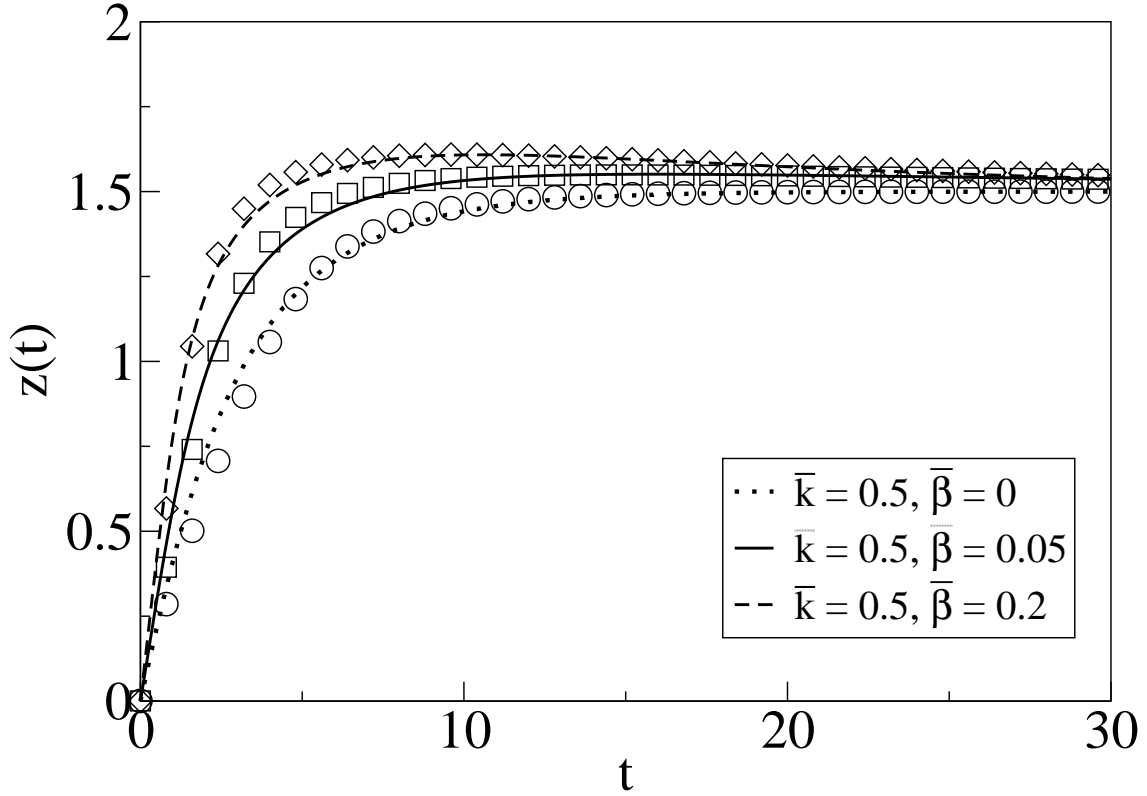


Figure 5.7: The response of CANNs with STD to an abruptly changed stimulus from $z_0 = 0$ to $z_0 = 1.5$ at $t = 0$. Symbols: numerical solutions. Lines: Gaussian approximation using 11th order perturbation of the STD coefficient. Parameters: $\tau_d/\tau_s = 50$, $\alpha = 0.5$, $a = 0.5$ and $x \in [-\pi, \pi)$.

while the function $p(x, t)$ is decomposed as

$$p(x, t) = 1 - \sum_{n=0}^{\infty} p_n(t) v_n(x|z), \quad (5.5)$$

where v_n is the n^{th} eigenfunction of quantum harmonic oscillator [27]

$$v_n(x|z) = \frac{1}{\sqrt{\sqrt{\pi}a2^n n!}} H_n \left(\frac{x-z}{a} \right) \exp \left[-\frac{(x-z)^2}{2a^2} \right], \quad (5.6)$$

and H_n is the n^{th} Hermite Polynomial. Note that, this selection of basis functions are different from that in Eq. (2.8), which are given by

$$u_n(x) = \frac{1}{\sqrt{\sqrt{2\pi}a2^n n!}} H_n \left(\frac{x}{\sqrt{2}a} \right) \exp \left[-\frac{x^2}{4a^2} \right]. \quad (5.7)$$

5.3.1 Static Bump Solution

Without lose of generality, we choose $z = 0$. For the lowest order approximation, we set $p(x, t) = 1 - p_0(t)v_0(x|0)$. Substituting this and Eq.(5.4) into Eqs.(5.1) and (5.2), we get

$$\begin{aligned} \tau_s \frac{dU_0(t)}{dt} e^{-\frac{x^2}{4a^2}} &= -U_0(t) e^{-\frac{x^2}{4a^2}} + \frac{\rho J_0}{\sqrt{2}} \frac{U_0(t)^2}{1 + k\rho\sqrt{2\pi}aU_0(t)^2} e^{-\frac{x^2}{4a^2}} \\ &\quad - p_0(t) \frac{\rho J_0}{\sqrt{3\sqrt{\pi}a}} \frac{U_0(t)^2}{1 + k\rho\sqrt{2\pi}aU_0(t)^2} e^{-\frac{x^2}{3a^2}}, \end{aligned} \quad (5.8)$$

and

$$\begin{aligned} -\tau_d \frac{dp_0(t)}{dt} e^{-\frac{x^2}{2a^2}} &= p_0(t) e^{-\frac{x^2}{2a^2}} - \sqrt{\sqrt{\pi}a}\tau_d\beta \frac{U_0(t)^2}{1 + k\rho\sqrt{2\pi}aU_0(t)^2} e^{-\frac{x^2}{2a^2}} \\ &\quad + \tau_d\beta p_0(t) \frac{U_0(t)^2}{1 + k\rho\sqrt{2\pi}aU_0(t)^2} e^{-\frac{x^2}{a^2}}. \end{aligned} \quad (5.9)$$

By projecting both sides of Eq.(5.8) on u_0 , Eq. (2.8), and both sides of Eq.(5.9) on v_0 , we obtain

$$\tau_s \frac{dU_0(t)}{dt} \approx -U_0(t) + \frac{\rho J_0}{\sqrt{2}} \frac{U_0(t)^2}{1 + k\rho\sqrt{2\pi}aU_0(t)^2} \left[1 - \sqrt{\frac{4}{7}} \frac{p_0(t)}{\sqrt{\sqrt{\pi}a}} \right], \quad (5.10)$$

and

$$\tau_d \frac{d}{dt} \left(\frac{p_0(t)}{\sqrt{\sqrt{\pi}a}} \right) \approx -\frac{p_0(t)}{\sqrt{\sqrt{\pi}a}} + \tau_d\beta \frac{U_0(t)^2}{1 + k\rho\sqrt{2\pi}aU_0(t)^2} \left[1 - \sqrt{\frac{2}{3}} \frac{p_0(t)}{\sqrt{\sqrt{\pi}a}} \right]. \quad (5.11)$$

As shown in figure 5.3, these two equations can roughly predict the trends of the magnitudes of $U(x, t)$ and $1 - p(x, t)$. However, the difference between simulation and prediction is due to the fact that the above prediction is done by projection, but not exact calculation. The stationary solution should satisfy

$$U_0 \approx \frac{\rho J_0}{\sqrt{2}} \frac{U_0^2}{1 + k\rho\sqrt{2\pi a}U_0^2} \left[1 - \sqrt{\frac{4}{7}} \frac{p_0}{\sqrt{\sqrt{\pi a}}} \right], \quad (5.12)$$

and

$$\frac{p_0(t)}{\sqrt{\sqrt{\pi a}}} \approx \tau_d \beta \frac{U_0(t)^2}{1 + k\rho\sqrt{2\pi a}U_0(t)^2} \left[1 - \sqrt{\frac{2}{3}} \frac{p_0(t)}{\sqrt{\sqrt{\pi a}}} \right]. \quad (5.13)$$

Dividing Eq. (5.12) and Eq. (5.13), we have

$$\bar{U} = \frac{1 - \sqrt{\frac{4}{7}} \frac{p_0}{\sqrt{\sqrt{\pi a}}}}{\sqrt{2} \bar{\beta} (1 - \sqrt{\frac{2}{3}} \frac{p_0}{\sqrt{\sqrt{\pi a}}})} \frac{p_0}{\sqrt{\sqrt{\pi a}}}, \quad (5.14)$$

where $\bar{U} = \rho J_0 U_0$. By substituting Eq. (5.14) into Eq. (5.13), we have

$$\frac{1}{2\bar{\beta}} \left(1 - \sqrt{\frac{4}{7}} \frac{p_0}{\sqrt{\sqrt{\pi a}}} \right)^2 \left[1 - \left(\sqrt{\frac{2}{3}} + \frac{\bar{k}}{8\bar{\beta}} \right) \frac{p_0}{\sqrt{\sqrt{\pi a}}} \right] \frac{p_0}{\sqrt{\sqrt{\pi a}}} - \left(1 - \sqrt{\frac{2}{3}} \frac{p_0}{\sqrt{\sqrt{\pi a}}} \right)^2 = 0. \quad (5.15)$$

For any given p_0 , the rescaled inhibition \bar{k} can be rewritten as

$$\bar{k} = \frac{8}{p_0} \left(\sqrt{\sqrt{\pi a}} - \sqrt{\frac{2}{3}} p_0 \right) \bar{\beta} - \frac{16(\sqrt{\pi a})}{p_0^2} \left(\frac{\sqrt{\sqrt{\pi a}} - \sqrt{2/3} p_0}{\sqrt{\sqrt{\pi a}} - \sqrt{4/7} p_0} \right)^2 \bar{\beta}^2. \quad (5.16)$$

With this equation, for any $p_0/\sqrt{\sqrt{\pi a}} < 1$, we can draw the parabola on the space of \bar{k} and $\bar{\beta}$, as shown in figure 5.8. Each parabola corresponds to a given value of p_0 .

Having the existence condition, it is natural to discuss about the stability condition of the equation system, Eqs. (5.10) and (5.11). Let us consider the dynamical equations,

$$\tau_s \frac{d\bar{U}}{dt} = \frac{1}{\sqrt{2}} \frac{\bar{U}^2}{1 + \bar{k} \bar{U}^2/8} \left(1 - \sqrt{\frac{4}{7}} \frac{p_0}{\sqrt{\sqrt{\pi a}}} \right) - \bar{U}, \quad (5.17)$$

$$\tau_d \frac{dp_0}{dt} = \frac{\bar{\beta} \bar{U}^2}{1 + \bar{k} \bar{U}^2/8} \left(\sqrt{\sqrt{\pi a}} - \sqrt{\frac{2}{3}} p_0 \right) - p_0. \quad (5.18)$$

Suppose (\bar{U}^*, p_0^*) is the fixed point solution. Let $\epsilon = \bar{U} - \bar{U}^*$ and $\delta = p_0 - p_0^*$. After

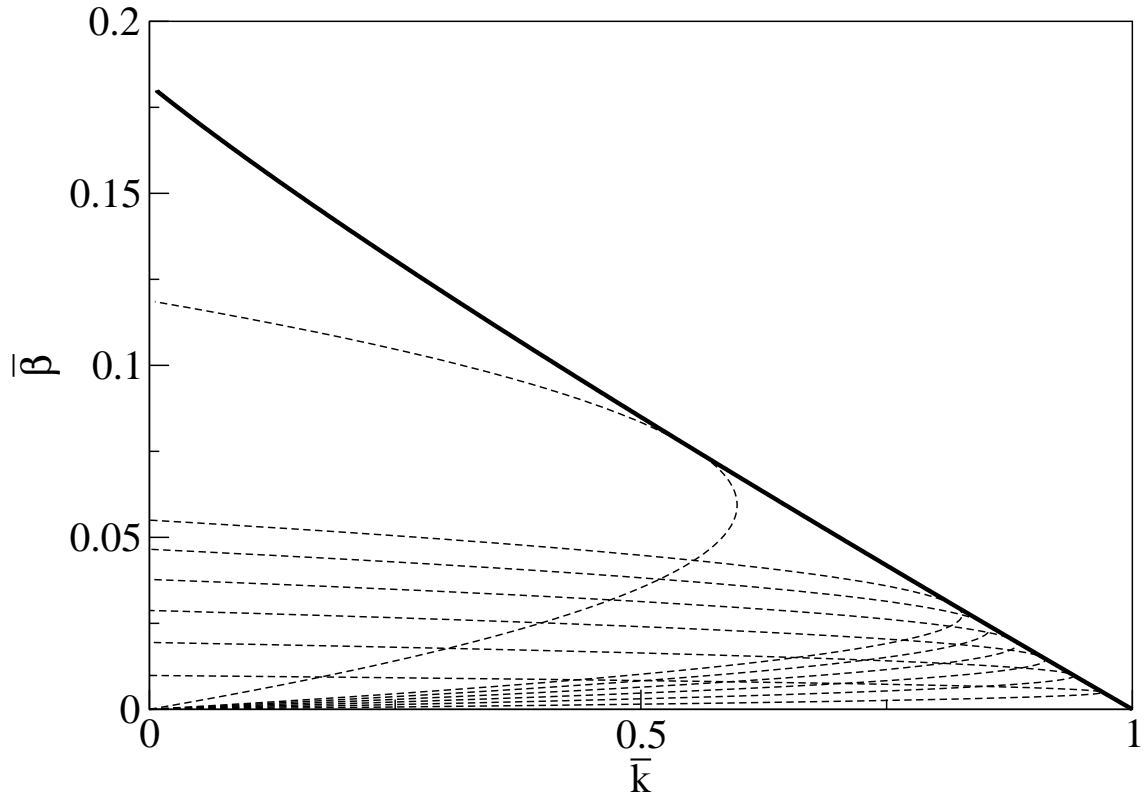


Figure 5.8: Region of existence of the static bump solution. Dashed line: Parabolas drawn by Eq. (5.16). Solid line: existence region figured out by the parabolas. Parameter: $z = 0.5$.

linearization, we have

$$\frac{d}{dt} \begin{pmatrix} \epsilon \\ \delta \end{pmatrix} = \begin{pmatrix} M_{11} & M_{12} \\ M_{21} & M_{22} \end{pmatrix} \begin{pmatrix} \epsilon \\ \delta \end{pmatrix}, \quad (5.19)$$

where

$$M_{11} = -\frac{1}{\tau_s} \left[1 - \frac{\sqrt{2} \bar{U}}{(1 + \bar{k} \bar{U}^2/8)^2} \left(1 - \sqrt{\frac{4}{7}} \frac{p_0}{\sqrt{\sqrt{\pi} a}} \right) \right] \quad (5.20)$$

$$M_{12} = -\frac{\bar{U}^2}{\tau_s \sqrt{\sqrt{\pi}} (1 + \bar{k} \bar{U}^2/8)} \sqrt{\frac{2}{7}} \quad (5.21)$$

$$M_{21} = \frac{2\bar{\beta} \bar{U}}{\tau_d (1 + \bar{k} \bar{U}^2/8)^2} \left(\sqrt{\sqrt{\pi} a} - \sqrt{\frac{2}{3}} p_0 \right) \quad (5.22)$$

$$M_{22} = -\frac{1}{\tau_d} \left(1 + \frac{\bar{\beta} \bar{U}^2}{1 + \bar{k} \bar{U}^2/8} \sqrt{\frac{2}{3}} \right). \quad (5.23)$$

The stability condition of the fixed point solution is that, the two eigenvalues of the above matrix are negative in its real part. The result can be obtained numerically, as shown in figure 5.9.

Analytically, from the matrix, the stable boundary can be derived to be

$$\bar{\beta} = \frac{\frac{p_0}{\sqrt{\sqrt{\pi} a}} \left(1 - \sqrt{\frac{4}{7}} \frac{p_0}{\sqrt{\sqrt{\pi} a}} \right)^2}{4 \left(1 - \sqrt{\frac{2}{3}} \frac{p_0}{\sqrt{\sqrt{\pi} a}} \right)} \left[1 + \frac{\tau_s}{\tau_d \left(1 - \sqrt{\frac{2}{3}} \frac{p_0}{\sqrt{\sqrt{\pi} a}} \right)} \right], \quad (5.24)$$

for a given p_0 . Accompanying with Eq. (5.16), the phase boundary can be done. As we shall see, this stability condition can only apply for the stability in amplitude. For the asymmetric perturbations, the neuronal bump may not be stable.

5.3.2 Perturbative Approach to Synaptic Depression

A moving bump solution means the peak of $U(x, t)$ changes with time. Consider the bump moves in a constant speed v , i.e., $z(t) = vt$. Substituting $U(x|z(t), t)$ in Eq. (5.1), we have, for the left-hand side of the equation,

$$\tau_s \frac{\partial U(x, t)}{\partial t} = \tau_s \dot{U}_0 e^{-\frac{|x-z|^2}{4a^2}} + \tau_s \frac{U_0 \dot{z}}{2a} e^{-\frac{|x-z|^2}{4a^2}} \left(\frac{x-z}{a} \right), \quad (5.25)$$

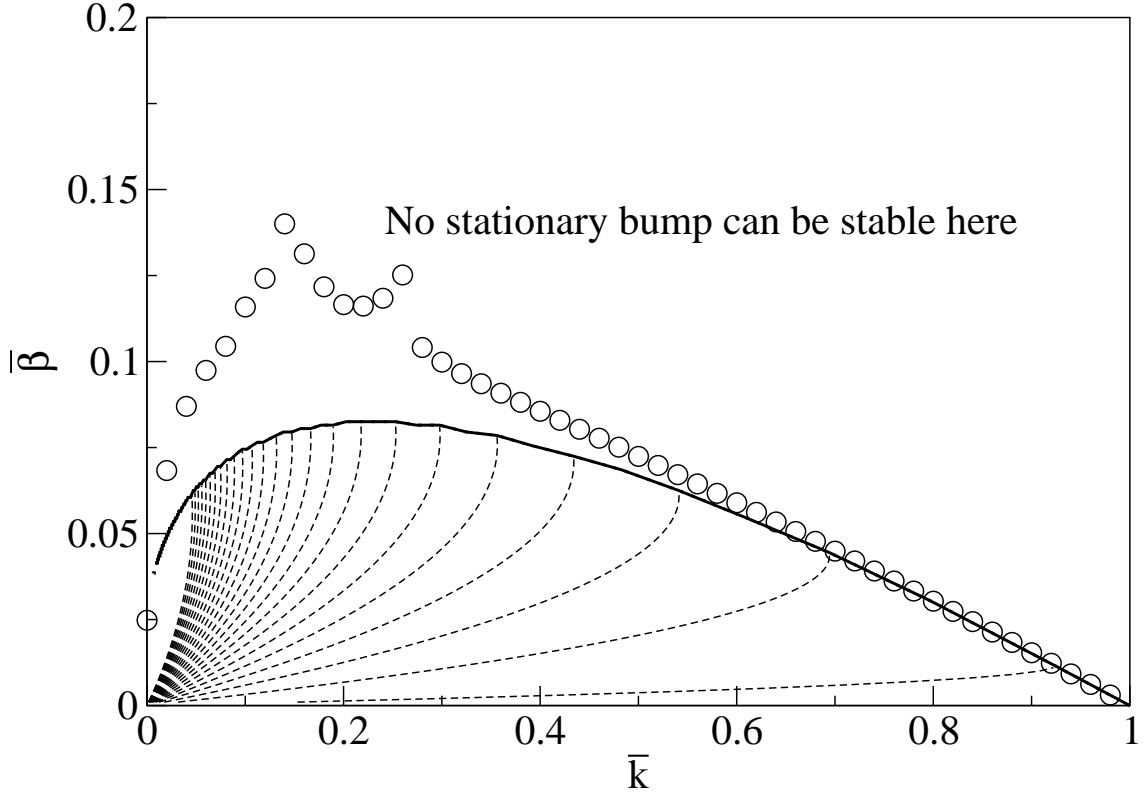


Figure 5.9: Region of amplitude stable static bump solution. Dashed line: Parabolas drawn by Eq. (5.16). Solid line: the region figured out by Eq. 5.19. Symbols: simulations. The simulations for $(\bar{k}, \bar{\beta})$ are done by initial conditions prepared with $(\bar{k}, 0)$ and stimulus with $\alpha = 0.5$. However, these simulations may not be appropriate to test this phase boundary. As we will show later, below this phase boundary, the bump may not be *totally* stable. Some of the states are only amplitude-stable, but not positionally unstable.

and for the right-hand side of the equation,

$$\begin{aligned}
& -U(x, t) + \rho \int \frac{dx' J(x, x') p(x') U(x', t)^2}{1 + k\rho \int dx'' U(x'', t)^2} \\
&= \frac{\rho J_0 U_0^2}{B \sqrt{2\pi a^2}} \int dx' e^{-\frac{(x-x')^2}{2a^2}} \left[1 - \sum_{n=0}^{\infty} \frac{p_n}{\sqrt{\sqrt{\pi} a n! 2^2}} e^{-\frac{(x'-z)^2}{2a^2}} \left(a \frac{d}{dz'} \right)^n \Big|_{z'=z} e^{-\frac{(x'-z')^2}{a^2}} \right] e^{-\frac{(x'-z)^2}{2a^2}} \\
& - U_0 e^{-\frac{(x-z)^2}{2a^2}} \\
&\approx \left[\frac{\rho J_0 U_0^2}{B \sqrt{2}} - \frac{\rho J_0 U_0^2}{B} \sqrt{\frac{2}{7}} \sum_{n \text{ even}} \frac{p_n}{\sqrt{\sqrt{\pi} a n! 14^n}} \frac{n! (-1)^{n/2}}{(n/2)!} - U_0 \right] e^{-\frac{(x-z)^2}{4a^2}} \\
& + \left[\frac{\rho J_0 U_0^2}{B} \frac{2\sqrt{2}}{7} \sum_{n \text{ odd}} \frac{p_n}{\sqrt{\sqrt{\pi} a n! 14^n}} \frac{(n+1)! (-1)^{(n+1)/2}}{[(n+1)/2]!} \right] e^{-\frac{(x-z)^2}{4a^2}} \frac{x-z}{a}, \tag{5.26}
\end{aligned}$$

where $B = 1 + k\rho \int dx' U(x', t)^2 = 1 + k\rho \sqrt{2\pi} a U_0^2$. By comparing terms, we have

$$1 = \left[\frac{1}{\sqrt{2}} - \sqrt{\frac{2}{7}} \sum_{n \text{ even}} \frac{p_n}{\sqrt{\sqrt{\pi} a n! 14^n}} \frac{n! (-1)^{n/2}}{(n/2)!} \right] \frac{\bar{U}}{B}, \tag{5.27}$$

$$\frac{v\tau_s}{a} = \frac{\bar{U}}{B} \frac{4\sqrt{2}}{7} \sum_{n \text{ odd}} \frac{p_n}{\sqrt{\sqrt{\pi} a n! 14^n}} \frac{(n+1)! (-1)^{(n+1)/2}}{[(n+1)/2]!} \tag{5.28}$$

for the fixed point solution. Similarly, for Eq. (5.2), the left-hand side of the equation is

$$\tau_d \frac{\partial p(x, t)}{\partial t} = -\frac{\dot{z}\tau_d}{a} \sum_n \left[\left(\sqrt{\frac{n}{2}} p_{n-1} - \sqrt{\frac{n+1}{2}} p_{n+1} \right) + \tau_d \dot{p}_n \right] v_n(x|z), \tag{5.29}$$

while the right-hand side reads

$$\begin{aligned}
& 1 - p(x, t) \left[1 + \tau_d \beta \frac{U(x, t)^2}{B} \right] \\
&= \sum_{n=0}^{\infty} p_n v_n - \frac{\tau_d \beta U_0^2}{B} \sqrt{\sqrt{\pi}} v_0 + \frac{\tau_d \beta U_0^2}{B} e^{-\frac{(x-z)^2}{2a^2}} \sum_{n=0}^{\infty} p_n v_n \\
&= \sum_{n=0}^{\infty} \left(p_n - \frac{\tau_d \beta U_0^2}{B} \sqrt{\sqrt{\pi} a} \delta_{n0} + \frac{\tau_d \beta U_0^2}{B} \sum_m C_{nm} p_m \right) v_n, \tag{5.30}
\end{aligned}$$

where C_{nm} is given by

$$C_{nm} = \sqrt{\frac{2}{3}} \left(\frac{1}{2} \right)^{n+m} \sum_{r+s=\text{even}} \frac{(-1)^{\frac{(m-s)-(n-r)}{2}} \sqrt{n!} \sqrt{m!}}{r!(n-r)!s!(m-s)!} \left(\frac{1}{3} \right)^{\frac{r+s}{2}} \frac{(r+s)!(n+m-r-s)!}{\left(\frac{r+s}{2} \right)! \left(\frac{n+m-r-s}{2} \right)!}. \tag{5.31}$$

The equations for the fixed point solution is

$$-\frac{\dot{z}\tau_d}{a} \sum_n \left(\sqrt{\frac{n}{2}} p_{n-1} - \sqrt{\frac{n+1}{2}} p_{n+1} \right) = p_n - \frac{\bar{\beta} \bar{U}^2}{B} \sqrt{\sqrt{\pi} a} \delta_{n0} + \frac{\bar{\beta} \bar{U}^2}{B} \sum_m C_{nm} p_m \quad (5.32)$$

Eq. (5.27), (5.28) and (5.32) can be used to determine the region of existence of bumps, including stationary and spontaneously moving. Similarly, the region of existence can be figured out by drawing parabolas. For a given $\bar{\beta} \bar{U}^2/B$, \bar{U}/B , $\tau_d \dot{z}/a$ and p_n can be solved. With these constants, \bar{k} is given by

$$\bar{k} = \frac{8}{\left(\frac{\bar{\beta} \bar{U}^2}{B}\right)} \bar{\beta} - 8 \left(\frac{\frac{\bar{\beta} \bar{U}^2}{B}}{\frac{\bar{U}}{B}} \right)^2 \bar{\beta}^2. \quad (5.33)$$

Now the parameter \bar{k} is rewritten as a function of $\bar{\beta}$ with constants $\bar{\beta} \bar{U}^2/B$ and \bar{U}/B . The region of existence can then be figured out by this family of parabolas. Considering the stability condition similar to Eq. (5.19) and using different restrictions, we may find out the boundaries for different states. To study the stability, we let $\epsilon = \bar{U} - \bar{U}^*$ and $\delta_n = p_n - p_n^*$. The equation system similar to Eq. (5.19) is then

$$\frac{d}{dt} \begin{pmatrix} \epsilon \\ \delta_0 \\ \vdots \\ \delta_n \end{pmatrix} = \begin{pmatrix} M_{-1,-1} & M_{-1,0} & \cdots & M_{-1,n} \\ M_{0,-1} & & & \vdots \\ \vdots & & & \vdots \\ M_{n,-1} & \cdots & \cdots & M_{n,n} \end{pmatrix} \begin{pmatrix} \epsilon \\ \delta_0 \\ \vdots \\ \delta_n \end{pmatrix}, \quad (5.34)$$

where

$$M_{-1,-1} = \frac{1}{\tau_s} \left[\frac{2}{B} - 1 \right], \quad (5.35)$$

$$M_{-1,\text{even } n} = -\frac{1}{\tau_s} \frac{\rho J_0 U_0^*}{B} \sqrt{\frac{2}{7}} \frac{1}{\sqrt{\sqrt{\pi} a n! 14^n}} \frac{n! (-1)^{\frac{n}{2}}}{\left(\frac{n}{2}\right)!}, \quad (5.36)$$

$$M_{-1,\text{odd } n} = 0, \quad (5.37)$$

$$M_{n,-1} = \frac{1}{\tau_d} \left[\frac{2-B}{B U_0^*} \frac{\dot{z}\tau_d}{a} \left(\sqrt{\frac{n}{2}} p_{n-1}^* - \sqrt{\frac{n+1}{2}} p_{n+1}^* \right) + \frac{2\tau_d \beta U_0^*}{B^2} \delta_{n0} - \frac{2\tau_d \beta U_0^*}{B^2} \sum_m C_{nm} p_m^* \right], \quad (5.38)$$

$$\begin{aligned}
M_{n,\text{even } l} = & \frac{1}{\tau_d} \left[-1 + \frac{\tau_d \rho J_0 U_0^*}{\tau_s B} \frac{4\sqrt{2}}{7} \frac{(l+1)!(-1)^{\frac{n+1}{2}}}{\sqrt{\sqrt{\pi} a l! 14^l (\frac{l+1}{2})!}} \left(\sqrt{\frac{n}{2}} p_{n-1}^* - \sqrt{\frac{n+1}{2}} p_{n+1}^* \right) \right. \\
& \left. + \frac{\tau_d \dot{z}}{a} \left(\sqrt{\frac{n}{2}} \delta_{l,n-1} - \sqrt{\frac{n+1}{2}} \delta_{l,n+1} \right) - \frac{\tau_d \beta U_0^{*2}}{a} \right], \tag{5.39}
\end{aligned}$$

$$M_{n,\text{odd } l} = \frac{1}{\tau_d} \left[-1 + \frac{\tau_d \dot{z}}{a} \left(\sqrt{\frac{n}{2}} \delta_{l,n-1} - \sqrt{\frac{n+1}{2}} \delta_{l,n+1} \right) - \frac{\tau_d \beta U_0^{*2}}{a} \right]. \tag{5.40}$$

The eigenvalues can be found numerically. To have a stable solution, the all eigenvalues should be negative in its real part.

To figure out the phase boundary of different solutions, we have to put different restrictions on the above equation system. For example, fixing \dot{z} to be zero, the boundary of amplitude stable static states can be obtained. By searching stable solutions with $\dot{z} = 0$, the boundary of stable static bumps should be obtained. If there is no restriction on \dot{z} , the boundary for moving bump can be obtained. The predicted boundaries are as shown in figure 5.1. In figure 5.1, there is a region labeled by ‘Metastatic or Moving’. As shown above, the static bump in this region is stable in amplitude. However, by using the general perturbation theory, it is found that, in this region, the static bump will no longer be static if there is a distortion that is asymmetric, about the center of mass of the neuronal input bump, distortion is added on the synaptic depression. Then, the bump will move like the bumps in the spontaneously moving region. In contrast, states in the stable static region can maintain static, even though an asymmetric distortion is added to the synaptic depression.

It is notable that, in inset of figure 5.1, the predicted phase boundary between moving phase and silent phase cannot predict so well when $\bar{\beta}$ is large. Since the prediction cannot be improved significantly by using a higher order perturbation on $p(x, t)$, this difference between simulation and prediction should be due to the assumption on $U(x, t)$ in the calculation. In Eq. (5.4), $U(x, t)$ is assumed to be a perfect Gaussian function. However, when $\bar{\beta}$ is large, this assumption may not work well. As shown in figure 5.10, the predictions using perturbation up to $n = 10, 11, 60, 61$ are plotted. As we can see, the predicting power can be improved by using a higher order perturbation. However, the improvement is not very large, even though the $n = 61$ perturbation is used. Also, the odd order perturbations always overestimate the phase boundary, and the even order perturbations underestimate the phase boundary.

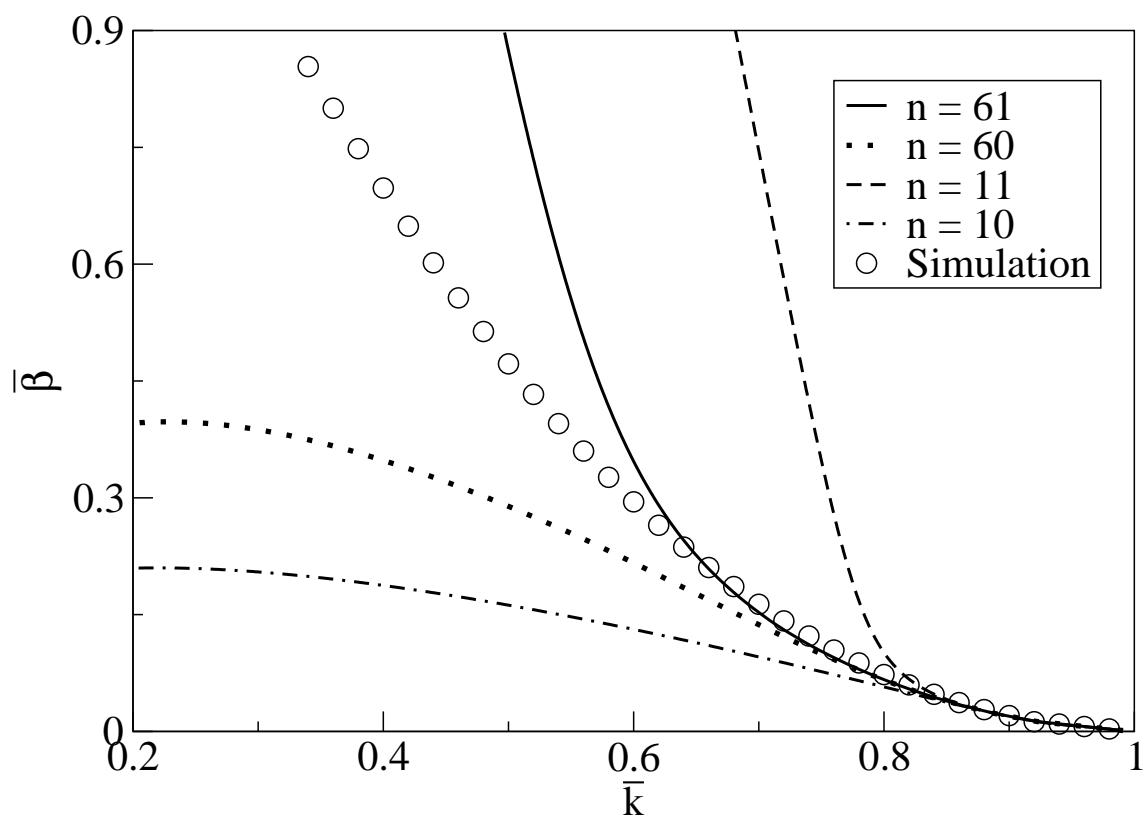


Figure 5.10: Comparison of predictions with perturbation with various orders. The predicted phase boundary is oscillating around the simulation result.

5.3.3 Slow-decaying Behavior

To understand the plateau behavior shown in figure 5.3, we may study the U -nullcline, i.e. $\partial U/\partial t = 0$, and p_0 -nullcline, i.e. $\partial p_0/\partial t = 0$, obtained from Eqs. (5.10) and (5.11). The nullclines are plotted in figure 5.11. Choosing the parameters used in figure 5.3, i.e. point P in figure 5.1, there is no intersection between two nullclines. So, there is no stationary solution.

In figure 5.11, four classes of initial conditions are marked. Initial conditions of neuronal input bump excited by stimuli should be of class A. In figure 5.3, the initial condition of the simulation for class A is prepared by using a stimulus $\alpha = 0.5$. According to Eq. (5.10), the decay will be slowest near the peak position of the U -nullcline. So, there is a relative long period that the height of the bump decays slowly. For comparison, the simulation counterpart of figure 5.11 is plotted in figure 5.12.

For class B and C, since $\tau_s \ll \tau_d$, the state of the system converges first to the U -nullcline. At this stage, the change in \bar{U} will depend on the change in p_0 with the time scale τ_d . Therefore, the change in \bar{U} will be very slow and \bar{U} will have a very long lifetime. For case D, \bar{U} will be repelled by the unstable branch of U -nullcline. Therefore, the neuronal input bump will decay with a time scale τ_s .

5.3.4 Tracking along the Preferred Stimulus Space

An important feature of a CANN is its capacity of tracking time-varying stimuli. In this subsection, we explore how synaptic depression affects the tracking performance of the network. Two scenarios are considered: 1) an external stimulus experiences an abrupt change; and 2) external stimuli change continuously over time.

5.3.4.1 Catching up an abrupt change in stimuli

Tracking is an important feature for the decoding process to adapt to the changing stimulus. As shown in figure 5.5, the neuronal bump was initially stable at $x = 0$ ($t < 0$). At $t = 0$, the position of the stimulus change from $x = 0$ to $x = 1.5$ abruptly. Then the synaptic input track to catch up with the new position of the stimulus. In this part, we will discuss this process and how synaptic depression affects the tracking performance. For simplicity, we take the external stimulus $I^{\text{ext}}(x|z_0) = \alpha \exp[-(x - z_0)^2/(4a^2)]$, where z_0 is the center of mass of the stimulus and α represents the strength of the stimulus.

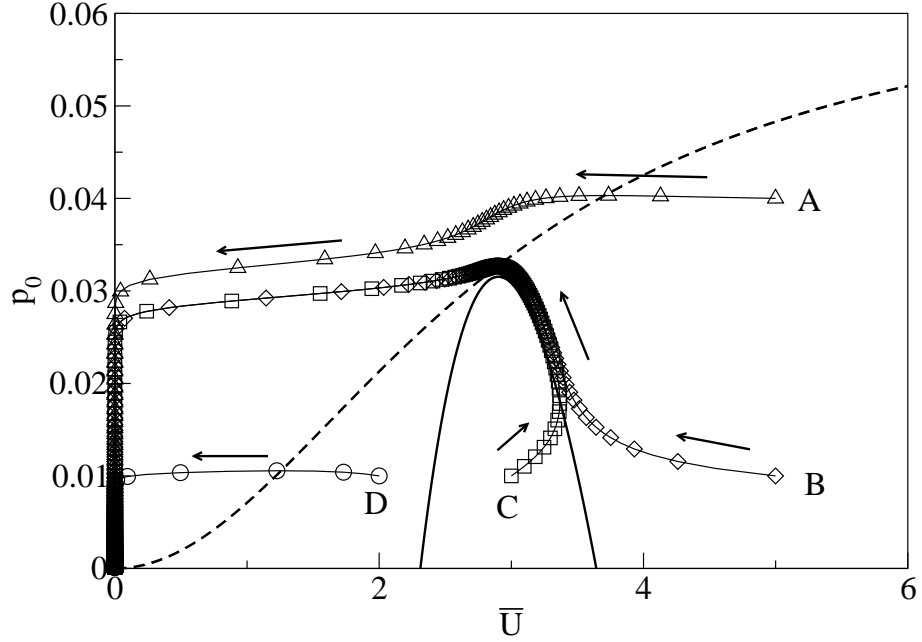


Figure 5.11: Nullclines and plots of $p_0(t)$ against \bar{U} . Symbols: numerical result from Eqs. (5.10) and (5.11) plotted every $2\tau_s$. Dashed line: U -nullcline. Solid line: p_0 -nullcline. Parameter: $\bar{k} = 0.95$, $\bar{\beta} = 0.0085$.

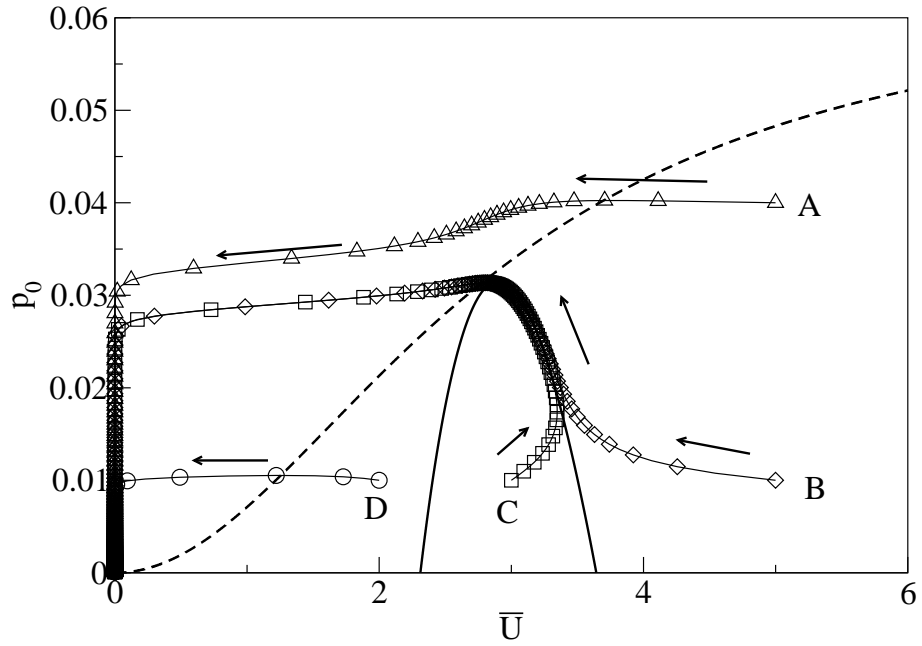


Figure 5.12: The simulation counterpart of figure 5.11. These results show that the predictions by Eqs. (5.17) and (5.18) agree with the simulations.

Using projection, we may approximate $I^{\text{ext}}(x|z_0)$ by

$$I^{\text{ext}}(x|z_0) \approx \alpha \exp \left[-\frac{(z - z_0)^2}{8a^2} \right] \exp \left[-\frac{(x - z)^2}{4a^2} \right] + \alpha \frac{z_0 - z}{2a} \exp \left[-\frac{(z - z_0)^2}{8a^2} \right] \frac{x - z}{a} \exp \left[-\frac{(x - z)^2}{4a^2} \right]. \quad (5.41)$$

By comparing terms with Eq. (5.25) and (5.26), we have

$$\tau_s \frac{dU_0}{dt} = \alpha \exp \left[-\frac{(z - z_0)^2}{8a^2} \right] + \frac{\rho J_0 U_0^2}{\sqrt{2}B} - \frac{\rho J_0 U_0^2}{B} \sqrt{\frac{2}{7}} \sum_{n \text{ even}} \frac{p_n}{\sqrt{\pi a n! 14^n}} \frac{n! (-1)^{\frac{n}{2}}}{(\frac{n}{2})!} - U_0 \quad (5.42)$$

$$\dot{z} = \frac{\alpha}{\tau_s} \frac{1}{U_0} (z_0 - z) \exp \left[-\frac{(z - z_0)^2}{8a^2} \right] + \frac{\rho J_0 U_0^2}{B} \frac{8\sqrt{2}a}{7\tau_s} \sum_{n \text{ odd}} \frac{p_n}{\sqrt{\pi a n! 14^n}} \frac{(n+1)! (-1)^{(n+1)/2}}{[(n+1)/2]!}. \quad (5.43)$$

As shown in Eq. (5.43), the tracking speed will be affected by the presence of the synaptic depression. The net speed of the moving bump will be the sum of the spontaneously moving speed and a component due to the attraction of stimulus. As shown in figure 5.7, the Eq. (5.43) can predict the movement of the center of mass of the synaptic input with only a small difference with the simulation results. One may argue that, this difference could be due to the difference in heights of bumps in the two cases. However, the difference in height between the neuronal input bumps cannot account for the overshoot effect. This overshoot effect should be due to the terms with odd n in Eq. (5.43).

Note that, if the order of perturbation is low, e.g. $n = 1$, the overshooting will be overestimated. However, the basic feature of the overshooting behavior can still be captured, i.e. the center of mass of the neuronal bump is predicted to overshoot, and then relax to the new position of the stimulus.

5.3.4.2 Tracking time-varying stimuli

Moving objects are examples of continuously moving stimuli. To analyze these cases, for simplicity, we replace $z_0 = vt$ in Eq. (5.41). With this, we can predict the center of mass of the bump for a given speed of the stimulus, v , as shown in figure 5.13. In this figure, unlike the case of abruptly-change of stimulus, the initial speed of the bump is almost zero. When the stimulus is moving away from the synaptic input bump, the bump will accelerate to catch up with the speed of the stimulus. After a long enough time, the

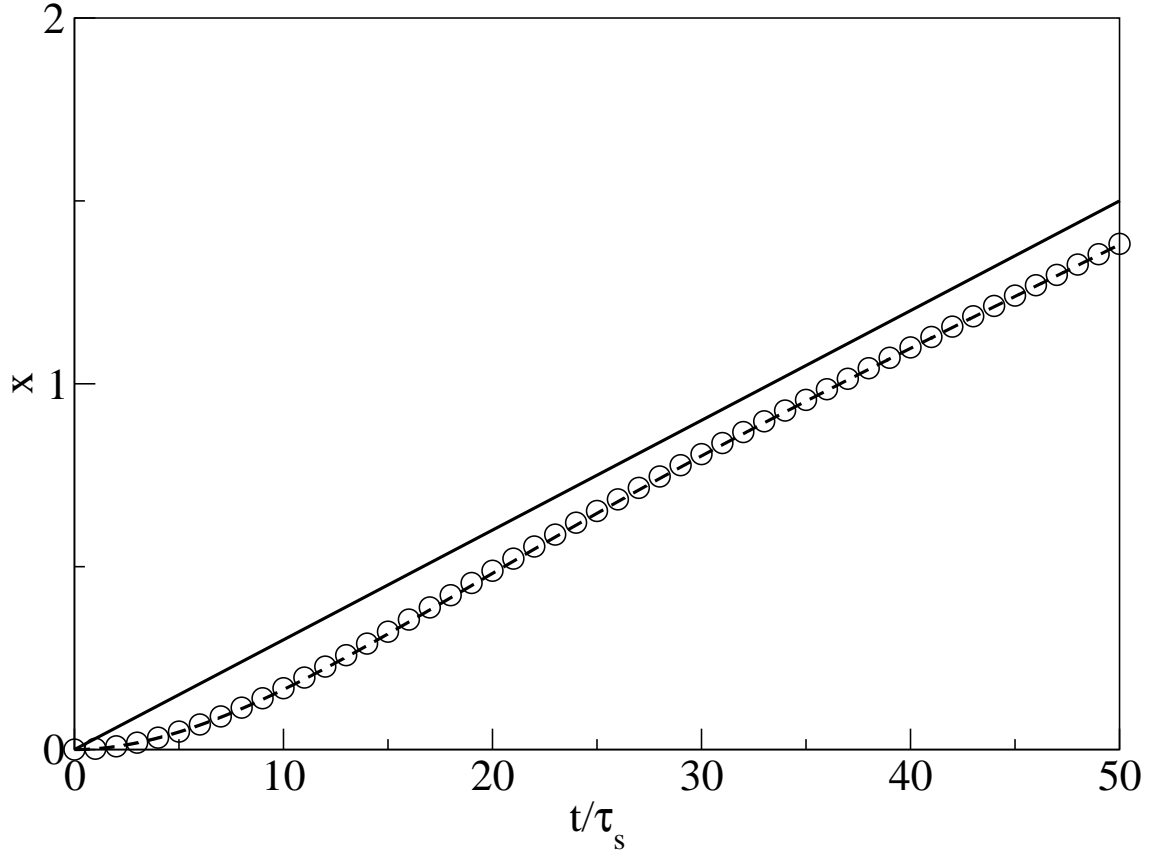


Figure 5.13: Tracking of a neuronal bump with continuously moving stimulus. Symbols: simulation result of center of mass of neuronal input bump. Dashed line: 11th order perturbation prediction of Eq. (5.43). Solid line: Continuously moving stimulus with speed 0.03. Parameter: $\alpha = 0.1$, $\bar{k} = 0.5$, $\bar{\beta} = 0.01$, other parameters are the same as figure 5.7.

separation between the bump and the stimulus converges to a constant.

Similar to the case of an abruptly changing stimulus, when the synaptic depression is large, the behavior of the motion of the bump is more surprising. As shown in figure 5.14, the center of mass of the synaptic input does not lag behind the stimulus eventually. The reason is that the contribution due to the second term of Eq. (5.43) is large. If the stimulus is not running very fast, the speed of the bump may be faster than the stimulus. However, when the bump goes advance the stimulus, the bump will decelerate due to the contribution by the first term of Eq. (5.43). Then, the separation between the bump and the stimulus will converge to be a constant. It is remarkable that the bump can lead the moving stimulus.

If the order of perturbation is too low, e.g. $n = 1$, the speed of the neuronal bump will be overestimated. As a result, the neuronal bump will overtake the stimulus and the separation will tend to infinity.

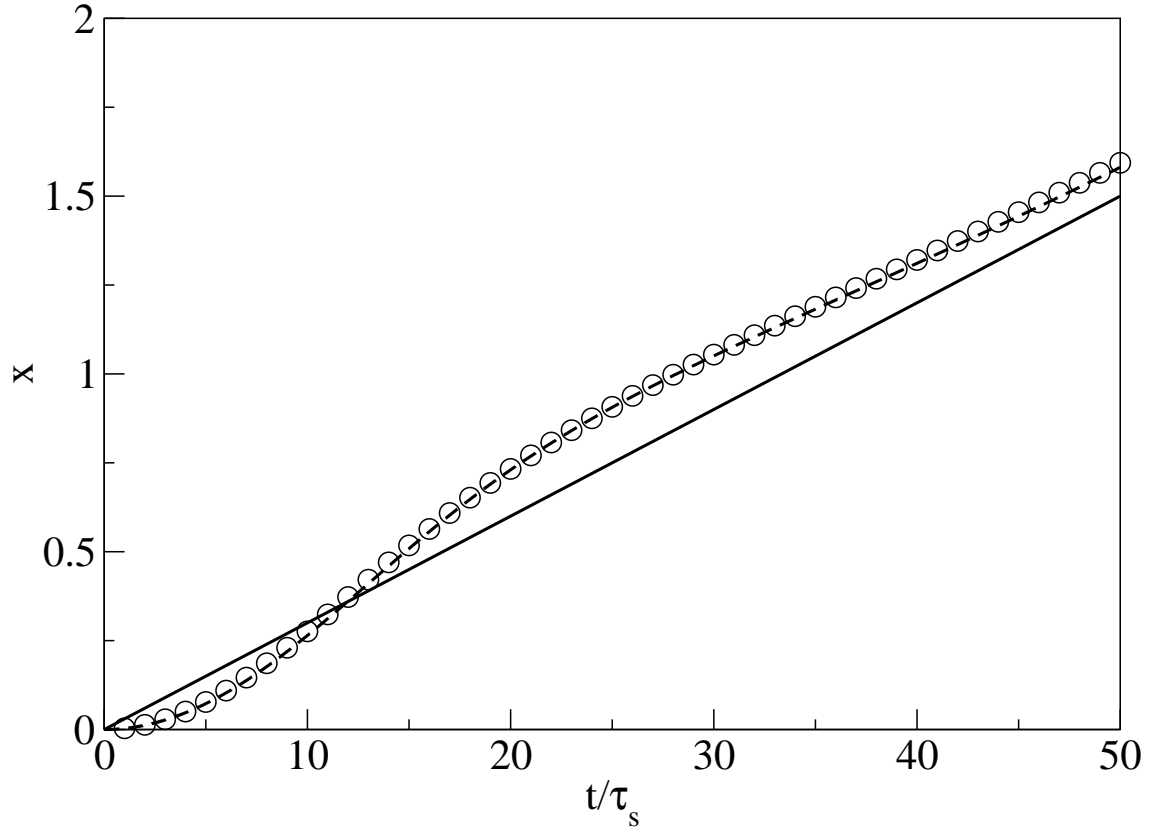


Figure 5.14: Tracking of a neuronal bump with continuously moving stimulus. Symbols: simulation result of center of mass of neuronal input bump. Dashed line: 11th order perturbation prediction of Eq. (5.43). Solid line: Continuously moving stimulus with speed 0.03. Parameter: $\alpha = 0.1$, $\bar{k} = 0.5$, $\bar{\beta} = 0.05$, other parameters are the same as figure 5.7.

5.4 Synaptic Facilitation

For the CANNs with facilitation, the dynamics of the synaptic input is given by[15]

$$\tau_s \frac{\partial U(x, t)}{\partial t} = -U(x, t) + \rho \int dx' J(x, x') f(x', t) r(x') + I^{\text{ext}}(x, t), \quad (5.44)$$

where the function $f(x, t)$ models the effect of facilitation. The dynamics of the function $f(x, t)$ is given by

$$\tau_f \frac{\partial f(x, t)}{\partial t} = -f(x, t) + 1 + \Omega [f_0 - f(x, t)] r(x), \quad (5.45)$$

where Ω controls how fast the facilitation reacts to the neural response, f_0 controls the maximum value of $f(x, t)$ and τ_f is the time constant of facilitation, which is fixed to be $50\tau_s$. Suppose a steady stationary solution to Eqs. (5.44) and (5.45) exists. By taking $\partial f / \partial t = 0$, we have

$$\begin{aligned} f(x) [1 + \Omega r(x)] &= 1 + \Omega f_0 r(x) \\ f(x) &= \frac{1 + \Omega f_0 r(x)}{1 + \Omega r(x)} \\ f(x) &= f_0 - (f_0 - 1) \frac{1}{1 + \Omega r(x)}. \end{aligned} \quad (5.46)$$

From this equation, if $r(x)$ is bump-shaped, $f(x)$ should also be bump-shaped with an offset 1. This result is comparable to Eq. (5.3), but the effect is *reversed*. We will demonstrate it by comparing the tracking performance.

5.4.1 Tracking Performance: A comparison with Synaptic Depression

In the simulation experiments, the neuronal input bumps will be prepared by a static stimulus sitting at 0, given by $I^{\text{ext}}(x|z_0) = \alpha \tilde{U}_0 \exp [-(x - z_0)^2 / (4a^2)]$. The position of the stimulus will be changed when the neuronal input bump becomes steady. With this setting, a bump-shaped $f(x, t)$ will be built due to the bump-shaped $r(x)$. As analyzed in the case of synaptic depression, the pit-shaped $p(x, t)$ enhances the performance and reduces the reaction time. Conversely, this bump-shaped $f(x, t)$ will slow down the tracking process and lengthens the reaction time, as shown in figure 5.15.

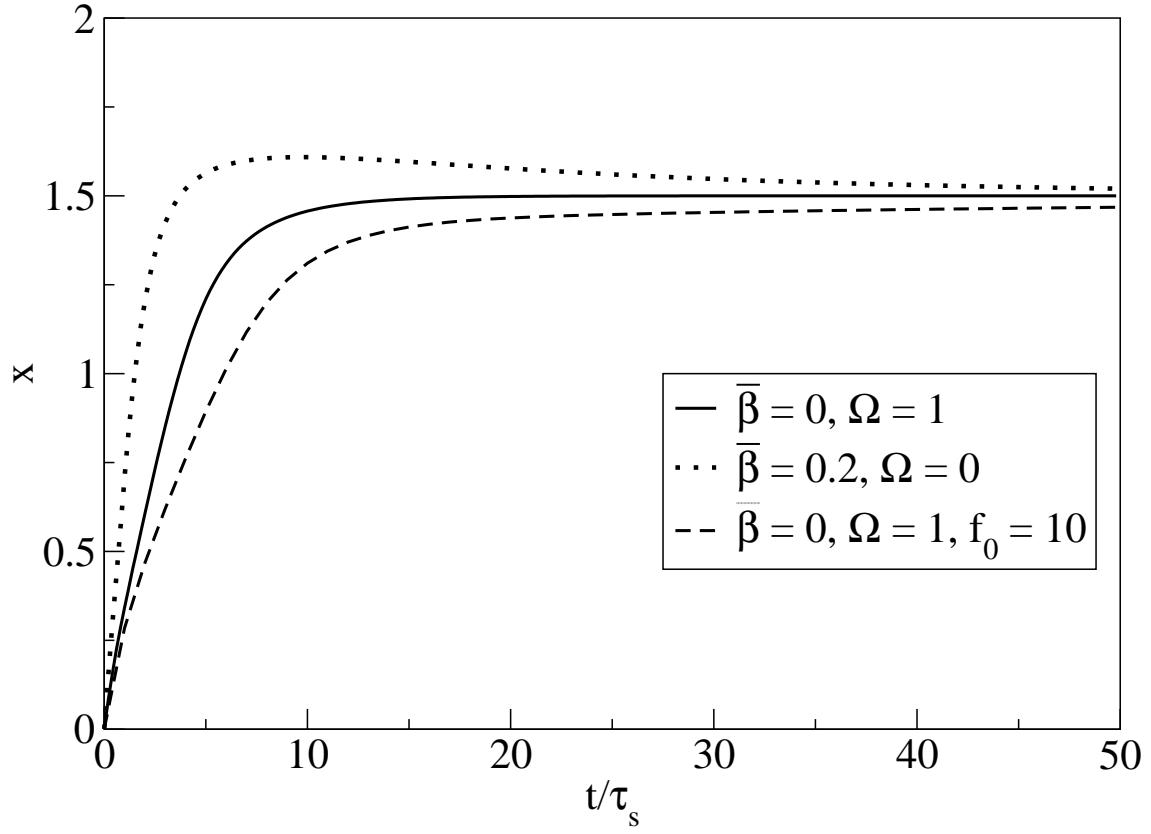


Figure 5.15: Comparison between system with synaptic depression, synaptic facilitation, or without time-dependent coupling. Parameter: $\alpha = 0.5$, $\bar{k} = 0.5$, other parameters are the same as figure 5.7.

5.5 Summary

In this chapter, the work on the plasticity of neural couplings was presented. We have shown that, by both theory and simulation, the system with short-term depression (STD) can support static and spontaneously moving bump solution. In figure 5.1, for different combinations of parameters $(\bar{k}, \bar{\beta})$, there are four phases regions on the phase diagram. They are moving phase, silent phase, static phase and metastatic phase. The STD can generate the traveling pulse, which can be observed in the experiments [34].

The plateau behavior is also a remarkable observation in this model. By using a carefully chosen combination of parameters, we can obtain the slow-decaying behavior, as shown in figure 5.3. This behavior is particularly important to the nervous system, because 1) it may provide a long enough duration of the neuronal input bump to decay slowly, so that the postprocessing layer of the nervous system may have more time to react, once the stimulus is remove abruptly, 2) it can shut off the neuronal response eventually, after the stimulus is removed. In figures 5.5 and 5.6, we have demonstrated that this selected set of parameters may track to catch up with the change of position of stimulus.

For the tracking performance, the presence of STD may enhance the reaction of the tracking process, thanks to the positional instability provided by STD. By Eq. (5.43), the motion of the neuronal input bump will be driven by stimulus and synaptic depression. Also, because of the synaptic depression, the neuronal bump may overshoot the target. In contrast, the reverse effect, namely STF, will slow down the tracking process as compared in figure 5.15.

Chapter 6

Conclusion

In this thesis, the work on the dynamics of CANNs with Mexican-hat couplings, 2D CANNs with divisive inhibition and CANNs with time-dependent couplings is presented. In chapter 2, the Mexican-hat couplings are obtained by using an annealing learning schedule on the energy function [29], Eq. (3.5). The advantage of this approach is that we only need to know the slope of the expected bump function, but not the exact form of the bump. The compensation of this approach is that the extra term ω_0 is needed to control the average amplitude of the coupling strength.

Unlike the 1D CANNs with divisive inhibition [28, 26], one-bump solutions are not the only type of solutions. In figures 3.2 - 3.4, if the change of the position of stimulus is too big, a new bump will grow up at the position of the new position of the stimulus. Because the inhibition effect is not global, this kind of spurious solutions is allowed. Figures 3.6 and 3.7 show that, when ω_0 , the average amplitude of coupling strength, or k is too large, this kind of change of stimulus will easily excite a spurious solution when the stimulus changes its position. This is because, in these settings, the system will be too sensitive to small changes. If the sensitivity is too high, a little perturbation of the neuronal input can excite a local bump, due to the strong local excitational connection. For 2D networks with Mexican-hat couplings, the instability behavior is similar, shown in figures 3.13 - 3.17. With some combinations of parameters, the bump cannot track well, and this behavior agrees with the expectation of [25].

For the 2D CANNs with divisive inhibition, by using the similar perturbative approach [28, 26], we can decompose the distortion around the stable stationary into different modes in terms of eigenfunctions of 2D quantum harmonic oscillator [14]. By choosing the eigenfunctions in rectangular coordinates, we may obtain the set of equations predicting the motion of the bump, Eqs. (4.12) and (4.18). Besides using the rectangular coordinates, we may also choose the polar coordinates due to the fact that the system is also rotationally symmetric. Once the polar coordinates are employed,

the eigenfunctions of the kernel \mathcal{G} with arguments (r, θ) can be obtained, as shown in figures 4.3-4.8. Some of them are comparable to the 1D counterpart [28, 26], because they look like the 2D version of the 1D eigenfunctions. For example, Ψ_{00} , $\Psi_{1\pm 1}$, Ψ_{20} and $\Psi_{3\pm 1}$ represent the distortion in height, position, width and skewness, respectively, of the bump. However, other eigenfunctions are special to 1D CANNs. $\Psi_{2\pm 2}$ and $\Psi_{3\pm 3}$ are examples corresponding to cigar-shaped and triangular-shaped distortions. It can be shown that, $\Psi_{n\pm n}$ are the eigenfunctions of \mathcal{G} . The dynamics of different modes of distortion are shown in figure 4.10.

In chapter 4, we discuss the effect of the plasticity of neuronal couplings. This effect depends on the neuronal response, and is largely studied in the literature [35, 36, 16, 37, 15, 32], especially the short-term depression, whose effect is the weakening of the original neuronal couplings. York et al [32] found that in their model with synaptic depression the system will be stable to static bump solution, spontaneously moving bump solution, homogeneous solution or silent solution, in different regions in the space of parameters. Studying a similar model, we discover the similar behaviors. In figure 5.1, the neuronal input bump may be static, spontaneously moving or silent. However, in the above analysis, it can be shown that the static bump can exist with the amplitude stable but the position is unstable. For example, in the *metastatic* region, if the initial condition is carefully prepared, a static bump can be observed. However, if a small perturbation is added to the neuronal input, the neuronal input bump will start to go, due to the positional instability. The origin of the moving behavior is explained in figure 5.2.

If the parameters $(\bar{k}, \bar{\beta})$ is selected to be near marginally unstable, say point P in figure 5.1, the plateau, or slow-decaying, behavior can be easily observed, because of the absence of the fixed point in Eqs. (5.10) and (5.11). The plateau behavior is important in biological systems, because, with this behavior, the nervous system can shut down the neuronal response once the stimulus disappear. Also, since the bump is slowly decaying, it gives a sufficient long duration for the postprocessing layers to work with the input signals.

Short-term depression on synaptic couplings can enhance the tracking performance. As shown in figure 5.7, the tracking performance can be improved by synaptic depression. However, there is a compensation of this improvement. As can be seen in the same figure, the bump overshoots the target, $z_0 = 1.5$, which can be explained by the extra term of Eq. (5.43). We have also shown that another kind of plasticity, synaptic facilitation, has a reverse effect to synaptic depression. In figure 5.15, the presence of facilitation slows down the tracking process.

All in all, in this thesis, we have discussed different kinds of fully connected continuous attractor neural networks. CANNs with Mexican-hat coupling is commonly used in various models to demonstrate the behavior of the systems. The tracking properties is explored in chapter 2. In chapters 3 and 4, analyses and simulations are done on the dynamics of the neuronal input. The key spirit of the calculations is to decompose the complicated functions with respect to a set of orthogonal and complete functions. Here, we use the eigenfunctions of the quantum harmonic oscillator, which are known to be orthogonal to each other. We may take the above calculations as examples of applying the perturbative approach on models.

Appendix A

Derivation of the interacting kernel matrix $\mathcal{F}_{nmn'm'}$ for 2D CANNs with Divisive Inhibition

From Eq. (4.7), we obtain

$$F(\mathbf{x}, \mathbf{x}' | \mathbf{z}) = \frac{2}{\pi a^2} \exp \left[-\frac{|\mathbf{x} - \mathbf{x}'|^2}{2a^2} \right] \exp \left[-\frac{|\mathbf{x}' - \mathbf{z}|^2}{4a^2} \right] - 2k\rho r_0 \exp \left[-\frac{|\mathbf{x} - \mathbf{z}|^2}{4a^2} \right] \exp \left[-\frac{|\mathbf{x}' - \mathbf{z}|^2}{4a^2} \right]. \quad (\text{A.1})$$

Similar to [26], considering $g_{nm}(\mathbf{x}) = \int d\mathbf{x}' u_{n'm'}(\mathbf{x}') F(\mathbf{x}, \mathbf{x}')$, which is given by

$$g_{n'm'}(\mathbf{x}) = \frac{2(-\sqrt{2})^{m'+n'}}{\sqrt{2\pi a^2 m'! n'! 2^{m'+n'}}} \left(\frac{d}{dx_1} \right)^{n'} e^{-\frac{(x_1 - z_1)^2}{4a^2}} \left(\frac{d}{dx_2} \right)^{m'} e^{-\frac{(x_2 - z_2)^2}{4a^2}} - 2k\rho r_0 \sqrt{2\pi a^2} \exp \left[-\frac{|\mathbf{x} - \mathbf{z}|^2}{4a^2} \right] \delta_{n'0} \delta_{m'0}, \quad (\text{A.2})$$

where $\mathbf{x} = (x_1, x_2)$ and $\mathbf{z} = (z_1, z_2)$. For $n'm' > 0$,

$$\begin{aligned} \mathcal{F}_{nmn'm'} &= \int d\mathbf{x} u_{nm}(\mathbf{x}) g_{n'm'}(\mathbf{x}') \\ &= \sqrt{\frac{m'! n'!}{m! n!}} \frac{2}{2^{m'+n'}} \frac{(-1)^{\frac{m'+n'-m-n}{2}}}{2^{\frac{m'+n'-m-n}{2}} \left(\frac{m'-m}{2} \right)! \left(\frac{n'-n}{2} \right)!}, \end{aligned} \quad (\text{A.3})$$

which the detail calculation is similar to appendix A. For \mathcal{F}_{0000} ,

$$\begin{aligned}
F_{0000} &= 2 - 2k\rho r_0 \sqrt{2\pi a^2} \int d\mathbf{x} \frac{1}{\sqrt{2\pi a^2}} \exp\left[-\frac{|\mathbf{x} - \mathbf{z}|^2}{4a^2}\right] \exp\left[-\frac{|\mathbf{x} - \mathbf{z}|^2}{4a^2}\right] \\
&= 2 - 2k\rho r_0 \left(\sqrt{2\pi a^2}\right)^2 \\
&= 2 - 4\pi a^2 k\rho r_0
\end{aligned}$$

Appendix B

Derivation of Bump Speed for 2D CANNs with Divisive Inhibition

Similar to that in appendix B, before the derivation of speed of the bump, we have to first deal with the self-consistent condition, Eq. (4.17). Suppose we have the expansion $U(\mathbf{x}, t) = \sum_{nm} a_{nm}(t) u_{nm}(\mathbf{x}, \mathbf{z})$, where $\mathbf{z} = (z_1, z_2)$ and $\mathbf{x} = (x_1, x_2)$ Eq. (4.17) can be rewritten as

$$\iint d\mathbf{x} (\mathbf{x} - \mathbf{z}) U(\mathbf{x}, t) = 0. \quad (\text{B.1})$$

Let's consider the first coordinate of \mathbf{z} , z_1 .

$$\iint d\mathbf{x} (x_1 - z_1) U(\mathbf{x}, t) = 0 \quad (\text{B.2})$$

Therefore, we have

$$\begin{aligned} \sum_{nm} \int u_m(x_2|z_2) dx_2 \int u_n(x_1|z_1) (x_1 - z_1) dx_1 &= 0 \\ \sum_{\text{even } m} \int u_m(x_2|z_2) dx_2 \left[\sum_{\text{odd } n} \int u_n(x_1|z_1) (x_1 - z_1) dx_1 \right] &= 0. \end{aligned} \quad (\text{B.3})$$

Inside the square bracket, the result is known in appendix B. For the integral $\int u_m(x_2|z_2) dx_2$, by [38], there is a integration formula such that

$$\int_{-\infty}^{\infty} e^{-(x-y)^2} H_n(\alpha x) dx = \pi^{1/2} (1 - \alpha^2)^{n/2} H_n \left(\frac{\alpha u}{(1 - \alpha^2)^{1/2}} \right). \quad (\text{B.4})$$

By using this formula, we have

$$\begin{aligned}
\int u_m(x_2|z_2)dx_2 &= \frac{2a}{\sqrt{\sqrt{2\pi am!}2^m}}\sqrt{\pi}(-1)^{m/2}H_n(0) \\
&= \frac{2a}{\sqrt{\sqrt{2\pi am!}2^m}}\sqrt{\pi}(-1)^{m/2}(-1)^{m/2}2^{m/2}(m-1)!! \\
&= \sqrt{2\sqrt{2\pi}a}\sqrt{\frac{(m-1)!!}{m!!}}.
\end{aligned} \tag{B.5}$$

Hence,

$$\sum_{\text{even } m, \text{ odd } n} \sqrt{\frac{(m-1)!!}{m!!}} \sqrt{\frac{n!!}{(n-1)!!}} = 0. \tag{B.6}$$

Similar equation can be obtained for z_2 .

If the changing stimulus is changing along the x -axis, we can let $z_2 = 0$. Then, we can multiply Eqs. (4.12) by $\sqrt{\frac{(m-1)!!}{m!!}}\sqrt{\frac{n!!}{(n-1)!!}}$, and then sum them up. The time derivatives of a_{nm} will vanish. By rearranging terms, we can obtain Eq. (4.18).

Appendix C

Proof: $\Psi_{l\pm l}$ are the eigenfunctions of \mathcal{G}

Provided that

$$\mathcal{G}(\vec{r}, \vec{r}') = \frac{2}{\pi a^2} \exp\left[-\frac{|\vec{r} - \vec{r}'|^2}{2a^2}\right] \exp\left[-\frac{|\vec{r}' - \vec{z}|^2}{4a^2}\right] - 2k\rho r_0 \exp\left[-\frac{|\vec{r} - \vec{z}|^2}{4a^2}\right] \exp\left[-\frac{|\vec{r}' - \vec{z}|^2}{4a^2}\right], \quad (\text{C.1})$$

and

$$\Psi_{l\pm l}(r, \theta) = \psi_{l\pm l} = \frac{1}{\sqrt{\pi l!}} \left(\frac{r}{\sqrt{2}a}\right)^l e^{-\left(\frac{r}{\sqrt{2}a}\right)^l \pm i l \theta}. \quad (\text{C.2})$$

By appendix A and C, the second term of Eq. (C.1) will give non-zero contribution for only the basis function ψ_{00} . Therefore, we may consider

$$\mathcal{G}'(\vec{r}, \vec{r}') = \frac{2}{\pi a^2} \exp\left[-\frac{|\vec{r} - \vec{r}'|^2}{2a^2}\right] \exp\left[-\frac{|\vec{r}' - \vec{z}|^2}{4a^2}\right] \quad (\text{C.3})$$

with the same effect as the original one, for $l \geq 1$. To prove the proposition, we need one more tool, which is the raising operator R^+ . It works as

$$R^+ \psi_{l,l} = \sqrt{l+1} \psi_{l+1, (l+1)}, \quad (\text{C.4})$$

and is given by

$$R^+ = \frac{e^{i\theta}}{2} \left(\frac{r}{\sqrt{2}a} - \sqrt{2}a \frac{\partial}{\partial r} - \sqrt{2}a \frac{i}{r} \frac{\partial}{\partial \theta} \right). \quad (\text{C.5})$$

For simplicity, without lose of generality, we set $\vec{z} = \vec{0}$. Consider $R^+ \mathcal{G}'$, we have

$$\begin{aligned}
R^+ \mathcal{G}' &= R^+ \frac{2}{\pi a^2} \exp \left[-\frac{|\vec{r} - \vec{r}'|^2}{2a^2} \right] \exp \left[-\frac{|\vec{r}' - \vec{z}|^2}{4a^2} \right] \\
&= \frac{e^{i\theta}}{2} \left(\frac{r}{\sqrt{2}a} - \sqrt{2}a \frac{\partial}{\partial r} - \sqrt{2}a \frac{i}{r} \frac{\partial}{\partial \theta} \right) \\
&\quad \frac{2}{\pi a^2} \exp \left[-\frac{r^2 + r'^2 - 2rr' \cos(\theta - \theta')}{2a^2} \right] \exp \left[-\frac{r'^2}{4a^2} \right] \\
&= \frac{e^{i\theta}}{2} \frac{2}{\pi a^2} \left[\frac{r}{\sqrt{2}a} - \sqrt{2}a \left(-\frac{r}{a^2} + \frac{r'}{a^2} \cos(\theta - \theta') \right) + \sqrt{2}a i \frac{r'}{a^2} \sin(\theta - \theta') \right] \\
&\quad \exp \left[-\frac{r^2 + r'^2 - 2rr' \cos(\theta - \theta')}{2a^2} \right] \exp \left[-\frac{r'^2}{4a^2} \right] \\
&= \frac{e^{i\theta}}{2} \frac{2}{\pi a^2} \left[\frac{3r}{\sqrt{2}a} - \sqrt{2} \frac{r'}{a} e^{-i(\theta - \theta')} \right] \exp \left[-\frac{r^2 + r'^2 - 2rr' \cos(\theta - \theta')}{2a^2} \right] \exp \left[-\frac{r'^2}{4a^2} \right] \\
&= \frac{e^{i\theta}}{2} \frac{3r}{\sqrt{2}a} \mathcal{G}' - \mathcal{G}' \frac{r'}{\sqrt{2}a} e^{i\theta'}. \tag{C.6}
\end{aligned}$$

It is easy to check that, $\psi_{1\pm 1}$ are the eigenfunctions of \mathcal{G} with eigenvalue 1. Assume that, ψ_{kk} is a eigenfunction of \mathcal{G} with eigenvalue $2/2^k$. Then, we have

$$\begin{aligned}
\mathcal{G}' \psi_{kk} &= \frac{2}{2^k} \psi_{kk} \\
R^+ \mathcal{G}' \psi_{kk} &= R^+ \frac{2}{2^k} \psi_{kk} \\
\left(\frac{e^{i\theta}}{2} \frac{3r}{\sqrt{2}a} \mathcal{G}' - \mathcal{G}' \frac{r'}{\sqrt{2}a} e^{i\theta'} \right) \psi_{kk} &= \frac{2}{2^k} \sqrt{k+1} \psi_{k+1,k+1} \\
\frac{e^{i\theta}}{2} \frac{3r}{\sqrt{2}a} \mathcal{G}' \psi_{kk} - \mathcal{G}' \frac{r'}{\sqrt{2}a} e^{i\theta'} \psi_{kk} &= \frac{2}{2^k} \sqrt{k+1} \psi_{k+1,k+1} \\
\frac{e^{i\theta}}{2} \frac{3r}{\sqrt{2}a} \frac{2}{2^k} \psi_{kk} - \mathcal{G}' \sqrt{k+1} \psi_{k+1,k+1} &= \frac{2}{2^k} \sqrt{k+1} \psi_{k+1,k+1} \\
\frac{3}{2} \frac{2}{2^k} \psi_{k+1,k+1} - \mathcal{G}' \psi_{k+1,k+1} &= \frac{2}{2^k} \psi_{k+1,k+1} \\
\mathcal{G}' \psi_{k+1,k+1} &= \left(\frac{3}{2} - 1 \right) \frac{2}{2^k} \psi_{k+1,k+1} \\
&= \frac{2}{2^{k+1}} \psi_{k+1,k+1}. \tag{C.7}
\end{aligned}$$

By the principle of mathematical induction, $\mathcal{G} \psi_{ll} = (2/2^l) \psi_{ll}$. The proof for ψ_{l-l} follows.

Bibliography

- [1] W. C. McCulloch and W. Pitts, “A logical calculus of ideas immanent in nervous activity,” *Bulletin of Mathematical Biophysics*, vol. 5, pp. 115–133, 1943.
- [2] K. Steinbuch, “Die lernmatrix,” *Kybernetik*, vol. 1, pp. 36–45, 1961.
- [3] W. K. Taylor, *Electrical Simulation of Some Nervous System Functional Activities*. London 1985: Butterworths, 1956.
- [4] M. Tsodyks and T. Sejnowski, “Associative memory and hippocampal place cells,” *Int. Journal of Neural Systems*, vol. 6 (supp. 1995), pp. 81–86, 1995.
- [5] T. Kohonen, B. G., and C. R., “Statistical pattern recognition with neural networks: Benchmarking studies,” in *IEEE International Conference on Neural Networks (San Diego 1988)*, vol. I, (New York: IEEE), pp. 61–68, 1988.
- [6] R. P. Lippmann, “Review of neural networks for speech recognition,” *Neural Computation*, vol. 1, pp. 1–38, 1989.
- [7] A. Samsonovich and B. L. McNaughton, “Path integration and cognitive mapping in a continuous attractor neural network model,” *J. Neurosci.*, vol. 7, pp. 5900–, 1997.
- [8] A. P. Georgopoulos, M. Taira, and A. Lukashin, “Cognitive neurophysiology of the motor cortex,” *Science*, vol. 260, pp. 47–52, 1993.
- [9] D. O. Hebb, *The organization of behavior: a neuropsychological theory*. New York: Wiley, 1957.
- [10] A. P. Georgopoulos and J. T. Massey, “Cognitive spatial-motor process,” *Experimental Brain Research*, vol. 65, pp. 361–370, 1987.
- [11] M. R. Owen, C. R. Laing, and C. S., “Bumps and rings in a two-dimensional neural field: splitting and rotational instabilities,” *New Journal of Physics*, vol. 9, p. 378, 2007.
- [12] J. G. Taylor, “Neural ‘bubble’ dynamics in two dimensions: foundations,” *Biological Cybernetics*, vol. 80, no. 6, 1999.
- [13] H. Werner and T. Richter, “Circular stationary solutions in two-dimensional neural fields,” *Biological Cybernetics*, vol. 85, no. 3, 2001.
- [14] C. C. A. Fung, K. Y. M. Wong, and S. Wu, “Tracking dynamics of two-dimensional continuous,” *J. Phys.: Conference Series*, vol. 197, p. 012017, 2009.
- [15] M. V. Tsodyks, K. Pawelzik, and H. Markram, “Neural networks with dynamic synapses,” *Neural Computation*, vol. 10, pp. 821–835, 1998.
- [16] G. Mongillo, O. Barak, and M. Tsodyks, “Synaptic theory of working memory,” *Science*, vol. 319, pp. 1543–1546, 2008.
- [17] S. Amari, “Dynamics of pattern formation in lateral-inhibition type neural fields,” *Biological Cybernetics*, vol. 27, pp. 77–87, 1977.
- [18] B. Ermentrout, “Neural networks as spatial-temporal pattern-forming systems,” *Reports on Progress in Physics*, vol. 61, pp. 353–430, 1998.

- [19] H. S. Seung, "How the brain keeps the eyes still," *Proc. Acad. Sci. USA*, vol. 93, pp. 13339–13344, 1996.
- [20] S. Wu, K. Hamaguchi, and S. Amari, "Dynamics and computation of continuous attractors," *Neural Computation*, vol. 20, pp. 994–1025, 2008.
- [21] K.-C. Zhang, "Representation of spatial orientation by the intrinsic dynamics of the head-direction cell ensemble: a theory," *J. Neuroscience*, vol. 16, pp. 2112–2126, 1996.
- [22] S. Wu and S. Amari, "Computing with continuous attractors: Stability and on-line aspects," *Neural Computation*, vol. 17, pp. 2215–2239, 2005.
- [23] R. Ben-Yishai, R. Lev Bar-Or, and H. Sompolinsky, "Theory of orientation tuning in visual cortex," *Proc. Natl. Acad. Sci. USA*, vol. 92, pp. 3844–3848, 1995.
- [24] E. Folias and P. Bressloff, "Breathing pulses in an excitatory neural network," *SIAM J. Appl. Dyn. Syst.*, vol. 3, pp. 378–407, 2004.
- [25] D. Hansel and H. Sompolinsky, "Modeling feature selectivity in local cortical circuits," in *Methods in Neuronal Modeling: From Ions to Networks* (C. Koch and I. Segev, eds.), MIT Press, Cambridge, 1998.
- [26] C. C. A. Fung, K. Y. M. Wong, and S. Wu, "A moving bump in a continuous manifold: A comprehensive study of the tracking dynamics of continuous attractor neural networks," *Neural Comput.*, vol. 22, no. 3, 2010.
- [27] D. Griffiths, *Introduction to Quantum Mechanics*. Prentice Hall, 2004.
- [28] C. C. A. Fung, K. Y. M. Wong, and S. Wu, "Dynamics of neural networks with continuous attractors," *Europhys. Lett.*, vol. 84, p. 18002, 2008.
- [29] C. Darken and J. Moody, "Towards faster stochastic gradient search," *Advances in Neural Information Processing Systems*, vol. 4, 1991.
- [30] H. Markram, Y. Wang, and M. Tsodyks, "Differential signaling via the same axon from neocortical layer 5 pyramidal neurons," *Proc. Natl. Acad. Sci.*, vol. 95, pp. 5323–5328, 1997.
- [31] R. S. Zucker and W. G. Regehr, "Short-term synaptic plasticity," *Annual Review of Physiology*, vol. 64, pp. 355–405, 2002.
- [32] L. C. York and M. C. W. van Rossum, "Recurrent networks with short term synaptic depression," *J. Comput. Neurosci.*, vol. 27, pp. 607–620, 2009.
- [33] B. S. Gutkin, C. R. Laing, C. L. Colby, C. C. Chow, and B. Ermentrout, "Turning on and off with excitation: the role of spike-timing asynchrony and synchrony in sustained neural activity," *J. Computational Neuroscience*, vol. 11, pp. 121–134, 2001.
- [34] J. Wu, X. Huang, and C. Zhang, "Propagating waves of activity in the neocortex: What they are, what they do," *J. Comput. Neurosci.*, vol. 14, pp. 487–502, 2008.
- [35] L. F. Abbott, J. A. Varela, K. Sen, and S. B. Nelson, "Synaptic depression and cortical gain control," *Science*, vol. 275, pp. 220–224, 1997.
- [36] V. Matveev and X. J. Wang, "Implications of all-or-none synaptic transmission and short-term depression beyond vesicle depletion: A computational study," *Journal of Neuroscience*, vol. 20, pp. 1575–1588, 2000.
- [37] J. Tabak, W. Senn, M. J. O'Donovan, and J. Rinzel, "Modeling of spontaneous activity in developing spinal cord using activity-dependent depression in an excitatory network," *Journal of Neuroscience*, vol. 20, pp. 3041–3056, 2000.
- [38] I. S. Gradshteyn and I. M. Ryzhik, *Table of Integrals, Series, and Products*. Academic Press, 5 ed., 1994.